DTNSRDC-SME-CR-18-83

Contract No. N00024-80-C-5337

Acoustic Emission Determination of Deformation Mechanisms Leading to Failure of Naval Alloys

J. T. Glass, S. Majerowicz, R. E. Green, Jr.
Materials Science and Engineering Department
The Johns Hopkins University
Baltimore, MD 21218

May 1983

FINAL REPORT
(VOLUME I)

Prepared for:

David Taylor Naval Ship R&D Center (Code 2820)
and
Naval Sea Systems Command (SEA 05R25)

Approved for public release; distribution unlimited

UNCLASSIFIED

SECURITY CLASSIFICATION OF THIS PAGE (When Data Entered)

REPORT DOCUMENTATION PAGE		READ INSTRUCTIONS BEFORE COMPLETING FORM
1. REPORT NUMBER DTNSRDC SME-CR-18-83	2. GOVT ACCESSION NO. A135387	3. RECIPIENT'S CATALOG NUMBER
4. TITLE (and Subtitle) Acoustic Emission Determination of Deformation Mechanisms Leading to Failure of Naval Alloys (Volume I)		5. TYPE OF REPORT & PERIOD COVERED Final 12/27/79 - 12/27/82 6. PERFORMING ORG. REPORT NUMBER
7. AUTHOR(s) J. T. Glass S. Majerowicz R. E. Green, Jr.		8. CONTRACT OR GRANT NUMBER(s) N00024-80-C-5337
9. PERFORMING ORGANIZATION NAME AND ADDRESS The Johns Hopkins University Materials Science and Engineering Dept. Baltimore, MD 21218		10. PROGRAM ELEMENT, PROJECT, TASK AREA & WORK UNIT NUMBERS
11. CONTROLLING OFFICE NAME AND ADDRESS Naval Sea Systems Command Washington, D.C. 20362 SEA05R25, Dr. H. H. J. Vanderveldt		12. REPORT DATE May 1983 13. NUMBER OF PAGES 155
14. MONITORING AGENCY NAME & ADDRESS(if different from Controlling Office) David Taylor Naval Ship R&D Center Ship Materials Engineering Department Annapolis, MD 21402 Code 2820, Mr. Charles A. Zanis		15. SECURITY CLASS. (of this report) Unclassified 15a. DECLASSIFICATION/DOWNGRADING SCHEDULE

16. DISTRIBUTION STATEMENT (of this Report)

Approved for public release, distribution unlimited.

17. DISTRIBUTION STATEMENT (of the abstract entered in Block 20, if different from Report)

18. SUPPLEMENTARY NOTES

19. KEY WORDS (Continue on reverse side if necessary and identify by block number)

Acoustic Emission
Laser Beam Interferometer
HY80, 100, 130 Steels
Mechanical Deformation
Nondestructive Evaluation

20. ABSTRACT (Continue on reverse side if necessary and identify by block number)

In this investigation the acoustic emission behavior of three Naval alloy steels (HY 80, HY 100 and HY 130) was characterized during tensile elongation and bend type loading. The detection of emissions was accomplished using a very new, state of the art interferometer supplied by the Johns Hopkins Applied Physics Laboratory as well as with a unique piezoelectric transducer developed at the National Bureau of Standards. The deformation and fracture of these HY steels was documented via optical and

DD FORM 1 JAN 73 1473 EDITION OF 1 NOV 65 IS OBSOLETE
S/N 0102-014-6601

UNCLASSIFIED
SECURITY CLASSIFICATION OF THIS PAGE (When Data Entered)

20. (Continued)

scanning electron microscopy and was correlated with observed emissions in order to determine the generating mechanisms.

All three steels investigated were found to exhibit very similar deformation and fracture modes despite a slight difference in microstructures. They also exhibited identical acoustic emission behavior within statistical variances. Their fracture consisted of a very ductile mode involving void coalescence and growth with final failure occurring by knife edge rupture of numerous microligaments between voids. Two major types of acoustic emission were detected. The first occurred prior to yielding and was attributed to dislocation glide over distances above some critical minimum detectable mean free path. The second type was generated by the multiple rupture of many microaligaments immediately prior to failure. All three steels exhibited an appreciable Kaiser Effect on reloading. These results indicate that these steels are not well suited for nondestructive evaluation via acoustic emission unless the microligament rupture causing failure is known to be detectable yet propagate stably for a given loading situation, allowing for its detection prior to catastrophic failure - a fairly questionable condition.

EXECUTIVE SUMMARY

This is the final technical report (two volumes) summarizing research activities performed for the David Taylor Naval Ship Research and Development Center (Code 2820) and the Naval Sea Systems Command (SEA 05R15). The authors wish to thank Mr. Charles A. Zanis (DTNSRDC) and Dr. H. H. J. Vanderveldt (NAVSEA) for their continued encouragement and support during the course of this research. The purpose of this research was to use innovative optical techniques and superior signal capture and processing systems to determine the waveforms, frequency spectra, and propagational behavior of the acoustic emission signals generated by the various mechanical deformation mechanisms leading to failure of metal alloys of prime importance to naval structures. Experiments were performed using a laser interferometer detector and a new piezoelectric transducer, both of which permitted recording of the first arriving acoustic emission signal unmodified by transducer construction artifacts as experienced with conventional commercially available piezoelectric acoustic emission transducers.

Acoustic emission events were either generated by pulling microtensile specimens in an extremely quiet microtensile machine (Volume I) or by the brittle, step unloading fracture of glass capillary tubes on the surface of test specimens possessing different geometries (Volume II). All acoustic emission event waveforms were recorded by a high speed transient

recorder and stored on magnetic mini-diskettes for analysis on a high speed digital omputer and for future propagational behavior and waveform analysis. Specimens which were pulled in the microtensile machine were examined using optical and scanning electron microscopes to determine correlation between acoustic emission events and microstructural changes.

ABSTRACT

In this investigation the acoustic emission behavior of three Naval alloy steels (HY 80, HY 100 and HY 130) was characterized during tensile elongation and bend type loading. The detection of emissions was accomplished using a very new, state of the art interferometer supplied by The Johns Hopkins Applied Physics Laboratory as well as with a unique piezo-electric transducer developed at The National Bureau of Standards. The deformation and fracture of these HY steels was documented via optical and scanning electron microscopy and was correlated with observed emissions in order to determine the generating mechanisms.

All three steels investigated were found to exhibit very similar deformation and fracture modes despite a slight difference in microstructures. They also exhibited identical acoustic emission behavior within statistical variances. Their fracture consisted of a very ductile mode involving void coalescence and growth with final failure occurring by knife edge rupture of numerous microligaments between voids. Two major types of acoustic emission were detected. The first occurred prior to yielding and was attributed to dislocation glide over distances above some critical minimum detectable mean free path. The second type was

generated by the multiple rupture of many microligaments immediately prior to failure. All three steels exhibited an appreciable Kaiser Effect on reloading. These results indicate that these steels are not well-suited for non-destructive evaluation via acoustic emission unless the microligament rupture causing failure is known to be detectable yet propagate stably for a given loading situation, allowing for its detection prior to catastrophic failure - a fairly questionable condition.

1. INTRODUCTION

1.1 Background

When certain materials undergo deformation, a phenomenon known as acoustic emission occurs. Acoustic emission refers to an elastic wave generated from an area of rapid strain relaxation in a material. When this wave reaches the surface of the body in which it occurs, it can cause a detectable displacement containing information about its source.* The amount of distortion this wave undergoes while propagating through the material, and the ability of the detection system to deliver a true representation of the surface displacement, help determine the usefulness of acoustic emission.

The term acoustic emission (AE) may be applied to a wide range of wave phenomena, from siesmic activity in the earth's crust, to the elastic waves generated by the crazing of polymers. Audible AE has no doubt been observed since the beginning of time (i.e. the "crackling" of falling trees or breaking ice) and used, instinctively, to tell the observer something about the material emitting the sounds. Modern quantitative use of AE (both audible and subaudible), however, was

---

*(in optically transparent media this wave may be detected before reaching the surface)

not recorded until this century in the field of seismology. Early investigators were interested in predicting rockbursts and earthquakes by detecting subaudible "microseisms" [1-8]. The transducer, called a geophone, used to detect the seismic disturbances was a bimorphic piezoelectric crystal designed to fit into the same drill holes as sticks of blasting powder. After passing through an impedance matching transformer the signal travelled as much as 1,000 feet, for safety reasons, before being amplified, filtered and recorded by a stylus that was mounted in the field of a permanent magnet. Even with this relatively crude detection system it was found that the high frequency components of a microseism were attenuated more rapidly than the low frequency components and the listener could crudely estimate the distance a rockburst had travelled by determining its frequency content. More commonly, this system was used to predict rockbursts via microseism count, much in the same way AE from structural materials was later used to predict their failure. In fact, early work in seismology contained most of the precursors of future AE investigations - transducers, amplifiers, filters, attempts at triangulation and source identification [9].

The first comprehensive, well-documented study of acoustic emission directly pertinent to the investigation presented here was performed by Kaiser [10]. He

conducted studies on polycrystalline zinc, steel, aluminum, copper and lead, finding that all these materials emitted elastic stress waves during deformation. Kaiser was the first to clearly demonstrate the link between acoustic emission and deformation. He also noted that many materials which emitted during initial loading did not emit when unloaded and reloaded until the maximum stress used in the first loading was exceeded. This has since been labelled the Kaiser Effect. Schofield [11] and Tatro [12] expanded on Kaiser's work with broadened studies of this relationship, including experiments with single crystals. Schofield demonstrated that twin production and slip band formation, along with Kaiser's previously deduced grain boundary reorientation, were all sources of acoustic emission. He was also the first to distinguish between burst emission, a short higher amplitude transient wave and continuous emission, which appears as a low amplitude rise in the noise level [13,14]. With the encouragement of Schofield and Tatro, work in AE has increased dramatically since that time. Many excellent review articles have been published describing the various investigations conducted thus far [15-21].

The ultimate goal of the majority of work in AE, as with most non-destructive evaluation research,

is to be able to verify the integrity and predict the failure of engineering structures. AE was utilized for this purpose as early as 1964 at Aerojet General [22]. While monitoring rocket motor cases during hydrostatic proof testing, investigators were able to observe crack initiation and growth prior to failure and, employing triangulation techniques, locate the origin of failure within 12 inches. Since this time AE has been used in various other applications, from studying weld phenomena [23-26] and phase transformations [27-29] to monitoring pressure vessels [30-32] and airplane components [33,40].

A major drawback in the utilization of AE, however, has been a lack of knowledge of the underlying mechanisms generating the AE in a given material. Much attention has been given to this problem in the past. As previously mentioned, early work by Kaiser [10], Schofield [11] and Tatro [12] demonstrated that twin production, slip band formation and grain boundary reorientation were all sources of AE. By the late 1960's dislocation unpinning and mobile dislocation motion were both found to generate AE as well [34-36]. Phase transformations have also been known to cause AE for some time [29]. Fatigue crack growth, stress corrosion cracking and brittle crack propagation are also all sources of AE for certain materials and loading

conditions [33,37-44]. Intermetallic particle and inclusion fracture have been added to the list of AE generation mechanisms recently [45-46]. Excellent studies in this area have been conducted at Harwell, England by Wadley, Scruby et al. [47-50]. Investigators have employed a novel acquisition system and specimen geometry to bridge the gap between theory and experiment, while utilizing optical and electron microscopy to determine AE sources for various alloys. For a complete bibliography of AE work, with abstracts, including further studies on source identification, one should consult Ref. 51.

1.2 Theory

A number of review articles, as well as current studies, have been published recently involving AE theory [50,52-58]. The goal of most theoretical work is to be able to analyze a voltage-time record obtained from the surface displacement of a body caused by an AE event within and thereby unambiguously determine the force-time function at the source. The successful implementation of this would lend a great deal of insight into the generating mechanism.

The occurrence of a detectable AE can be described as a series of linked events as Hsu has done [52] (Fig. 1). An AE source is activated within the

specimen, causing a dynamic force or stress field change at a particular location (Link I). This force field change is propagated as a mechanical disturbance (i.e. an elastic wave - Link II). The sensor detects this disturbance when it reaches a free surface and outputs a voltage proportional to some property of the disturbance (i.e. particle velocity, vertical displacement, etc.) depending on the detector type (Link III). Some type of signal processing or display is then used to extract more information from the signal (Link IV). Finally, this processed signal is used to identify the AE event (Link V), or at least the force-time function generated from this event. In essence, the goal of AE theory is to obtain links IV and V in order to learn more about the deformation mechanism causing the event.

Although there are a number of approaches to the problem stated above, the basic theory is the same. Assuming the process to be linear, one can write the "links" mathematically as:

$$V(t) = A(t) * B(t) * C(t)$$

where $V(t)$ = voltage output

$A(t)$ = source function

$B(t)$ = structure function (dynamic Green's function)

C(t) = acquisition system function

"*" denotes convolution

The final output is seen to contain information about: (i) the AE source, (ii) the structure through which the wave has propagated, and (iii) the acquisition system (transducer, coupling, electronics, etc.). V(t) is a measured output, therefore, when any two of the other functions are known in this equation, the third may be determined by deconvolution.

Utilizing the concept of a reference impulse and the impulse responses of the various parts of a system [53] the equation of convolution may be found for a source signal, $i_i(t)$, to be:

$$v_i(t) = i(t) * e_i(t) * h(t) \qquad (1)$$

where $e_i(t)$ = impulse response of that portion of the specimen traversed by i(t)

$h(t)$ = impulse response of the acquisition system

$v_i(t)$ = measured output

The Fourier transform of (1) is then:

$$V_i(\nu) = I(\nu) \cdot E_i(\nu) \cdot H(\nu) \qquad (2)$$

(convolution in time domain becomes simple multiplication in the frequency domain).

One can also write the convolution equation for a reference signal r(t), which is generated artificially at a free surface, propagates through the specimen, and is detected at another free surface:

$$v_r(t) = r(t) * e_r(t) * c(t) * h(t) \qquad (3)$$

where $e_r(t)$ = impulse response of that portion of the specimen traversed by r(t)

$c(t)$ = impulse response of the transducer emitting r(t)

$v_r(t)$ = measured output

$h(t)$ = same as in (1)

whose Fourier transform is:

$$V_r(\nu) = R(\nu) \cdot C(\nu) \cdot E(\nu) \cdot H(\nu) \qquad (4)$$

If the transducer emitting r(t) has a flat spectrum in the band of frequencies studied (i.e. we are generating a sufficient impulse or spike in the time domain) then we know:

$$R(\nu) \cdot C(\nu) = K \qquad (5)$$

which simply states that the Fourier transform of an impulse is a constant. (4) then becomes:

$$V_r(\nu) = K \cdot E_r(\nu) \cdot H(\nu) \qquad (6)$$

Combining equations (2) and (6):

$$V_i(\nu) = \frac{1}{K} \cdot \frac{E_i(\nu)}{E_r(\nu)} I(\nu) \cdot V_r(\nu) \qquad (7)$$

or

$$I(\nu) = K \frac{E_r(\nu)}{E_i(\nu)} \cdot \frac{V_i(\nu)}{V_r(\nu)} \qquad (8)$$

where $I(\nu)$ is the Fourier transform of the signal in which we are interested; the source function (i.e. the emitted AE signal function). We can measure K, $V_i(\nu)$, and $V_r(\nu)$ directly and for simple geometries (spheres, infinite plates, etc.) one can calculate $E_r(\nu)$ (dynamic Green's function). $E_i(\nu)$, however, remains ambiguous and must be hypothesized in order to deconvolute.

The practical implementation of this theory is therefore hindered in several ways. An AE may originate from various unknown points in a real situation and therefore the transfer function for its passage is unknown. Obtaining a reference signal such that assumption (5) holds can be very difficult when one considers the possible bandwidths of real AE. Microstructural considerations such as grain boundaries (depending on grain size), inhomogeneities and various anisotropies (i.e. rolled materials) also have a

questionable effect on this theory. In fact, even for the simplest situations (simulated, well-characterized sources and ideal geometries), the deconvolution process has met with limited success due to inaccuracies in the transfer function involved. However, excellent results have been obtained by Hsu and co-workers at the National Bureau of Standards [52] which hopefully will pave the way for further theoretical work, applicable to field situations.

1.3 Detectors

There are several possible methods of detecting AE in a material, the most popular to date being the piezoelectric transducer (hereafter referred to simply as transducer). Although considerable progress has been made recently in transducer design by Procter at the National Bureau of Standards [59], allowing a truer reproduction of acoustic signals than previously possible with transducers (see section 2.1.1), they still contain some inherent problems as yet unresolved: (i) Absolute calibration is very difficult, usually requiring that acoustic events be evaluated on a relative scale for each situation, (ii) They have different responses to the various wave types (i.e. longitudinal waves, surface waves, etc.), (iii) Frequency response is often inadequate and marked with

mechanical and electrical resonances, (iv) The sensor loads the surface, causing distortion of an incident wave, (v) The couplant, necessary for wave transmission, adds an unknown impedance to the system, and (vi) The relatively large area of most transducers means that the incident wave is integrated over the entire surface of the active element, causing a complicated stress mode [60]. The result of these inherent problems is that the true waveform reaching the transducer cannot be accurately determined [61-63]. The advantages of transducers, however, especially in an industrial setting, should not be overlooked. They are relatively inexpensive, easy to use and very sensitive.

In recent years, much more attention has been given to the use of two groups of non-contact, broad-band detectors, that are exceptionally useful in laboratory investigations. These are (1) air gap capacitance transducers and (2) optical interferometers. In the past, these detectors, due to their insensitivity, have been used mainly in the detection of high energy events such as simulated AE (glass capillary fracture, lead fracture, electric pulses, etc.) or AE from known, high energy emitters such as tin [61,64-66]. Recent advances in the electronics field, however, have greatly increased their use,

especially optical interferometers, in detecting real AE from a variety of materials [45,61,65-71].

Although air gap capacitance transducers are very useful in that they exhibit a flat frequency response and are non-contact, they can be difficult to work with since they must be located very near the surface of the material being studied. (Capacitance changes due to surface displacements are measured in a DC biased electrostatic element located near the surface.) For this same reason, absolute calibration of these detectors is also a problem. In addition, the probe area is generally rather large, hindering the probing of small specimens or small local areas (i.e. crack tips).

A great deal of work has been done lately to improve interferometric systems and adapt them to the detection of low amplitude AE. As with air gap capacitance probes, no contact with the specimen is necessary and a broadband, flat frequency response is achieved. In addition, optical probes may be utilized a fair distance from the specimen, in hostile environments and over a wide range of temperatures. Transparent media may be probed internally when desired and the small sensitive area (beam diameter) allows probing of local regions of interest, inaccessible by other means.

Finally, the optical detector may be absolutely calibrated with relative ease. These considerations make the optical probe an excellent choice as a detector in an AE investigation.

The work presented here utilized a very novel interferometric system, designed and built by Dr. John Murphy and colleagues at the Johns Hopkins Applied Physics Laboratory (see section 2.1.2) giving the author all of the aforementioned advantages and making possible the detection of true AE waveforms with minimal environmental intrusions (i.e. background noise, mechanical drift, etc.).

1.4 Characterization of Acoustic Emission Signals

Several techniques have been utilized in the past for characterizing AE [72]. Event counting is simply a method by which any event above a preset voltage increments a counter by one and a record is thereby kept of the total number of AE events above a certain amplitude. There are several problems with this technique, the major ones being: (i) The assumption that all counted signals are equally damaging to the material and that all damaging events will be counted, (ii) The fact that some signals are oscillatory in nature and may cause more than one count or, if a delay is built in before reset, events

occurring close together may be missed, and (iii) No information is obtained about the shape of the AE waveform. A closely related method is amplitude sorting in which each emission is characterized by its largest cycle and the amplitudes are then sorted into ranges. This technique was utilized by Nakamura, et al. [73] for crack growth studies in steels. It suffers, however, from many of the same problems as event counting, allowing no way to distinguish between events of similar amplitude but very different time signatures.

Ring down counting, also known as threshold crossing, is a somewhat different technique which catagorizes an AE by the number of times a given signal crosses a preset voltage. It is still difficult, however, to relate this method to a physically meaningful parameter, energy in the AE perhaps being the closest. Unfortunately, the counts are a complicated function of both the detector and the propagating medium, as well as signal coupling efficiency, sensitivity, amplifier gain and the threshold voltage. This not only makes it extremely difficult to make an absolute energy determination but, because some of these parameters many times cannot be held constant during a test, even the relative energies of the AE events are difficult to obtain. Energy would be better

obtained by waveform analysis techniques (i.e. integration of digitized waveforms) in conjunction with the spectral analysis discussed later.

Another method of characterizing AE is by correlating them with better understood, independent material properties such as ultrasonic velocity and attenuation, electrical conductivity, magnetic permeability, etc. To date, relatively little work has been done in this area and that which has been attempted has met with limited success. Imanaka et al. [74] compared ultrasonic attenuation of 27 MHz longitudinal waves with simultaneous AE measurements and found no obvious correlation for copper single crystals and polycrystalline aluminum. Duke [75] monitored the attenuation of 10 MHz longitudinal waves for various aluminum alloys and again no substantial agreement with AE signals was found. Simultaneous internal friction (50 kHz) and AE measurements by Higgens and Carpenter met with somewhat better success [76]. These measurements in 7075 aluminum and pure iron gave insight into the AE mechanisms operating in these materials. As can be seen, in order to fully assess the potential of correlating AE with better known material properties more work is necessary.

A technique receiving a great deal of attention

at present is the spectral analysis of AE. This technique appears to have the greatest potential of being related to a physical event, with the faster mechanisms (i.e. brittle intermetallic particle fracture) causing emissions containing higher frequencies and the slower mechanisms (i.e. mobile dislocation motion) causing AE of lower frequency content. Although this possibility has been realized for some time, (both Kaiser [10] and Schofield [11] made attempts at examining AE frequency behavior) a major drawback in the past has been the lack of available broadband equipment. Recent developments in solid state electronics have increased the feasibility of this technique immensely. Not only are detectors of much higher quality, as previously mentioned, but analog to digital converters with greatly improved resolution and bandwidth are now available. The utilization of the videotape recorder has also increased the potential of obtaining AE characterization by this method. Spectral analysis from the videotape recorder, generally 0-3 MHz, may be obtained via a commercial spectrum analyzer, whereas the digitized information is usually processed by a computer via a fast Fourier Transform algorithm. This is a somewhat more expensive but much more versatile method, allowing for various signal processing techni-

ques (i.e. integration to obtain energy, various correlation techniques, signal averaging, etc.) perhaps giving an investigator even more insight into the AE characterization. Some investigations utilizing the concept of frequency analysis have shown that different sources do emit AE of different frequencies in certain materials [45,77-80]. Other studies have concluded there was no frequency dependence of the AE in the material under consideration [81] or that a frequency dependence was due to specimen geometry and the acquisition system utilized in the tests [82]. From this discussion, it is apparent that no general conclusions can be drawn at this time except that the success of the spectral analysis characterization is dependent not only on the material under investigation and the loading conditions, but also on the specimen geometry and acquisition system employed. If these parameters are well documented and controlled, however, spectral analysis seems to hold great promise, especially in the laboratory environment.

It should be noted that the major drawbacks of the characterization techniques most popular in the past (event counting, amplitude sorting and ring down counting) may not be terribly restricting for non-destructive testing purposes once the AE behavior of

a material is well-documented. For laboratory purposes, however, they yield very little information about the AE generating processes. As Kline states [67], it is not possible to quantify the complete time evolution of an AE by a single number (i.e. count rate, etc.). When attempting a correlation between deformation mechanisms and AE one would like a characterization parameter which groups AE from like sources together. The complexity of the signal processing necessary to accomplish this is a function of the complexity of the situation (i.e. how many sources are operating throughout a test) and the "trueness" of the acquisition system (i.e. is it a broadband, non-intrusive system). In an ideal situation, one should be able to distinguish AE events in their time domains (i.e. rise times, etc.) if they are, in fact, distinguishable at all since the frequency is simply a representation of the time function. Bruchey [45] found that he could separate signals from two different sources by examining either time records or their transforms. The best situation for studying sources would seem to be utilization of a true enough acquisition system and a proper specimen geometry, along with as simple a deformation condition as possible, in order to maximize the probability that signals will be distinguishable in their

time domains. Although these requirements may seem trivial when seen in writing, they are in reality quite stringent and difficult to obtain.

Once the generating mechanisms for and properties of AE are known for a given material, the next step is to design a field system where none of the aforementioned simplifications are possible, which exploits these findings. For instance, when the most "damaging" sources are found to contain most of their energy in a particular frequency band, and the potentially dangerous AE density per unit volume for these particular AE events is established, a practical transducer based acquisition system could be designed, perhaps utilizing an event counting technique which employs filters to only look at these particular emissions.

In the spirit of "first things first," this investigation deals with the employment of a new, state of the art, interferometer, a unique piezoelectric transducer design as well as several other novel ideas (i.e. specimen geometry, loading apparatus, etc.) in order to characterize AE behavior during the deformation and fracture of a series of rather microstructurally complex Naval alloy steels.

2. EXPERIMENTAL PROCEDURE

Three different types of tests were conducted on the material under investigation: (i) micro-tensile tests (ii) bend tests (iii) macro-tensile tests. In this way, the AE behavior of the material was more completely characterized than would be possible with any single test type. AE was detected in the micro-tensile and bend tests utilizing an optical interferometer whereas a piezoelectric transducer was employed during the macro-tensile tests. Complete descriptions of these detection and loading systems as well as the differences between the various testing configurations are given in the following sections.

2.1 Micro-tensile Tests

Initial experiments were conducted on micro-tensile specimens for several reasons. First, it is desirable to probe very close to the AE sources and be able to quantitatively assess microstructural alterations that occur as a result of deformation, both of which are feasible only in very small gauge sections. Additionally, if the material is a copious emitter, the micro-tensile specimens avoid signal overlap, allowing true waveforms to be detected.

2.1.1 Specimen Considerations

Material

The materials investigated in this study were all High Yield (HY) Naval alloy steels supplied by Mr. Charles Zanis of the David Taylor Naval Ship Research and Development Center (DTNSRDC). Three steels, designated HY 80, HY 100, and HY 130, (where the numbers following the HY represent the approximate yield strength of the materials), were studied in order to determine the mechanisms operating during their deformation and fracture and the related emission characteristics. These steels were chosen for study due to their widespread application in Naval structures and the subsequent desire to non-destructively evaluate their integrity. The work presented here has determined the feasibility of AE as a tool for the non-destructive evaluation of these materials by determining when AE occurs in this material and what are its causes.

Average compositions and mechanical properties of samples from the same lot as those used in this investigation are given in Table I for each type of steel. They were all hot rolled and then water quenched from 1650°F ($\pm$ 25°). HY 80 was then tempered at 1100°F and HY 100 at 1050°F. HY 130 was reheated to 1550°F ($\pm$ 25°) and water quenched again prior to a tempering at 1160°F. After tempering, all were water

quenched. The manufacturer was Lukens Steel Company and the mill order numbers for the HY 80, HY 100 and HY 130 specimens were 72661-1, 12286-1 and 88433-1, respectively, while DTNSRDC tag numbers were 292, 299 and 250, respectively. Data reported for this investigation was obtained from specimens cut in the transverse direction from rolled plates (i.e. the longitudinal axis of the specimen lay in the rolling plane, perpendicular to the rolling direction). It should be realized that military specifications on engineering materials are generally more concerned with properties than chemical composition or heat treatment and therefore these latter two conditions may vary for supposedly equivalent materials if obtained from different manufacturers as well as between various lots and time periods for the same manufacturer.

The microstructure as well as the precise deformation and fracture mechanisms for these steels will be treated in later sections. It is sufficient to say at this point that, as indicated by their mechanical properties these metals are relatively ductile during room temperature deformation.

Geometry

In order to properly characterize the acoustic behavior of a material, one would ideally like a

recorded waveform which is an exact representation of the waveform emitted from the AE source. In this way, the most information can be obtained from the wave about the deformation mechanism causing the emission and therefore the integrity of the material. As discussed in section 1.2, however, this is not generally possible, as the wave is modified by various parts of the system through which it passes. On the other hand, some portions of the system, for example the specimen geometry, can be designed to minimize the modification they impart to the wave.

Micro-tensile geometries utilized by previous investigators have influenced the AE signals recorded to varying extents. Many times bandwidth limitations in other parts of the system, were such that true waveform representations were not expected and the geometry effect was therefore of no real concern. In the current investigation, however, bandwidth of the detection system (see section 2.2) is such that the specimen geometry may well be the limiting link. In order to develop a geometry which would have a minimal effect on AE waves, a known waveform (surface step unloading at a point caused by glass capillary fracture [65,83]), was propagated through several micro-specimens of steel possessing various cross-sections. All of these waveforms were recorded using a new piezoelectric

acoustic emission transducer developed by Tom Proctor at the National Bureau of Standards [59]. The design and detection characteristics of this transducer are discussed in section 2.3. It should be noted here that this transducer did faithfully detect the first arriving waveform characteristic of glass capillary fracture (Fig. 2) without modification of the signal as caused by conventional commercial piezoelectric AE transducers (Fig. 3). It agreed, within experimental error, with the theoretical waveform shown in Fig. 4 [84,85]. The arrival of longitudinal, shear and Rayleigh waves emanating from a point source on the same surface can be seen in both waveforms. Portions of the waveform following the Rayleigh spike, in the experimental case, are due to resonance in the transducer, as well as reflections from free surfaces since no specimen is truly an infinite half-space as in the theoretical case. These regions may be disregarded during this specimen geometry work and only the distortion the specimens impart to the wave up to the first arriving Rayleigh spike need be examined. Although the glass capillary fracture is not of infinite bandwidth as in the theoretical case or as large a bandwidth as some AE [87], it is a close enough approximation to be an invaluable aid for various investigations including the specimen design work presented here and allows for

a much better micro-tensile geometry than previously utilized.

A schematic of the arrangement utilized in this specimen geometry determination is shown in Fig. 5. The fracture of a capillary tube causes a step unloading which propagates an elastic wave through a micro-specimen of a certain cross-section onto the surface of a large aluminum test block via a coupling fluid and then propagates across this surface until it reaches the point of detection. Figure 6 is the waveform used as a standard for the tests and was obtained by breaking a glass capillary directly on the large aluminum test block rather than through one of the micro-specimens. It therefore is distorted less than those waves propagated through the micro-specimens. An acceptable micro-specimen cross-section must yield a waveform very close to this shape shown in Fig. 6. As previously stated, the waveforms are only compared up to the Rayleigh spike since the characteristics of the wave after this point are greatly dependent on transducer resonances and the large aluminum test block rather than the micro-specimens. Also, the first arriving wave is generally all that is important in broadband AE work since at later times, no matter how well the specimen is designed, the free surfaces effect the wave. Determining what portion of the total wave-

form is the "first arriving wave" can be difficult and at times arbitrary if a theoretical waveform for the given source is not known as is the case in most AE work. In the glass capillary fracture, however, the theoretical waveform is known and the first arriving wave is seen to end at the Rayleigh spike.

Figure 7 shows the signal detected on the surface of the aluminum test block caused by breaking a glass capillary on a square cross-section (0.075 in x 0.075 in) micro-specimen. The signal modification (compare to Fig. 6) of the first arriving waves of all three types (longitudinal, shear and Rayleigh) is minimal whereas square cross-sections both larger (0.123 in x 0.123 in) and smaller (0.060 in x 0.060 in) cause considerable distortion to the waveform as shown in Figs. 8 and 9, respectively. It was also found that if the width (0.025 in) of the micro-specimen through which the wave is propagated is less than the thickness (0.075 in), the waveform is distorted (Fig. 10). If, on the other hand, the width (0.075 in) is greater than the thickness (0.03 in), there is very little distortion as shown in Fig. 11.

In general, if the thickness is equal to or less than the width of the specimen and is approximately 0.075 inches or less, distortion is minimal. An upper bound has therefore been set on specimen dimensions.

The results are in agreement with the intuitive idea that the thinner the specimen the better, for wave propagation through its thickness. This has been given quantitative meaning and a set of constraints has been added to the width (width $\geq$ ~0.075 $\geq$ thickness). A more complete catalogue of waveforms obtained during these tests is presented in Appendix A.

After determining specimen cross-section requirements, the geometry shown in Fig. 12 was designed. Not only did this specimen incorporate the gauge dimensions for minimal distortion, as determined by the above experiments, but it also utilized a gauge curvature designed to guide unwanted reflections away from the point of detection (see Fig. 12). Since the angle of incidence equals the angle of reflection and since the sides of the gauge section were concave, waves incident on these sides were, in general, reflected such that they diverged away from the longitudinal symmetry plane perpendicular to the detection surface and therefore away from the detector. This same idea has been used in fracture mechanics studies to avoid stress wave intensification from reflected waves at the tip of a crack [86].

Surface Preparation

In order to obtain maximum sensitivity from the

interferometer (see section 2.1.2) in detecting AE signals and to make proper optical and scanning electron microscope observations of microstructural changes caused by deformation, the specimens surface was polished to a mirror finish. Previous specimens of 304L stainless steel and 2024 aluminum were prepared by mounting them in an acrylic quickmount, metallographically polishing the surface to be probed and examined, and then chemically dissolving the quickmount prior to testing. When this was attempted with the current Naval steel specimens, a deposit, which appeared to be a corrosion product, formed on the surface decreasing the reflectivity to such an extent that interferometric measurements were impossible. In order to solve this problem, specimens were attached to a mounting fixture (Fig. 13) either by using a "super glue" type cement, which could be dissolved in acetone without damage to the specimens, or magnetically, making the preparation of ferromagnetic materials exceptionally easy.

2.1.2 System Description

A block diagram and photograph of the experimental set-up are shown in Fig. 14. The specimen was deformed in a tensile machine while its polished surface was monitored by a laser interferometer. An AE

reaching this surface caused a displacement giving rise to a voltage output from the photodetectors in the interferometer. Room noise below a set cutoff frequency and specimen "drift" due to a Poissons ratio effect was eliminated by the path stabilization loop incorporated in the interferometric system (to be discussed later in this section), thereby avoiding saturation of the detectors. The output proportional to the higher frequency surface displacements was fed into a transient recorder where the voltage-time profiles were digitized and automatically stored on magnetic disks.

Loading Machines

A loading machine utilized in these tests must meet two major conditions with respect to its noise characteristics. The noise must be below the stabilized frequency of the interferometer and must also be of low enough amplitude so that it does not disable the stabilization system. Most conventional tensile machines do not meet these requirements. The mechanical rubbing of gears or the movement of fluid through valves and orifices generates noise of too great an amplitude. This problem was overcome by two different tensile machines for the tests presented here.

Initial tests were conducted with an Allied

Research Associates pneumatic test machine first utilized by Bruchey [45]. A sketch of the load frame is shown in Fig. 15. Load is applied by the action of pneumatic pressure on a pair of pistons. Figure 16 shows a cross-sectional schematic of the actuator crosshead. Piston-cylinder friction is kept to a minimum by the rolling seal which allows the pistons to be free and self centering in the cylinders. Therefore, there is no metal-metal contact to act as a source of noise. The pistons are pressurized by a 2500 psi tank of Argon gas regulated to yield a 50 psi maximum pressure up to approximately 200 lbs, which is adequate to fracture the micro-tensile specimens.

Operation of this pneumatic system is analogous to the dead weight loading of a specimen. Although loading can be controlled accurately and with relative ease by the use of two opposing pressure valves, there is a drawback to this and any other dead weight loading system for AE work. In any ductile material, the moment an instability occurs during its loading, uniform deformation ceases and localized strain begins. This is commonly referred to as necking and occurs at a stress concentration in the material (i.e. a scratch on the specimen, a large inclusion or other defect in the specimen, etc.). This phenomena occurs in almost all engineering materials during tensile loading and

manifests itself as a load drop on a conventional, constant elongation rate tensile machine. Deformation then continues until some critical diameter is reached whereupon the specimen fractures. In a constant load rate machine there is no way for this load drop to occur and as soon as the cross section of the specimen starts to decrease (i.e. necking begins) there is more than enough load to complete the fracture process.

Therefore, there is very little time between the onset of necking and the attainment of the critical diameter for fracture due to the fact that load does not drop and therefore stress increases unstably as soon as the neck begins to form. This prevents the monitoring of AE during the severe plastic flow occurring in the necked region, completely excluding certain mechanisms occurring only in this region as AE sources.

To overcome this problem a tensile machine as quiet as the pneumatic tensile machine but giving constant displacement was necessary. This was accomplished by designing a "thermal" tensile machine. This machine, a schematic of which is shown in Fig. 17, utilized the same frame as the pneumatic machine but replaced the actuator crosshead with a single bar of 6061 aluminum surrounded by a small furnace. One of the grips was attached to this bar and the other to a

fixed cross piece. The bar was heated prior to the test to a temperature sufficient to give, upon cooling, enough thermal contraction to fracture the specimens. After the bar was heated, the specimens were placed firmly in the grips and the bar was allowed to cool, fracturing the specimens as a constant displacement machine. The specimens were thermally insulated from the grips so that deformation was occurring at approximately room temperature. Although this was a very quiet tensile machine, a drawback was the lack of control of the displacement (i.e. strain rate, stopping a test at some point before completion, etc.). With some refinements to the furnace it is felt this drawback could be easily overcome. In the present work, specimens of each material were tested in both the pneumatic machine, in order to easily and controllably characterize the material prior to necking, and the thermal machine, so that postnecking acoustic activity could be determined. Universal joints were utilized in both types of machines to ensure that the plane of the specimen did not change during a test and the optical interferometer stayed aligned.

The load was monitored by placing a Schaevitz, model FTD-24 load cell in series with the specimen and the load frame. It was calibrated using 5 kg Instron weights and was recorded on either a strip

chart recorder or an X-Y plotter. Displacement was measured for select specimens utilizing a Schaevitz, model CAS-025, linear variable differential transformer (LVDT). The LVDT was calibrated with a micrometer and then the ferromagnetic core was mounted to one grip with the solenoid coil on the other (Fig. 18). The specimens were too small to have the LVDT mounted directly on them so displacement measurements included the elastic deformation of the grips. When the LVDT was used, its output drove the X-axis of an X-Y plotter while the load cell output drove the Y-axis.

Interferometer

Although the micro-tensile machines discussed above were an integral part of the overall AE detection system and believed to be types not previously used in this manner, the heart of this project as far as equipment is concerned, was the interferometer. This interferometer combined an innovative optical arrangement and path stabilization system to make it an excellent AE detector. One goal of this work was to test, modify and verify the performance of this new interferometric system as well as determine design and performance changes necessary for future generations of the same system.

As a cooperative effort with the present research

project the new laser interferometer was designed and constructed by Dr. John Murphy and his colleagues at the Johns Hopkins University Applied Physics Laboratory. The design goals of providing an improved interferometric detector possessing a greater high frequency response (maximum operating frequency greater than 40 MHz), low minimum detectable displacement (less than or equal to 0.1 nm), and convenient, portable operation in a laboratory environment adaptable to samples of different shapes and orientations have been realized.

Figure 19 is a block diagram of the optics in the APL laser interferometer. This device is a polarized Michelson interferometer modified to include active stabilization of the relative optical path lengths of the signal and reference arms of the interferometer. The first polarized beam splitter (BS1) codes the reference beam path through the lens assembly, the lead zirconium titanate (PZT) piezoelectric mirror mount, and return path to the optical detectors with one optical polarization component. The signal beam path is coded with the orthogonal optical polarization by the first polarized beam splitter (BS1). This beam is steered by the beam position mirror and gimbal mirror to the specimen surface and then returned to the optical detectors. The second polarized beam splitter

(BS2) and pair of optical detectors allows the light beam interference signal $S = A_S A_R \cos \Omega$ to be detected without the background of the signal and reference beam intensities themselves. A_S and A_R are the light wave amplitudes of the signal and reference beams, respectively, and $\Omega = \frac{4\pi}{\lambda} (L_S - L_R)$ is the difference of signal and reference path lengths in units of the light wavelength λ.

Two active stabilization loops control Ω in order to minimize environmentally caused changes. The first loop operates the PZT piezoelectrically driven reference mirror as a first order control loop. This loop is limited to low frequency (less than 6 kHz) operation because of the response characteristics of the PZT element. It allows, however, for easy absolute internal calibration simply by driving the reference mirror with a known voltage signal corresponding to an exact displacement prior to a test. This can be recorded via the high frequency output and thereby utilized to obtain the Angstroms surface displacement per volt output. This "calibration waveform" as recorded by the transient recorder is shown in Fig. 20. The second loop uses the electro-optic (EO) modulator as a fast (frequencies from 0 to slightly greater than 100 kHz) zero order loop controller. Working together, locking in on and tracking

a set of fringes for frequencies below ~100 kHz, these two loops stabilize the interferometer against environmental noise as well as thermal and mechanical drift.

The frequency response of the interferometer was improved in the high frequency region since it is essential that a surface displacement measurement probe have a response faster than the signals produced by the acoustic emission source. The amplitude versus frequency plot of its response to a test signal generated by a fast light-emitting diode showed that the detection bandwidth (3 dB point) and the maximum detectable response frequency are higher than prior designs. The new interferometer possesses a flat frequency response *from* DC to 60 MHz and drops off to the 3 dB point at 160 MHz. Since the detection signal-to-noise ratio is inversely proportional to the square root of the detection bandwidth, increasing bandwidth can degrade detection of small amplitude signals. The use of balanced photodiodes as optical detectors and an improved laser power supply has permitted detection of signals with amplitudes as small as 0.1 nm (1 Å) while retaining increased detection bandwidth. The use of the beam steering mirrors along with a telescoping lens assembly to focus the signal component of the laser beam on the specimen surface makes adjustment of this interferometer more convenient

than prior designs. It can accommodate a wide range of orientations of the specimen surface without major readjustment.

A basic schematic of the support circuitry for the optical arrangement just described is shown in Fig. 21. Each of the two detectors has two outputs - a low frequency output, approximately 0 to 100 kHz, which drives the path stabilization system and a high frequency output, greater than 60 MHz. The high frequency outputs are differentially amplified to one output, directly proportional to high frequency surface displacements (i.e. AE), which is then filtered and fed into the transient recorder. It is this recorder which is the limiting link in the bandwidth of the system (discussed later in this section). The low frequency outputs are used, via the path stabilization circuitry, to drive the PZT pusher on which the reference mirror is attached and the modulator, both discussed earlier. After being amplified separately, the outputs are fed into a differential amplifier whose output drives both the high frequency EO modulator and the integrator which ultimately drives the PZT pusher. The integrator outputs a signal proportional to thermal or mechanical DC drift as well as superimposed environmental noise below 6 kHz. This output drives the PZT via a high voltage amplifier,

thereby allowing the reference mirror to "track" a given set of fringes. When the drift voltage reaches a critical value (either plus or minus, depending on the direction of the drift in the specimen) which is set according to the power and travel capabilities of the PZT pusher, the drivers fire the relay which resets the integrator to zero, thereby resetting the PZT pusher back to its initial, equilibrium position where it begins tracking a new set of fringes. As previously stated, this complex stabilization loop acts as a filter for noise and drift from zero to approximately 100 kHz while preventing detector saturation due to fringe motion across their active elements. The noise amplitude this system can tolerate is limited by the dynamic ranges of the EO modulator (less than 1.0 μm) and the PZT pusher (approximately 2.1 μm) in their respective frequency ranges.

Transient Recorder

The transient recorder utilized in this study was the limiting factor with respect to frequency bandwidth of the overall system. The recorder, a Nicolet model 204-A, had a sampling frequency of 20 MHz allowing for a maximum detection frequency of 10 MHz. Although this was a great improvement over most systems previously employed to detect AE (whose bandwidth has

been less than 3 MHz and usually in the kHz regime) it was still quite far from the limitations of the interferometer (> 60 MHz). It allowed, however, for the automated capture and storage of AE digitized to 4096 points at 50 nanoseconds per point when utilized at its maximum frequency capabilities.

2.2 Bend Tests

The same materials (HY 80, HY 100 and HY 130) discussed in section 2.1.1 were also deformed in a bending mode. The identical detector system (section 2.1.2), and therefore material preparation techniques, were utilized in these tests as were discussed in conjunction with micro-tensile tests.

2.2.1 Specimen and System Configuration

Deformation was accomplished by the cantilever beam arrangement shown in Fig. 22. The added complexity of compressive and tensile stresses acting simultaneously during the bending more closely approximated an in service situation than the pure tension tests. Specimens were notched in order to concentrate the deformation in a region close to the point of detection. Loading was accomplished by bending one end of the specimen with a screw type indentor while rigidly clamping the other end. Metal-to-metal rubbing was avoided by placing teflon between the indentor and the

specimen. The teflon remained stationary while the indentor turned on it during bending. The excellent attenuation characteristics of the teflon insulated the specimen from any noise generated in the indentor.

2.3 Macro-tensile Tests

2.3.1 Specimens and Tensile Machine

In order to evaluate volume effects on the results from micro-tensile tests, tensile tests on much larger specimens (Fig. 23) were performed with a floor model TT-CM Instron machine with a 5,000 kg maximum capacity. The specimens were machined from the same materials discussed earlier - HY 80, HY 100 and HY 130 (see section 2.1.1). The gauge volumes in these specimens were approximately 1,000 times larger than the micro-tensile gauge volumes.

2.3.2 Detection System

Although attempts were made to acoustically insulate the specimens during testing, the noise levels from the Instron were too great to allow the use of the interferometer as the detection system. Work is currently underway to increase the dynamic ranges of the path stabilization loops in the interferometer in order to make tests on conventional tensile machines, such as this Instron, possible.

For these macro-tensile tests a new transducer, developed by Tom Procter at the National Bureau of Standards (NBS) [59] was used throughout the tests until just after necking. At some point after necking began and before failure, the tests were momentarily stopped while this transducer was replaced with a more durable, commercial, half inch, 1 MHz Panametrics transducer. The NBS transducer was utilized during more than 80% of each test in order to obtain the truest waveform possible. Had it been in place during fracture, however, it would have been damaged. The more durable, although less desirable in its frequency characteristics, commercial transducer was therefore utilized during fracture. As previously discussed, neither of these transducers has the bandwidth of the interferometric system and a true waveform was not expected outside the range of their flat frequency response. They allowed, however, for the filtering of the noise generated by the Instron. Before being recorded, therefore, all frequencies at or below 100 kHz as well as all frequencies above 2 MHz were filtered from the signals.

The range of the NBS transducer is approximately 1.2 MHz and it has been shown to give a true representation of a surface step unloading on an infinite half space, as approximated by glass capillary fracture on

a large aluminum block and demonstrated in section 2.1.1. It accomplishes this by the unique design shown in Fig. 24. A small conical active element of lead zirconium titanate (PZT) is attached to a disk of brass which acts as both an electrical contact and an inertial backing for the transducer. Resonances in the PZT are avoided below 1.2 MHz since waves passing through it are transmitted to the brass disk which is of such dimensions that by the time the wave reflects from its free surfaces and back to the active element the initial electrical signal is not affected. This relatively large broadband response relative to other transducers, its ease of use, and its sensitivity, make it ideal for simulated AE experiments such as those presented in section 2.1.1 as well as certain types of real AE studies. It is possible, however, that real AE from a given material have higher frequencies present than the range of this transducer [45]. If this is the case, recorded AE waveforms will be distorted to some extent. None the less, this transducer will still give an indication of the AE activity in a material, although it may be somewhat qualitative.

A block diagram and photograph of the overall system is shown in Fig. 25. Filtering was accomplished with an electronic Model 3202 Krohn-Hite filter and the transient recorder used was the Nicolet Model 204-A

described earlier. It should be noted that electrical insulation from radio frequency noise was very important with this transducer, therefore, the grips, specimen, transducer and amplifier were enclosed in a conductive cage. Coaxial cables were then utilized to transfer the signal to the filter and transient recorder.

2.4 Microscopy of Deformation and Fracture

Specimens of all three types of HY steels were examined via both optical and scanning electron microscopy. In order to characterize their microstructures, specimens were metallographically polished, etched and examined prior to their deformation. Deformed specimens were examined prior to any disturbance of the previously polished surface and were then sectioned, repolished and sometimes etched in order to examine internal regions, especially for particle deformation and void formation. Specimens partially deformed as well as fractured specimens were examined in this manner.

Fracture surfaces of the various specimens were also examined. Due to its large depth of field, this was done primarily with the scanning electron microscope. In this way, the basic mode of fracture was determined for each type of specimen for the various tests as well as specific mechanisms occurring within

this mode of failure. Energy dispersive x-ray analysis was also employed in conjunction with the electron microscopy to determine approximate compositions of certain particles.

3. RESULTS AND DISCUSSION

The primary goal of this study, as previously stated, was to determine the AE characteristics of the three HY Naval alloy steels 80, 100 and 130. In conjunction with this, however, there were two secondary goals: (i) Test, modify and verify the performance of the new interferometric system built at APL as well as determine design and performance changes necessary for its future use and (ii) Study the deformation and fracture characteristics of the steels utilized in this study. It would be very beneficial at this time prior to presenting the results, to review the findings of workers who have studied the emission characteristics of various steels in the past.

3.1 Review of Acoustic Emission from Steel

Although AE work has not had the widespread interest as such classic topics as fracture mechanics, corrosion, etc. there are, nonetheless, excellent ongoing studies being conducted in the field. Workers at Harwell have investigated the emission from a variety of heat treatments of an A533B composition steel [87, 89]. Table II lists the composition of this material. They found that only a few of the wide range of operative deformation and fracture events generated detectable AE, even when using very sensitive recording

techniques. Heat treatments studied in this work were catagorized as one of two types. The first type involved austenitizing the specimens for 1 hour at 1000°C in a dynamic argon atmosphere and cooling them at different rates. The specimens were either quenched into iced brine at -10°C, 10% NaOH solution at room temperature, unstirred water or oil; or they were not quenched but allowed to air cool, or furnace cool (at ~50°C/hr). The second type of heat treatment involved water quenching specimens from 1000°C and then isothermally tempering them at 650 $\pm$ 5°C in argon for a time of 6 to 10,020 minutes followed by another water quench.

It was found that the four most rapid quench rates generated no significant AE prior to σ_{max} (i.e. necking) when deformed by conventional tensile elongation. It was concluded that this was due to the high dislocation density and small width of martensitic laths limiting the dislocation propagation distance to below a critical value required for detection. Air and furnace cooling gave increased levels of continuous type emission around yield which was correlated with the increase in the mean free distance of dislocation propagation. Various tempering treatments on the water quenched specimens had a large effect on the AE activity prior to σ_{max}. Little or no emission was

generated from very lightly tempered martensite. Prolonged tempering, however, resulted in a strong increase in emission as the quenched-in dislocation structure and lath boundaries were annealed out and the carbide spacing was increased. The authors concluded that the emission increase was due to the increased distances dislocations could move prior to being pinned in some manner. Calculations of distances necessary for detection of acoustic emission from dislocation motion were correlated with phase boundary distances measured microscopically, supporting their findings for the various treatments.

Emissions after σ_{max} were greatly affected by the variety of cooling rates on the austenitized steel. The two most rapidly quenched specimens generated very large amplitude emissions as final fracture was approached. The emissions were attributed to the formation of cleavage microcracks in the material. When the cooling rate was reduced slightly (by quenching into water) the AE activity was both reduced in energy and delayed, occurring closer to failure. It was concluded from quantitative determinations of crack parameters that cleavage microcrack formation was most likely the origin of AE for these specimens in this post σ_{max} region as well, although alternating shear may also have contributed to some degree. Neither the slow

cooled nor any of the tempered specimens generated any AE after σ_{max} except at the instant of final failure. These specimens failed essentially by ductile void coalescence.

The two mechanisms cited as AE sources for these steels were therefore dislocation motion and cleavage microcrack formation, depending on the heat treatment. These results are consistent with other studies by Harwell workers as well as with various other investigations [69,88,90,95]. Some discrepancies have been seen, however [91], and many times the details are not agreed upon.

A number of investigations have shown that particular steels under given loading conditions resulted in ductile crack initiation and propagation that also generated detectable AE, although it is generally accepted that the more ductile a material the less likely it is to emit detectable AE (brittle inclusions or intermetallics in a ductile matrix are a notable exception and will be discussed later). Clark [92], has investigated two pressure vessel steels utilizing a three point bending test and found that at critical values of the crack opening displacement, high energy emissions were detected. The crack propagation was associated with a shear linkage type of void coalescence rather than a truly ductile rupture (i.e.

knife-edge) of the microligaments between voids. Guz and Zotov [93] also recorded AE from cracks of varying degrees of ductility but, again, no investigation was made of a purely ductile rupture.

Somewhat less conspicuous AE sources than those due to crack propagation are those associated with intermetallic particles and inclusions. Decohesion of intermetallics as well as their fracture have been shown to cause AE to varying degrees by Jaffrey [94]. This investigation also showed the importance of the orientation and shape of these particles relative to the stress axis. In general, it was determined that AE from MnS inclusions was enhanced when they were elongated and lying perpendicular to the stress axis. Similar results were obtained by Ono, Huang and Hatano [95].

Fractured intermetallics were also determined to be the cause of AE by Bruchey [45] in his study of 304L stainless steel. Although the matrix deformed in a very ductile manner, the nature of the particle fracture appeared more brittle, giving rise to high frequency AE. The affect of intergranular versus intragranular fracture has also been investigated [96]. It was concluded that intergranular mechanisms such as grain boundary sliding produced relatively little emission in a grade 45 steel. Although not as pertinent

to the current investigation, stress corrosion cracking has also been shown to cause AE in certain steels [80].

As can be seen by this brief review of AE studies in various steels, many mechanisms have been found to be responsible. Even when modes of fracture are identical, it appears that different AE sources operate depending on slight variations in alloying constituents and/or loading conditions. There are, at present, no comprehensive guidelines to determine the emission characteristics of a material simply by studying its deformation and fracture even though some generalizations are possible (i.e. ductility generally decreases AE). The study presented here will determine the AE characteristics for the HY steels already mentioned and will compare these results to the findings of previous investigators.

3.2 Microscopy of Deformation and Fracture

Specimens were examined optically in three different ways: (i) They were polished and etched before deformation to document their microstructure, (ii) An external surface, polished prior to any deformation, was examined following the tests, and (iii) Internal sections were examined by mounting, grinding, polishing and in some cases etching the specimens

following deformation. Electron microscopy was utilized chiefly for the examination of fracture surfaces. Standard techniques and nomenclature utilized in the microscopic examination of deformation and fracture as well as microstructural investigations can be found in several excellent texts and review articles [97-102].

Microstructures of undeformed specimens, as revealed by Nital etchant, can be seen in Fig. 26. The quantity and variety of alloying constituents and the heat treatment resulted in a fairly broken, complex, microstructure. All three steels were of a tempered martensitic and bainitic microstructure. Lighter regions, comparable to free ferrite in a plain carbon steel, were clearly visible in the HY 80 and less apparent in HY 100 and HY 130 specimens. Prior austenite grains were decorated more heavily in the higher strength HY 100 and HY 130 as was seen most readily with the use of Picral etch (Fig. 27). This is because carbon and other alloying constituents congregated at grain boundaries during the austenitizing treatment. When quenched, they did not have time to disperse uniformly and therefore precipitated out preferentially at the prior austenite grain boundaries giving an excellent outline of these grains. The longer tempering time (and/or higher tempering temperature) of the lower strength alloy, HY 80, however, allowed the carbides to

redistribute throughout the matrix, essentially destroying the prior grain boundary outlines.

External surfaces were examined before, during (by interrupting the test), and after selected tests for each material. Both slip and, at higher strains, apparent phase boundary motion was seen on the surfaces of the specimens (Fig. 28). Specimens were also sectioned to view internal regions. The significant findings during this work were related to particle behavior and void formation during deformation. A low magnification micrograph near the fracture surface of a sectioned specimen illustrates the void mechanism of fracture (Fig. 29). The initiation of the relatively large voids visible at this magnification occurred in two primary ways. Initiation took place at a particle matrix interface (Fig. 30) or between two sections of a fractured particle (Fig. 31). These figures also show, in excellent detail, the mechanism of particle fracture which occurred during deformation. All three types of steels were very similar on these external and internal sections.

Although scanning electron microscopy was used to a limited extent in the above views of the specimens, it was generally employed most extensively for fracture surface observations. Examination of the fracture surfaces (pictured in Fig. 32) in conjunction with the

above information, revealed a great deal about the deformation and fracture processes which operated in these alloys. Large particles, generally found to be composed of MnS or FeNi by energy dispersive x-ray analysis, were seen situated in the largest voids. Intermediate size voids were also seen to contain particles, much smaller in size, believed to be carbides. Finally, still smaller voids were observed interspersed between these larger voids and appeared to contain no particles. This could be due to the resolution of the electron microscope and there might have been small, perhaps coherent, particles nucleating these voids. Triple points, where three grains meet, as well as regular grain boundaries and other defect structures such as dislocation cell walls and pile-ups may also have been void initiation sights as they are generally believed to be in purer materials. In the HY steels, they would take part in void initiation once the impure regions containing carbides and intermetallics had been "used up" by primary void nucleation earlier in the deformation.

The sequence of events leading to rupture began with the formation of the largest voids visible in the fracture surface, which then acted as stress concentrators causing necking and subsequent formation of progressively smaller voids. During this time, voids

were growing and coalescing as the microligaments between them got smaller and fewer in number. These microligaments finally necked down to a knife edge as if each was a small, single phase, micro-tensile specimen, thus demonstrating the extreme ductility of the matrix material. At the instant of fracture, these microligaments separated simultaneously or consecutively, within fractions of a second. Again, all three steels were qualitatively identical in the appearance of their fracture surfaces. No shear linkage of voids was observed, indicating the truly ductile nature of their deformation and fracture.

3.3 Acoustic Emission Measurements

3.3.1 System Verification

A major problem in AE work has been the ambiguity associated with what has generated a recorded waveform. For instance, was it truly AE from the specimen or was it noise from the experimental system or the room, etc. Many precautions were taken in this investigation to ensure that the detection systems were only recording AE from the specimen, (i.e. the specimens were acoustically isolated, experiments were performed on an air table, etc.). It was still necessary to have a way to check the system, to determine if these precautions were effective before plunging

into AE tests on materials with unknown characteristics. This was done by testing known emitters and known non-emitters in the system as control specimens. The non-emitters were simply materials which were previously loaded and were known to experience the Kaiser Effect on reloading.

For the micro-tensile and bend tests, zinc and 7075 T6 aluminum were used as known emitters [75] to check the system. HY 80, found to exhibit the Kaiser Effect, was loaded several times prior to testing and used as the non-emitter. For the macro-tensile tests, 2024 and 7075 T6 aluminums were used as emitters and non-emitters (upon reloading) [75] as well as HY 80 as a non-emitter after multiple loadings. These control tests verified the integrity of the systems employed in this investigation, demonstrating that AE could be detected and that extraneous noise was not.

3.3.2 Acoustic Emission Waveforms

Micro-tensile specimens of each of the steels were found to emit several different types of waveforms (Fig. 33). The AE during these tests, however, was sporadic and unpredictable, with some specimens from each type of steel emitting no AE at all. The most consistent type of waveform emitted was the single

spike shown in Fig. 33a. Many specimens emitted this type of AE, several of which are shown in Fig. 34.

A problem which arose during these tests was connected with the static "tracking" capabilities of the interferometer. As previously stated, the path stabilization loop tracks a set of fringes utilizing a PZT driven reference mirror in order to compensate for specimen drift due to a Poissons ratio effect. When the PZT reaches a limiting extension or compression it resets to its zero position and begins tracking again. During this resetting, no AE can be detected. It is possible that as much as 30% of the AE during many of the micro-tensile tests in this investigation may have been lost in this manner. Although not in time for the present investigation, design changes have since decreased this percentage by up to an order of magnitude.

Due to the loading configuration, this was not a problem during the bend tests. The same results were obtained, however, with respect to the sporadic nature of the AE, with the exception of those emissions occurring directly prior to failure. In nearly every test of all three types of steels a series of emissions was detected immediately prior to final fracture of the specimens (Fig. 35). A load drop was generally observed after each emission until directly after the final AE,

at which point the material fractured.

Macro-tensile tests were initially conducted due to the sporadic nature of the AE activity during micro-tensile tests. It was believed this may have been a volume effect (see section 3.3.3 for further discussion of volume effect), therefore, large tensile specimens (Fig. 23) were tested, as previously discussed, in a floor model Instron tensile machine utilizing the new NBS transducer as the detector (see section 2.1.2). Suspicions of a volume effect were confirmed when these large specimens were found to emit consistently in certain portions of their loading. Identical results were obtained for each steel, HY 80, HY 100 and HY 130, and typical AE behavior is shown superimposed on load elongation curves in Fig. 36. Each tic mark along the x axis corresponds to one AE. The waveforms (Fig. 37) were oscillatory in nature and those occurring prior to yielding could be catagorized as continuous type. The waveforms are believed to be distorted a fair amount by the specimen geometry and the detection system. Qualitatively, however, the results are very significant. The specimens generated anywhere from 10 to 35 detectable emissions prior to yielding, were then quiet until directly prior to fracture, at which time, one to seven events were detected before final separation.

3.3.3 Sources of Acoustic Emission

The AE from the three HY steels studied in this investigation were very similar for each and appear to be caused by two distinct mechanisms with the exception of some sporadic emissions. One mechanism, beginning at the onset of loading and ending prior to specimen yielding, gave rise to what will be termed type I emissions, while the second mechanism, operating directly prior to failure, caused what will be referred to as type II emissions. These type II emissions, which occurred in both the bend tests and macro-tensile tests, were caused by consecutive ductile rupture of the microligaments between voids just prior to complete material separation. This may be considered a kind of ductile crack propagation but is not the same ductile crack propagation as that involving the shear linkage of voids discussed earlier (see sections 3.1 and 3.2). The apparent number of microligament ruptures involved in each AE event observed indicate that individual ligament ruptures would generate AE amplitudes below noise levels. This suggests that in order to generate a detectable AE the superimposed energies of many ruptures occurring consecutively (or simultaneously) were necessary. This implies that there was some critical "crack volume" necessary for generating a minimum detectable

elastic wave. Quantitative results from previous investigations related to this discussion are shown in Appendix B.

The mechanism causing type I emissions is somewhat less conspicuous. Their location on the load-elongation curve, however, suggests that they were related to dislocation motion in some way. Various investigators, as discussed earlier (section 3.1), have attributed AE in this region to the sustained easy glide of dislocations in tempered steel microstructures. In this case, there was some critical mean free path for dislocation motion below which a single dislocation would not be detected. Appendix C contains the details of the calculation of this minimum path length. This distance was approximately 4500 μm for the macro-tensile system in the current study. The prior austenite boundaries were on the order of 30 μm, indicating that dislocation motion could not be detected if these boundaries act as barriers to the dislocation motion. This could be overcome, however, in two separate ways: (i) The prior austenite boundaries may not have been barriers to dislocation motion and therefore dislocations could have much longer glide lengths than these boundaries suggest or (ii) If there were many sources acting simultaneously such that the sum of the distances they travelled was

greater than 4500 μm (i.e. 150 dislocations at 30 μm each - not an exceptionally large number for dislocation motion) they could have generated detectable emission. In fact, it is very likely that this dislocation glide mechanism was the cause of the AE in this region for two important reasons: (i) Microscopy indicated a severe lack of additional mechanisms operating in the load regime in which this AE was detected and (ii) Dislocation theory tells us that at the pre-yield loads at which much of this AE was detected, the easy glide of mobile dislocations should be the only active mechanism.

The final problem, therefore, becomes the origin of the sporadic signals recorded during the micro-tensile and bend tests. Some were undoubtedly due to the same dislocation motion believed to cause the type I emissions in the macro-tensile tests. The relative inconsistency of these signals in the micro as opposed to macro-tensile specimens can be attributed to a volume effect (the gauge volume of the macro-tensile specimens is over 1,000 times larger than the micro-tensile gauge volume) manifesting itself in two ways: (i) As has been well documented in the literature, ductile materials generate relatively few emissions in general, therefore, the very small deforming volume in the micro-tensile tests could lead to anomolous

results due simply to the statistical probability of an event of high enough energy being present in the total number of events which occur and (ii) The small deforming volume made it much less probable that several low energy events would occur simultaneously, their energies thereby adding to make a single detectable AE.

Although there is no direct proof, a logical correlation is that the most consistent waveforms in the micro-tensile tests (i.e. the spike-like waveforms) were due to the same mechanism as the consistent type AE in the macro-tensile tests. The only plausible argument against this reasoning is that the emissions in the micro-tensile tests were not of the continuous type generally recorded for this mechanism of dislocation motion. To the author's knowledge, however, no one has ever recorded these types of emissions with a broadband system! It may be that they appear to be continuous to the narrow band systems, but are actually discrete waveforms, only detectable as spikes by a higher frequency, broadband system.

The possibility of these spike-like waveforms (Fig. 34) having the origin of dislocation motion, as was deduced for the pre-yield macro-tensile AE, is supported by returning to the idea of a minimum detectable mean free path for dislocation motion.

Previous investigators have found this distance to be as low as 100 μm using a narrow band detection system. This calculation cannot be carried out for the micro-tensile tests and the broadband system (as it was for the macro-tensile tests) used in this investigation because of the violation of the assumption that the mean free path is much smaller than the smallest wavelength AE detected and much smaller than the detector to source distance. If, however, the system is truly broadband with respect to the AE frequency generated by the dislocation motion, then the duration of the waveforms caused by this motion times the dislocation velocity will yield an experimental, rather than calculated, mean free path or distance travelled by the dislocations detected. When this is determined for a dislocation traveling 200 m/sec (a velocity utilized by investigators in the past [31] and believed to be reasonable) and whose lifetime is assumed to be the duration of the spike-like waveforms detected during the micro-tensile tests, a value for the mean free path of 150 μm is found - a very reasonable number.

As already stated, there is no direct proof for the assumption that these spike-like waveforms are due to the same dislocation motion sources which appear to be sources in the macro-tensile tests. This

possibility certainly warrants further investigation with a broadband system, however, in order to determine if there is supporting evidence found in other materials for this idea of continuous emission being made up of discontinuous bursts which could be detected with large enough bandwidths.

Additional spurious signals recorded during micro-tensile and bend tests, not due to dislocation motion, most probably can be attributed to inconsistencies in the microstructures such as unwanted inclusions. This has been concluded by other investigators when sporadic signals were observed [87,90,91]. It is also very beneficial to note the deformation and fracture mechanisms observed in these steels which did not cause AE, even though they were quite abundant and are known to be sources of AE in other materials (see section 3.1). For instance, many fractured and decohered particles were observed in all three steels. Also, a great deal of slip and phase boundary motion was noted. These mechanisms, however, did not occur at the proper points and/or in the correct quantities to have caused the AE in this study. The author knows of no concrete explanation of the variables controlling the generation of detectable AE by any of these mechanisms. Although it was found they did not generate detectable AE in the current investigation or

in certain previous studies, other investigators have found that these events did give rise to detectable AE. Section 3.1 cites these various investigations and in many cases it is seen that the deformation characteristics of the materials as well as the loading conditions are very similar.

4. CONCLUSIONS

The modified Michaelson interferometric system has been demonstrated to be effective in the detection of AE although an increase in its dynamic stabilization amplitude was found to be necessary if it is to be used in conjunction with conventional tensile machines. The mechanisms of deformation and fracture of the three Naval steels HY 80, HY 100 and HY 130, have been documented as well as their emission characteristics under tensile elongation and bend type loading. AE occurring prior to yield, attributed to dislocation motion, and AE immediately prior to failure due to the consecutive rupture of microligaments in the material were detected in all three steels to approximately the same degree. These results suggest that the utilization of AE as a means of monitoring the integrity of a structure made from these materials is of limited value. The AE which occurs in the elastic region is of little relevance because structures are designed to deform elastically and therefore the detection of this AE is not an indication of a problem. If it were concentrated at or near yield, on the other hand, it could be quite beneficial but it occurs earlier than this in its load history. In contrast, the AE occurring immediately prior to failure is too

late to be of great value in most situations. By the time these AE events are detected, catastrophic failure may be already occurring. If, however, it is known that these ductile cracks will initiate and propagate stably prior to catastrophic failure these emissions could be of use. Great caution should be exercised in this case, however, and the loading situation should be well characterized to be certain that a detectable, stable crack propagation will, in fact, occur.

APPENDIX A

Catalogue of Waveforms Detected During Specimen Geometry Work

This appendix contains several simulated AE waveforms detected after they propagated through micro-specimens of various cross-sections in order to investigate specimen geometry effects (see section 2.1.1). Figure A1 is an undistorted standard waveform to which the others were compared. It can be seen that the waveforms propagated through specimens whose thickness is equal to or less than their width and is approximately 0.075 in or less contain relatively little distortion (Figs. A2-A4). Specimens not meeting these requirements, however, appreciably distort some portion of the initial, first arriving, waveform (Figs. A5-A8).

APPENDIX B

Quantitative Discussion of Crack Growth Sources

For a small, horizontal crack of cross-sectional area A, crack face separation 2δ, and volume V under mode I loading, the strain field at a distance h, much greater than the crack dimensions, is approximately that of an edge dislocation loop of area A and effective Burger's vector 2δ. The area under the longitudinal pulse emanating from this crack is given by [88]:

$$S = \frac{V}{2\pi c_1 h} \tag{B1}$$

With this result, the minimum detectable crack diameter can then be determined as has been done by workers at Harwell [87] in the manner described below.

Assuming a parabolic increase in crack area with time, the peak amplitude of the longitudinal component is:

$$x = \frac{V}{c_1 \tau h} \tag{B2}$$

where c_1 is the longitudinal wave speed. This allows for the determination of the minimum detectable crack volume provided τ, its duration, is known. It is more usual, however, to express a crack in terms of its length. Assuming the crack behaves in a linear

elastic manner during growth we can express the volume of the crack having an ellipsoidal shape as:

$$V = \frac{4\pi a^2 \delta}{3} \tag{B3}$$

where a is the radius of an assumed circular crack of midplane area πa^2. Under elastic loading the crack face displacement at the center of the crack, δ, is a function of crack radius and applied stress:

$$\delta = \frac{2(1-\nu^2)\sigma a}{E} \tag{B4}$$

where E is Young's modulus and ν is Poisson's ratio. Substituting for V and δ, equation B2 becomes:

$$x = \frac{8\pi a^3 (1-\nu^2)\sigma}{3c_1 \tau hE} \tag{B5}$$

Assuming a constant radial crack velocity, v, so that $a = v\tau$ and rearranging (B5) gives:

$$a_{min} = \sqrt{\frac{3c_1 Eh\, x_{min}}{8\pi v(1-\nu^2)\sigma}} \tag{B6}$$

In the Harwell investigation where this theory was developed [87], the material exhibited brittle microcrack formation and the smallest detectable crack diameter was calculated as $2a_{min} = 10^{-6}$m utilizing values of $E = 2 \times 10^{11}$ Pa, v = 500 m/sec, $\nu = 0.3$, $\sigma = 10^9$ Pa, h = 0.03m, c_1 = 5960m/sec and x_{min} =

10^{-14} m for the material and system employed in their study. In the current investigation a problem arises with the assumption of linear, elastic behavior during crack growth due to the fact that the HY steels studied here did not exhibit brittle failure but rather fractured by a very ductile crack growth mechanism as described earlier (section 3.2). None the less, if it is assumed that this linear elastic behavior will generate an "order of magnitude" result for the minimum detectable crack length of the crack growth occurring directly prior to failure in the macro-tensile tests, a rough value of the crack radius, a_{min}, can be calculated.

This calculation cannot be carried out for the crack growth detected during the bend tests because the close proximity of the detector to the crack does not allow for approximating the crack strain field as that of an edge dislocation as mentioned early in this section. We can, however, determine the crack velocity in these tests by the width of the first arriving longitudinal pulse, since the broadband detection system was utilized in these tests. For a test in which separation occurred by only one propagation, a is $\sim 8 \times 10^{-4}$ m and τ can be seen in Fig. B1 to be approximately 1 μsec. Therefore:

$$v = a/\tau = 800 \quad \text{m/sec}$$

Assuming this same propagation velocity occurs in the macro-tensile tests and using $E = 4 \times 10^4$ MPa, $\nu = 0.3$, $\sigma = 2 \times 10^2$ MPa,* $h = 0.063$ m, $c_1 = 5960$ m/sec and $x_{min} \cong 10^{-12}$, it is found that $a_{min} = 3.5 \times 10^{-6}$ m. Although this appears to be a reasonable value at first, it is actually much smaller than examination of the data suggests a_{min} should be. For example, only several AE waveforms, on the average, were detected during this final crack propagation. If seven emissions were detected (the upper limit in the actual tests) just above the noise level, the calculated a_{min} says that seven different crack events totalling 4.9×10^{-5} m occurred. In order to propagate across the smallest dimension of the specimen's cross-section (4.8×10^{-3} m) it would be expected that ~95 (rather than seven!) of these events would occur. There are two different reasons, however, that the calculated a_{min} is more accurate than this indicates: (i) There were some AE events "missed" during a test while the transient recorder is rearming. Therefore if two emissions occurred very close to each other but outside the window of the recorder (0.2 msec), only the first

*from load at fracture divided by final cross-sectional area since AE occurred very close to failure

would be recorded and (ii) The amplitudes of the AE events recorded during this crack propagation (Fig. 37b) were not "just" detectable but actually had an amplitude well above the noise level indicating that the crack by which they were generated, propagated farther than the calculated a_{min}. This makes the small a_{min} more "believable" even though the number of recorded events was relatively small. Therefore, although a linear elastic crack propagation was assumed, thereby distorting the final value calculated for the minimum detectable crack length for the system and material utilized in the current investigation, an apparently reasonable length was obtained.

APPENDIX C

Minimum Mean Free Path for Detection of Dislocation Glide

Calculations by workers at Harwell [87] allow for an approximate determination of the minimum distance or mean free path which must be traversed for a single dislocation to be detected by a given system. Considering a glissile dislocation loop of Burger's vector b, expanding from an initial radius of zero to some final radius a, the time dependence of the surface displacement at the epicenter of a half space has been previously evaluated [48]. It is assumed that the loop is inclined 45° to the tensile axis and that the final radius is much smaller than the source to detector distance and the minimum wavelength detected, so that the loop may be considered a point source. The early part of the waveform is dominated by a pulse, due to the arrival of a longitudinal wave, the area under which is given by:

$$S = \frac{c_2^2 b\ A}{2\ \pi\ h c_1^3} \qquad \text{(C1)}$$

where c_1 and c_2 are the speeds of the longitudinal and transverse waves, respectively, in the material, h is the depth of the loop below the detector and A is the final loop area.

If the dislocation loop grows at constant radial velocity, v, so that the duration over which it grows:

$$\tau = a/v \tag{C2}$$

then τ will correspond to the width of the longitudinal wave pulse. If the height of the pulse is x, then for a loop area that grows parabolically in time to its final value of πa^2, the initial surface displacement commences with a ramp of slope x/τ. Thus:

$$x = \frac{b\ a\ v\ c_2^2}{hc_1^3} \tag{C3}$$

If x_{min} is the smallest detectable surface displacement, then the smallest detectable dislocation loop must have grown to a radius a_{min}:

$$a_{min} = \frac{hc_1^3\ x_{min}}{b\ v\ c_2^2}$$

For steel, c_1 = 5960 m/sec and c_2 = 3200 m/sec. Assuming a Burger's vector of $\sim 3 \times 10^{-10}$ and a dislocation velocity of 200 m/sec we find that a_{min} is approximately 4500 μm (since $x_{min} \cong 10^{-12}$ m and $h = 1.27 \times 10^{-2}$ m for the dislocation motion nearest the detector). Therefore, if a single dislocation loop expands $\sim$4500 μm it would be just detectable. Loops of smaller radius could be detected according

to this model if they either grew at greater velocity or if n loops situated near one another grew simultaneously so that their combined radii exceed a_{min}. In the latter case,

$$a_{min} = \frac{hc_1^3 x_{min}}{b\ n\ v\ c_2^2} .$$

REFERENCES

1. L. Obert, U. S. Bur. Mines, Rep. Invest. R1-3555 (1941).

2. L. Obert and W. Durall, U. S. Bur. Mines, Rep. Invest. R-3654 (1942).

3. L. Obert and W. Duvall, U. S. Bur. Mines, Rep. Invest. R1-3797 (1945a).

4. L. Obert and W. Duvall, U. S. Bur. Mines, Rep. Invest. R1-3803 (1945b).

5. L. Obert and W. Duvall, U. S. Bur. Mines, Bull. 575, (1957).

6. L. Obert and W. Duvall, U. S. Bur. Mines, Rep. Invest. R1-5882 (1961).

7. E. A. Hodgson, "Dominion Observatory Rockburst Research 1938-1945," Dept. of Mines and Technical Surveys, Canada, Dominion Observatories Rept. (1958).

8. K. Hodgson and N. C. Jough, Failure and Breakage of Rock, C. Fairhurst, editor, p. 194 AIME, New York (1967).

9. A. E. Lord, Physical Acoustics, W. P. Mason and R. N. Thurston, editors, Vol. 11, p. 389 (1975).

10. J. Kaiser, Ph.D. Thesis, Technische Hochschule, Munich (1950).

11. B. Schofield, ASD-TDR-63-509, Lessells and Associates, Inc., Waltham (1963).

12. C. Tatro, Progress Report, College of Engineering, Michigan State University, East Lansing (1959).

13. B. Schofield, AF 33 (616)-5640, Lessells and Associates, Inc., Boston (1960).

14. B. Schofield, Proc. of Symposium on Physics and NDT, pp. 63-82 (1963).

15. H. L. Dunegan and A. S. Tetelman, Research/ Development, p. 20, May (1971).

16. A. A. Pollock, Acoustics and Vibration Progress, R. W. B. Stephens and H. G. Leventhall, editors, Vol. 1, pp. 53-54 (1974).

17. P. H. Hutton and R. N. Ord, "Acoustic Emission," R. S. Sharpe, editor, Research Techniques in NDT, pp. 1-30, (1970).

18. R. G. Liptai, D. O. Harris, and C. A. Tator, editors, ASTM STP 505, ASTM, Philadelphia, Pa. (1972).

19. J. C. Spanner, Acoustic Emission, Techniques and Applications, Intex Publ. Co., Evanston, Ill. (1974).

20. J. C. Spanner and J. W. McElroy, editors, Monitoring Structural Integrity by Acoustic Emission, ASTM STP 571 (1975).

21. H. L. Dunegan and W. F. Hartman, editors, "Advances in Acoustic Emission, Proc. Int. Conf. Acoustic Emission," ASNT (1981).

22. A. Green, C. Lockman and R. Steels, Modern Plastics, Vol. 41, p. 137 (1964).

23. K. Northvest, Weld. J. (New York), Vol. 45, p. 173-S (1966).

24. C. K. Day, Rep. BNWL-902, Batelle-Northwest, Richland, Washington (1969).

25. W. D. Jolly, Weld. J. (New York), Vol. 48, p. 21 (1969).

26. C. E. Hartbower, W. G. Reuter, C. F. Morais and P. P. Crimmins, Amer. Soc. Test. Mater., Spec. Tech. Publ. Vol. 505 (1972).

27. A. E. Brown and R. G. Liptai, Amer. Soc. Test. Mater., Spec. Tech. Publ., Vol. 505 (1972).

28. G. R. Speich and R. M. Rischer, Amer. Soc. Test Mater., Spec. Tech. Publ., Vol. 505 (1972).

29. A. G. Beattie, Bull. Amer. Phys. Soc. [2], Vol. 16, p. 385 (1971).

30. P. H. Hutton and D. L. Parry, Mater. Res. Stand., Vol. 11, p. 25 (1971).

31. D. L. Parry, "Acoustic Emission Integrity Analysis of Pressure Vessels and Piping," Jersey Nuclear Co., Richland, Washington (1971).

32. D. O. Harris and H. L. Dunegan, Tech. Rep. DRC 71, Dunegan Res. Corp., Livermore, California (1971).

33. P. H. Hutton, "Acoustic Emission Monitoring of Aircraft to Detect Fatigue Crack Growth," Batelle Pacific Northwest Lab., Contract No. N62269-80-C-0243 (1982).

34. R. B. Engle, Ph. D. Thesis, Michigan State University, Ann Arbor (1967).

35. R. T. Sedgwick, J. Appl. Phys., Vol. 39, p. 1728 (1968).

36. H. L. Dunegan and D. O. Harris, Ultrasonics, Vol. 7, p. 160 (1969).

37. O. Buck, Int. J. Fracture Mechanics, IJFMA, Vol. 8 (1), pp. 121-124, March (1972).

38. D. M. Egle, University of Oklahoma, Department of Aerospace, Mechanical and Nuclear Engineering, Norman, Oklahoma. "Fracture and Flaws, Proceedings of the 13th Annual Symposium," pp. 51-54 (1973).

39. D. M. Egle, J. R. Mitchell, K. H. Bergey, and F. J. Appl, Advances in Instrumentation, Vol. 27 (2) (1972).

40. S. R. Buxbaum, C. L. Friant, S. E. Fick and R. E. Green, Air Force Office of Scientific Research (AFOSR) Scientific Report, Contract No. F44620-76-C-0081, July (1979).

41. R. A. Kline, R. E. Green, C. H. Palmer, J. Appl. Phys. Vol. 52 (1), p. 141 (1981).

42. C. E. Hartbower and P. O. Crimmins, "Stress-Wave Emissions from Slow Crack Growth: A Review of Aerojet-General Research," Aerojet-General Corporation, Sacramento, California (1970).

43. D. G. Chakrapani and E. N. Pugh, Metallurgical Transactions A, MTTAB, Vol. 6A (6), pp. 1155-1163, June (1975).

44. B. Cox, Corrosion, CORRA, Vo. 30 (6), pp. 191-202, June (1974).

45. W. J. Bruchey, Ph.D. Thesis, Johns Hopkins University, Baltimore (1980).

46. S. L. McBride, J. W. MacLachlan and B. P. Paradis, J. of NDE, Vol. 2, No. 1, p. 36 (1981).

47. H. N. G. Wadley, C. B. Scruby and G. Shrimpton, Acta Metallurgica, Vol. 29, pp. 399-414 (1980).

48. C. B. Scruby, H. N. G. Wadley and J. E. Sinclair, AERE-R 9643, AERE Harwell, Oxfordshire, England, June (1980).

49. H. N. G. Wadley, C. B. Scruby, D. Stokham-Jones, K. L. Rusbridge, J. H. Worth and J. A. Hudson, AERE-R 10362, AERE Harwell, Oxfordshire, England, Dec. (1981).

50. H. N. G. Wadley and C. B. Scruby, AERE-R 10353, AERE Harwell, Oxfordshire, England, Dec. (1981).

51. T. F. Drouillard, Acoustic Emission, A Bibliography with Abstracts, F. J. Laner, editor, Plenum Publishing Corp., IFI/Plenum (1979).

52. N. Hsu and S. Hardy, Elastic Waves and Non-Destructive Testing of Materials, Y. H. Pao, editor, Vol. 29, pp. 85-106, ASME, New York (1978).

53. I. Lanchon-Magnin, P. Fleischmann, D. Rouby and R. Goutte, Ultrasonics, pp. 18-24, Jan. (1982).

54. J. A. Simmons and R. B. Clough, "Proc. of Int. Conf. on Dislocation Modelling in Physical Systems," J. Hirth and M. Ashby, editors, Scripta Metallurgica (1981).

55. J. E. Michaels, T. E. Michaels and W. Sachse, Materials Evaluation, Vol. 39, Oct. (1981).

56. W. Sachse and A. Ceranoglu, Ultrasonics International 1979, Conference Proceedings, IPC Science and Technology Press, Ltd., Guildford, England, pp. 138-145 (1979).

57. R. Weisinger, Master's Essay, The Johns Hopkins University, Baltimore (1979).

58. R. E. Green, Jr., Mechanics of Nondestructive Testing, W. W. Stinchcomb, editor, Plenum Publishing Corp., pp. 55-76 (1980).

59. P. M. Proctor, Jr., J. Acoust. Soc. Am., Vol. 71 (5), p. 1163, May (1982).

60. R. G. Liptai, D. O. Harris, R. B. Engle and C. A. Tatro, Int. J. of NDT, Vol. 3, pp. 215-275 (1971).

61. R. A. Kline, R. E. Green and C. H. Palmer, J. Acoust. Soc. Am., Vol. 64 (6) (1978).

62. N. Hsu, J. Simmons and S. Hardy, Materials Evaluation (Research Supplement). Vol. 35, p. 100 (1977).

63. L. Graham and G. Alers, ASTM STP 571, Monitoring Structural Integrity by Acoustic Emission, 11, ASTM, Philadelphia (1972).

64. R. E. Green, Jr., B. B. Djordjevic, C. H. Palmer and S. E. Fick, Proc. of Nat. Symp. on Applications of Lasers to Materials Processing, April (1979).

65. F. R. Breckenridge, C. E. Tschiegg and M. Greenspan, J. Acoust. Soc. Am., Vol. 57 (3), March (1975).

66. B. B. Djordjevic, Ph.D. Thesis, The Johns Hopkins University, Baltimore (1979).

67. R. A. Kline, Ph.D. Tehsis, The Johns Hopkins University, Baltimore (1978).

68. C. H. Palmer and R. E. Green, Jr., Nondestructive Evaluation of Materials, J. J. Burke and V. Weiss, editors, Plenum Publishing Corp., pp. 347-378, (1979).

69. H. N. G. Wadley and C. B. Scruby, Acta. Met., Vol. 27, p. 613 (1979).

70. S. E. Fick and C. H. Palmer, Applied Optics, Vol. 17 (17), p. 2686 (1978).

71. C. H. Palmer and S. E. Fick, Proc. of Southeastcon. '79, p. 191 (1979).

72. M. Arrington, British J. of NDT, Vol. 17, p. 10 (1975).

73. Y. Nakamura, C. Veach and B. McCauley, ASTM STP 505, Acoustic Emission, p. 164, ASTM, Philadelphia (1971).

74. T. Imanaka, K. Sano and M. Shinizu, Crystal Lattice Defects, Vol. 4, p. 57 (1973).

75. J. Duke, Master's Essay, The Johns Hopkins University, Baltimore (1976).

76. F. Higgins, Ph.D. Thesis, University of Denver, Denver (1977).

77. L. Graham and G. Alers, Materials Evaluation, Vol. 32, p. 31 (1974).

78. L. Graham and G. A. Alers, Ultrasonics Symposium Proceedings, Inst. Electrical and Electronics Engineers, pp. 18-20 (1972).

79. M. Bassim, D. Hay and J. Canteigne, Materials Evaluation, Vol. 34, p. 109 (1976).

80. R. Kline, Master's Essay, The Johns Hopkins University (1975).

81. K. Ono, R. Stern and M. Long, ASTM STP 505, Acoustic Emission, p. 152, ASTM, Philadelphia (1971).

82. K. Ono and J. Ucisik, Materials Evaluation, Vol. 34, p. 32 (1976).

83. J. T. Glass, S. Majerowicz and R. E. Green, Jr., DTNSRDC Report SME 81-44, July (1981).

84. H. Lamb, Philos. Trans. R. Soc., Vol. A 203, p. 1-42 (1904).

85. H. M. Mooney, Bull. Seismol. Soc. Am., Vol. 64, pp. 473-491 (1974).

86. J. F. Kalthoff, Workshop-Dynamic Fracture Modeling and Quantitative Analysis, Sponsored by: Ballistic Research Laboratory ARRADCOM, Army Research Office, Army Reserach Office-Europe, May (1982).

87. C. B. Scruby, C. Jones, J. T. Titchmarsh and H. N. G. Wadley, AERE-R 9645, AERE Harwell, Oxfordshire, England, Aug. (1980).

88. C. B. Scruby, H. N. G. Wadley and G. Shrimpton, AERE-R 9644, AERE Harwell, Oxfordshire, England (1980).

89. R. B. Clough and H. N. G. Wadley, AERE-R 10400, AERE Harwell, Oxfordshire, England, Dec. (1980).

90. N. V. Novikov and V. E. Vainberg, Strength of Materials, Vol. 9 (12), pp. 1467-1471 (1977).

91. K. Sano, T. Imanaka, T. Funakishi and K. Fujimoto, Proc. Second Acoustic Emission Symposium, Tokyo, Japan, pp. 23-45 (1974).

92. G. Clark, Mat. Res. Labs., Dept. of Defense, Melbourne, Australia, Ninth World Conference on NDT (1979).

93. I. S. Guz and A. D. Zotov, Strength of Materials, Vol, 6 (4), pp. 461-463 (1974).

94. D. Jaffrey, University of Newcastle, Newcastle, Australia, Ninth World Conference on NDT (1979).

95. K. Ono, G. Huang and H. Hatano, University of California, Los Angeles, Eighth World Conference on NDT (1976).

96. V. N. Sosedov and V. E. Vainberg, Industrial Laboratory, Vol. 44 (3), pp. 375-378, Mar. (1978).

97. A. S. Tetelman and A. J. McEvily, Jr., Fracture of Structural Materials, John Wiley and Sons, Inc., publishers (1967).

98. B. M. Straus and W. H. Cullen, editors, Fractography in Failure Analysis, ASTM STP 645, ASTM Philadelphia (1977).

99. J. L. McCall and P. M. French, Metallography in Failure Analysis, Plenum Press, publisher (1978).

100. D. Broek, Int. Metallurgical Reviews, Vol. 19, pp. 135-182 (1974).

101. O. Johari, IITRI Metals Research Division, Fracture Handbook, Failure Analysis of Metallic Materials by Scanning Electron Microscopy, IIT Research Institute, Chicago, Illinois (1979).

102. A. F. Szewczyk, U. S. Department of Energy, Contract No. DE-ACO2-80ER 10556, Tech. Rep. No. 86, Nov. (1981).

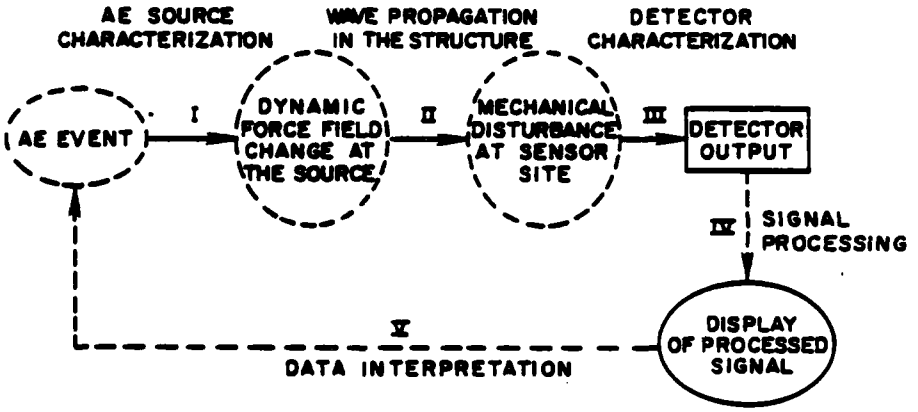

Fig. 1. Chain of AE signal analysis (after Hsu [52]).

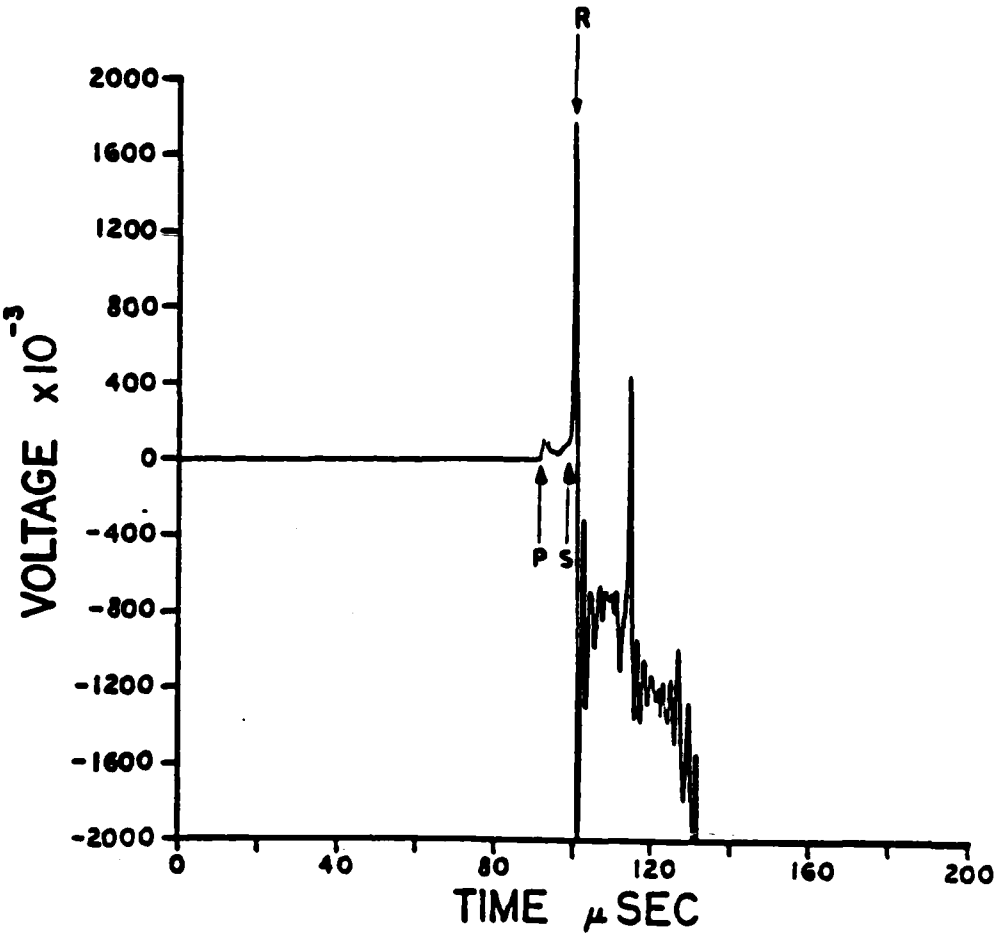

Fig. 2. Glass capillary fracture as detected by NBS transducer.

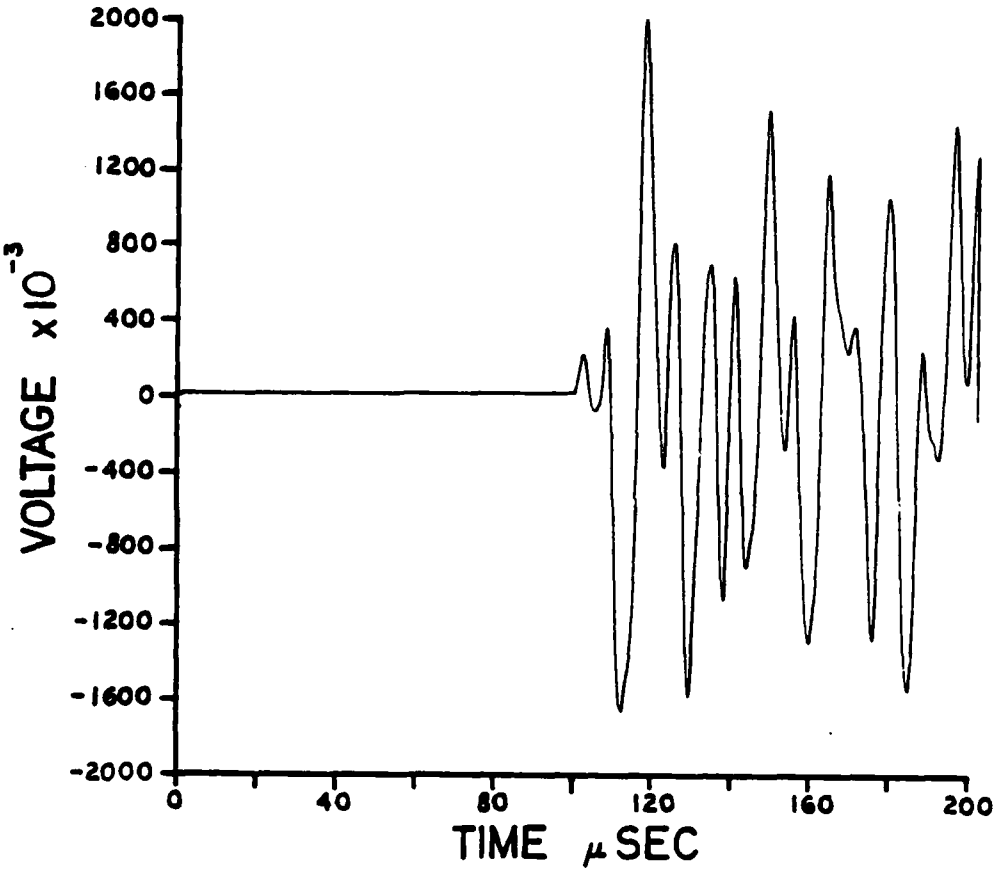

Fig. 3. Glass capillary fracture as detected by commercial transducer.

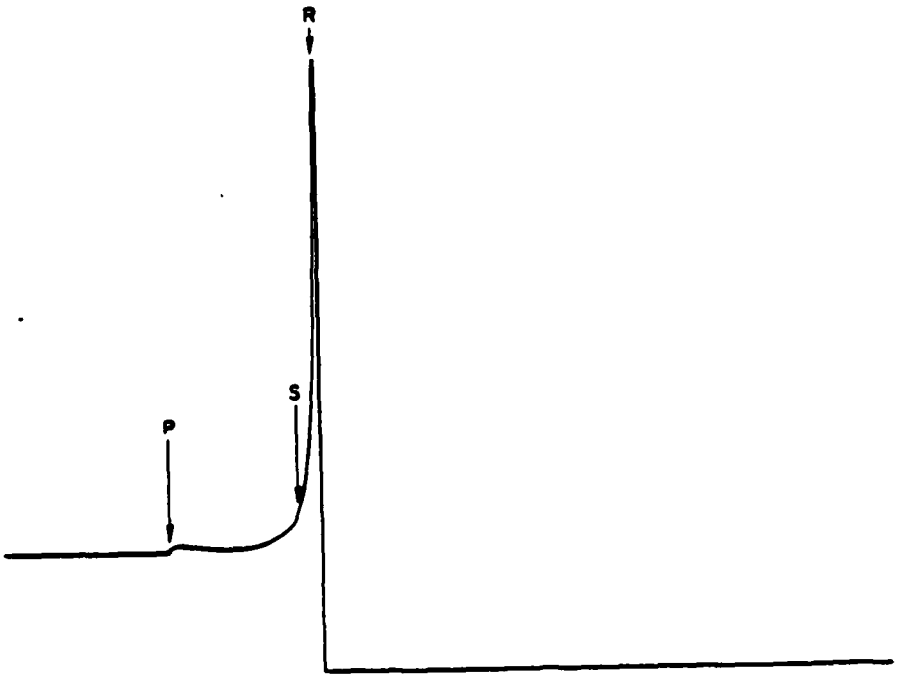

Fig. 4. Theoretical waveform of step unloading point source on the surface of an infinite half space when detected on this same surface.

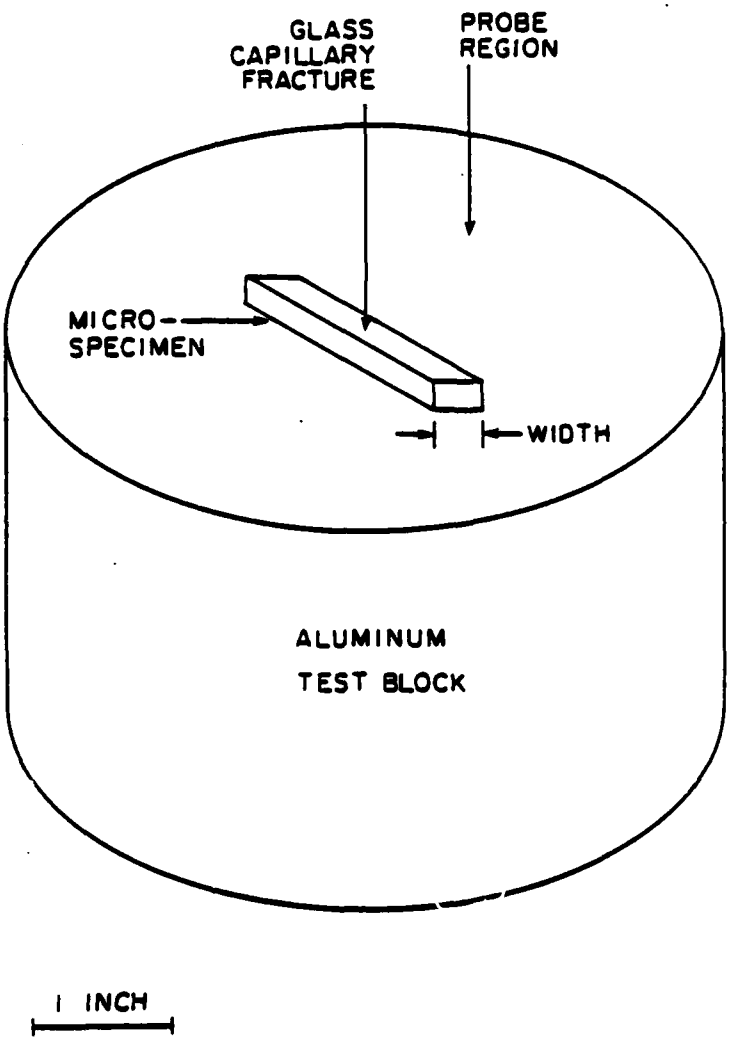

Fig. 5. Schematic of testing arrangement utilized in specimen geometry investigation.

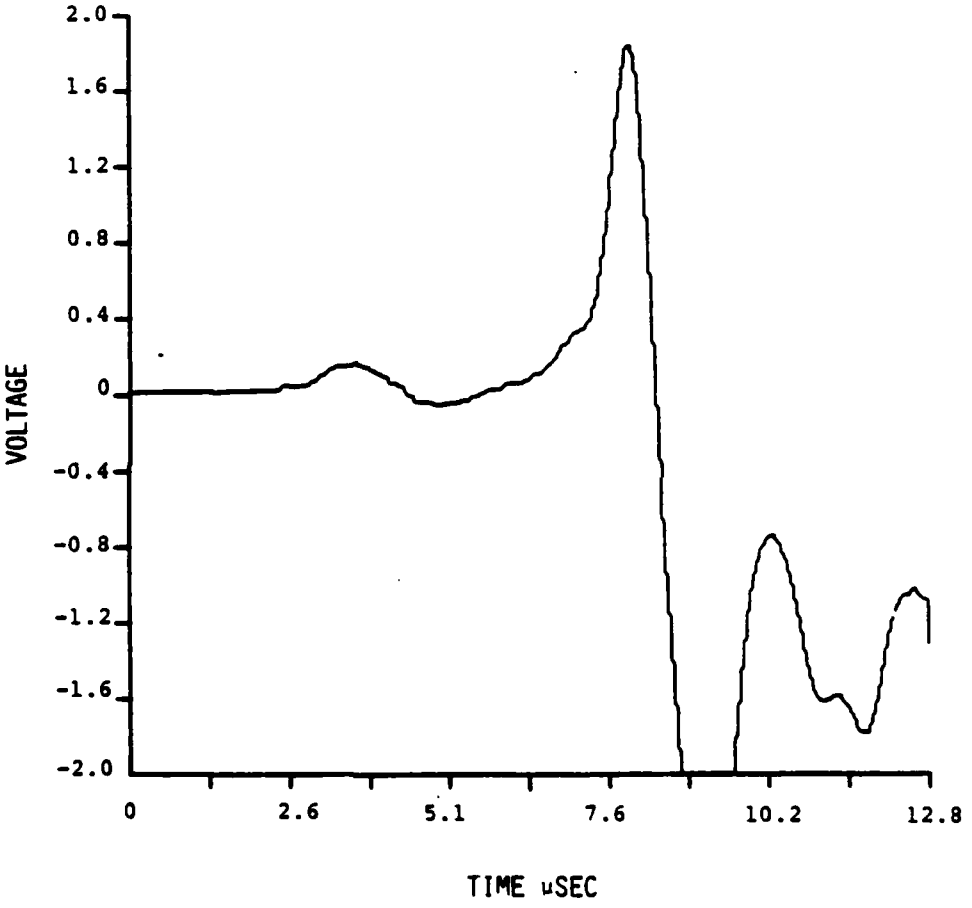

Fig. 6. Undistorted waveform of capillary fracture utilized as standard during specimen geometry investigation.

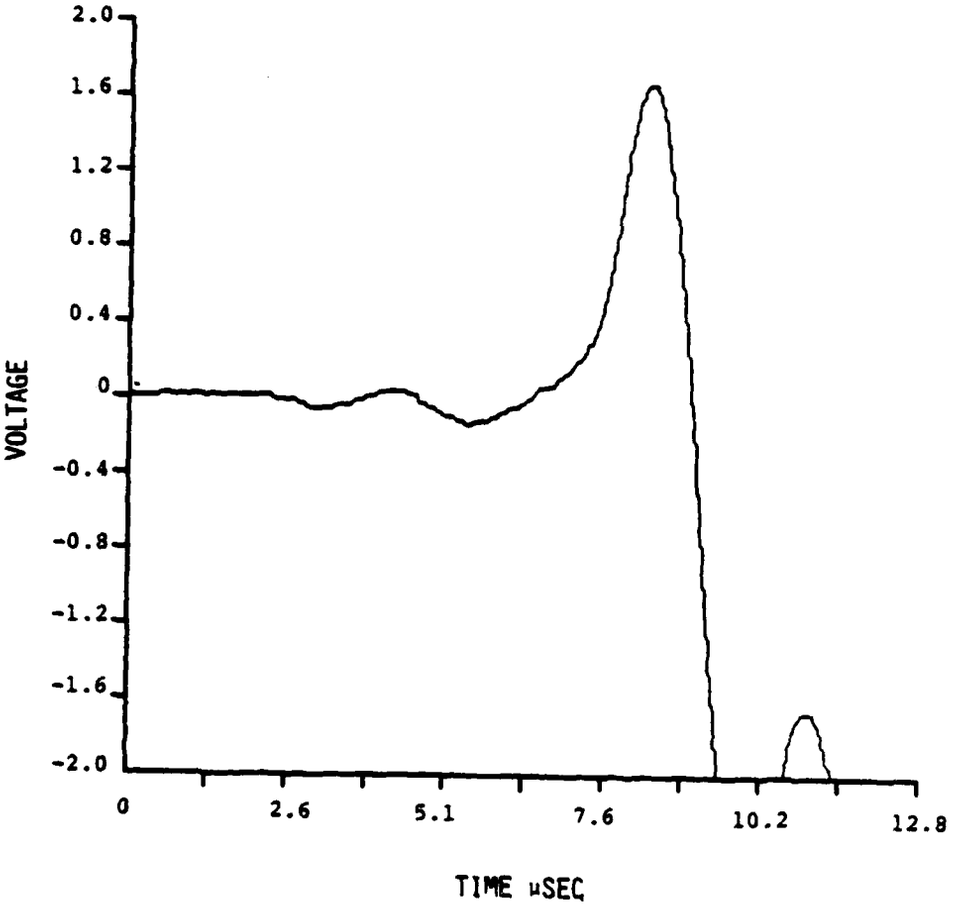

Fig.7. Waveform of glass capillary fracture through 0.075 x 0.075 in^2 cross-section.

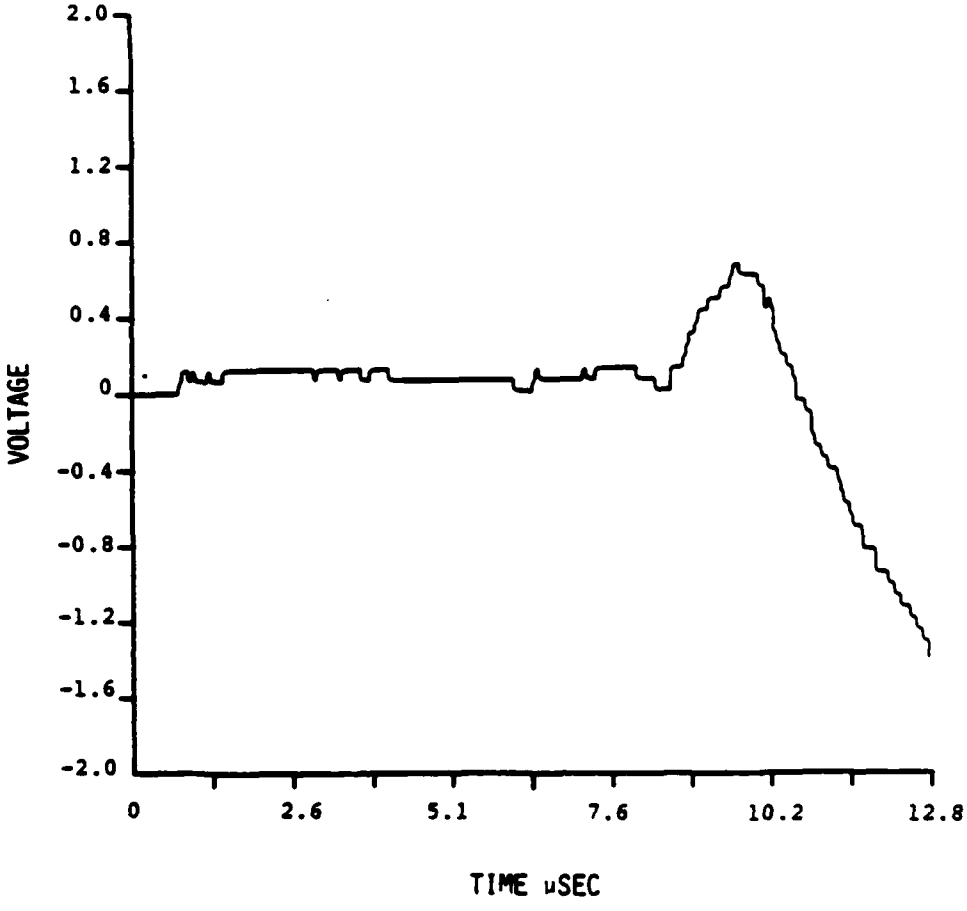

Fig.8. Waveform of glass capillary fracture through 0.123 x 0.123 in^2 cross-section.

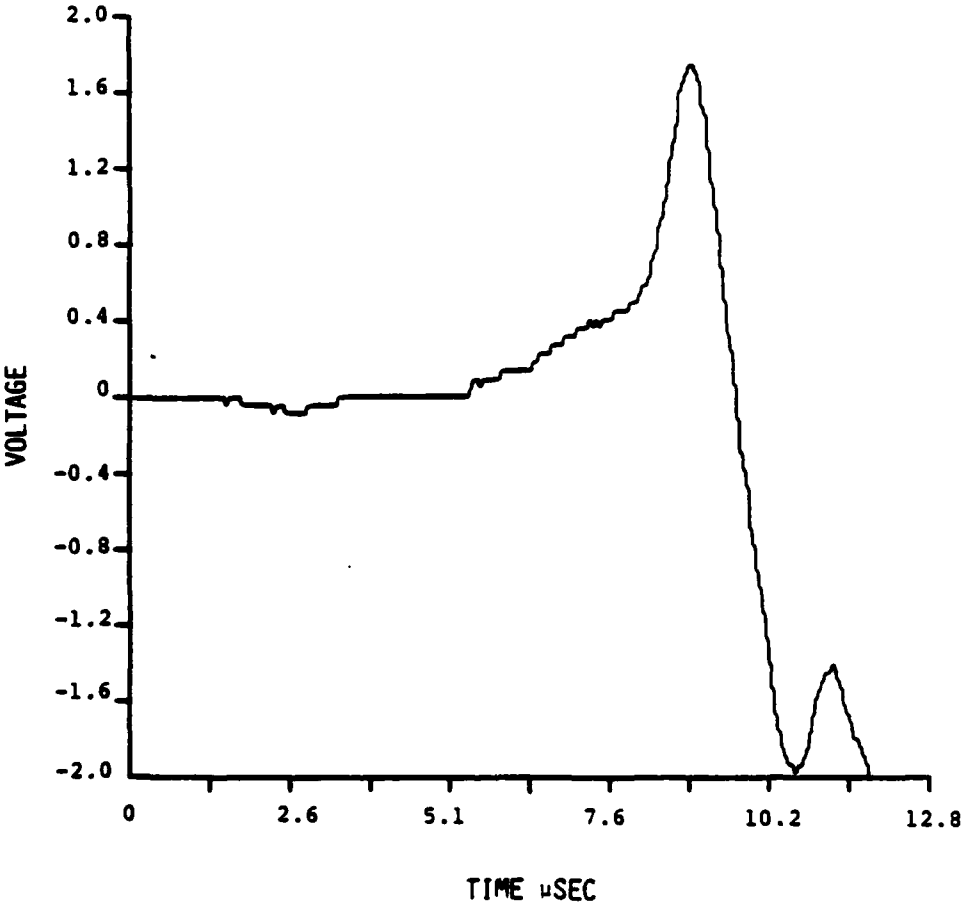

Fig. 9. Waveform of glass capillary fracture through 0.060 x 0.060 in^2 cross-section.

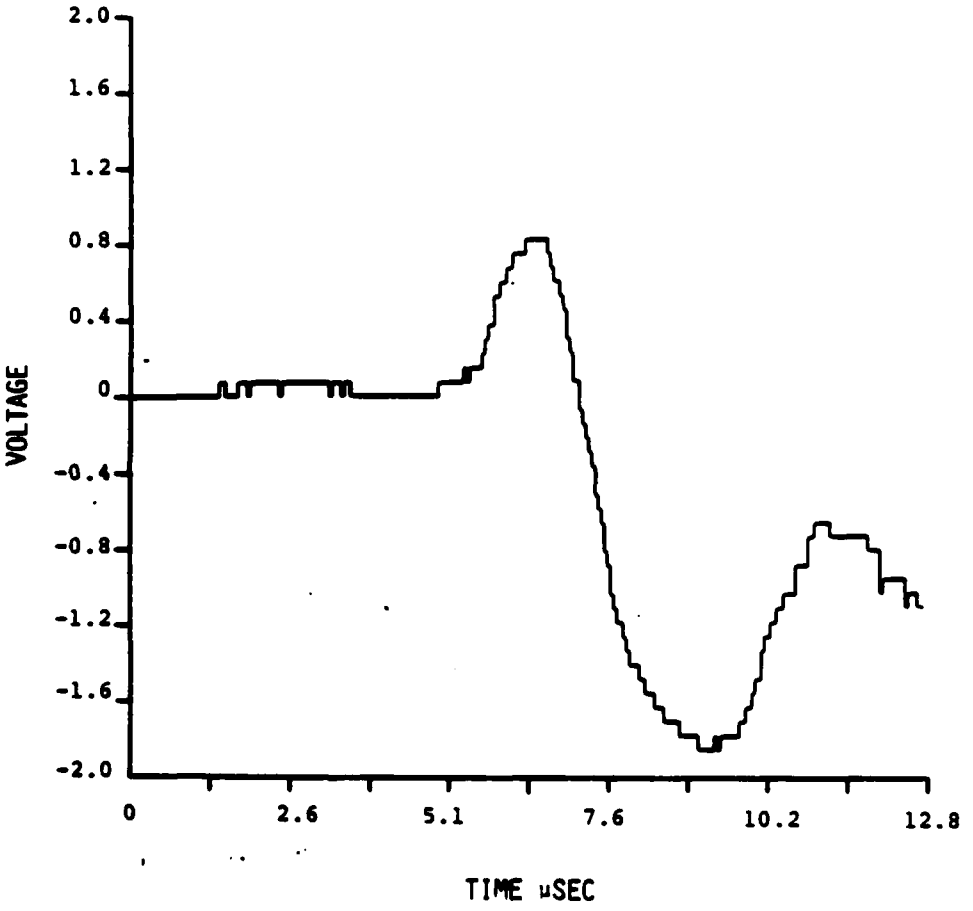

Fig.10. Waveform of glass capillary fracture through 0.025 x 0.075 in^2 cross-section.

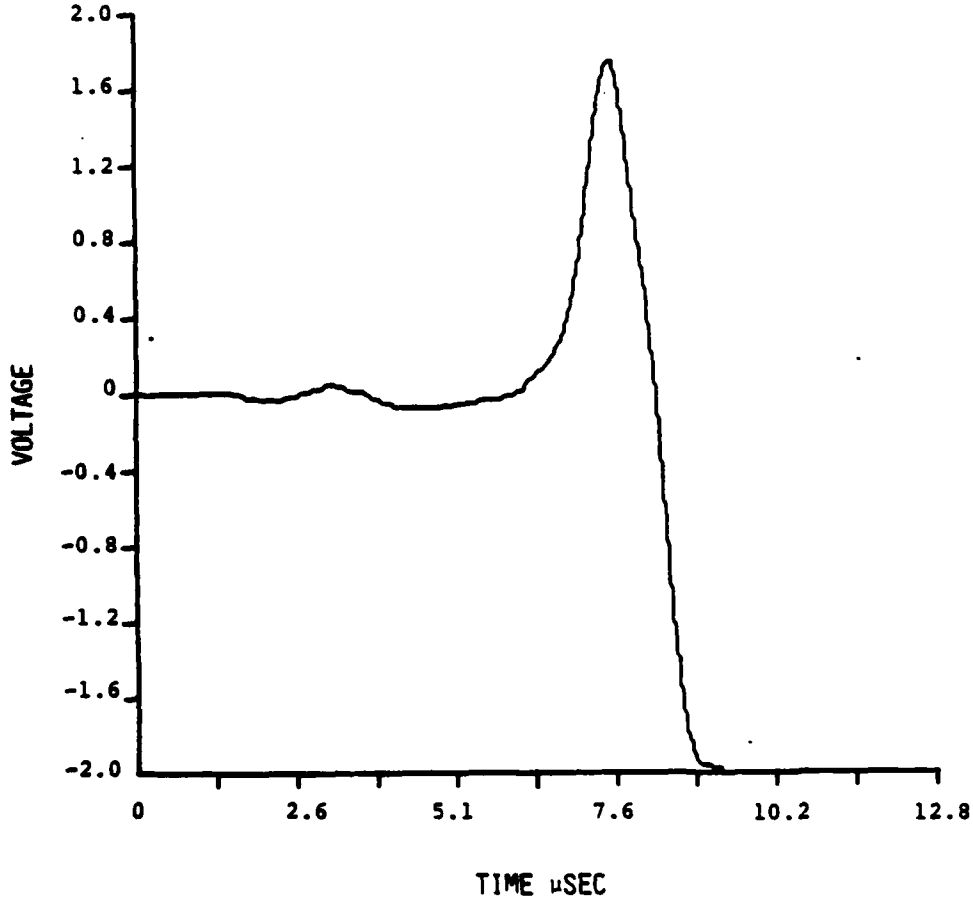

Fig.11. Waveform of glass capillary fracture through 0.075 x 0.03 in^2 cross-section.

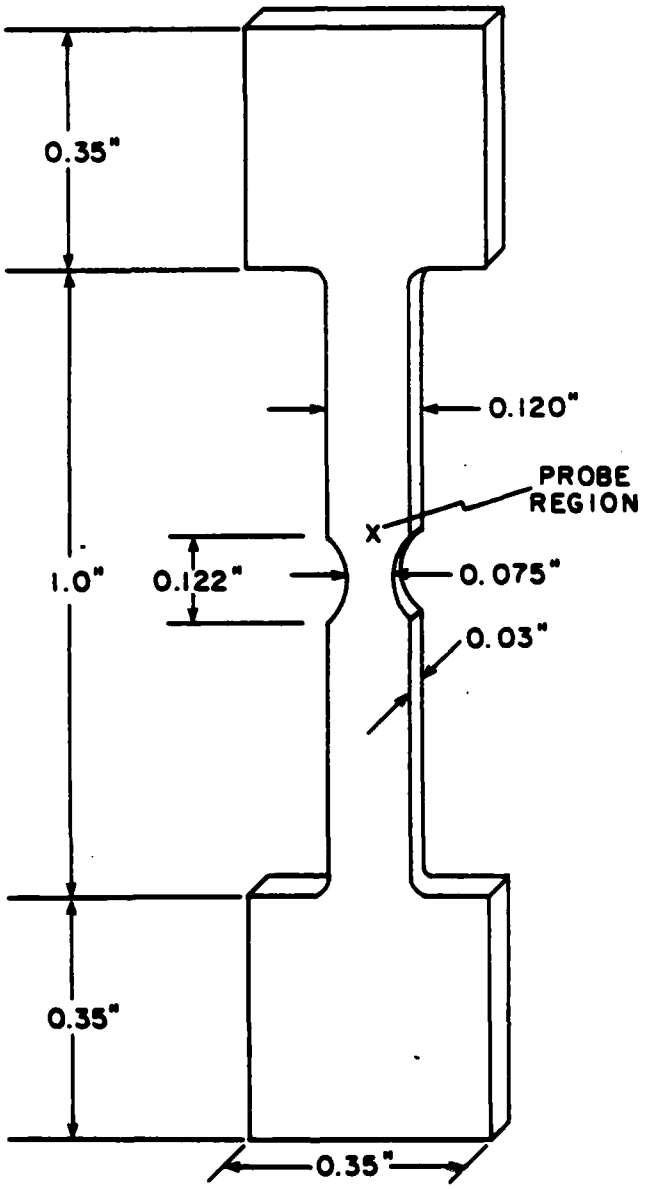

Fig. 12a. Schematic of micro-tensile specimen geometry.

Fig. 12b. Photograph of micro-tensile specimen.

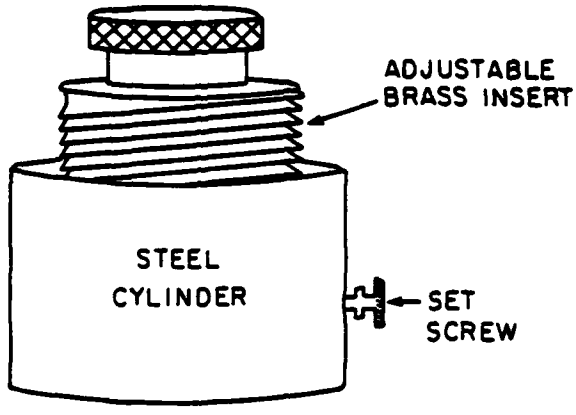

SIDE VIEW

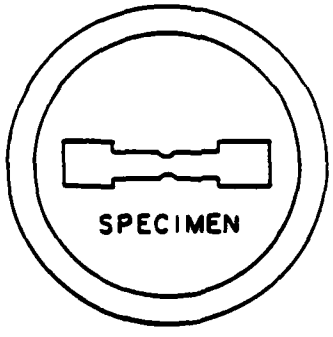

BOTTOM VIEW

1 INCH

Fig. 13a. Schematic of mounting fixture used to hold specimens during polishing.

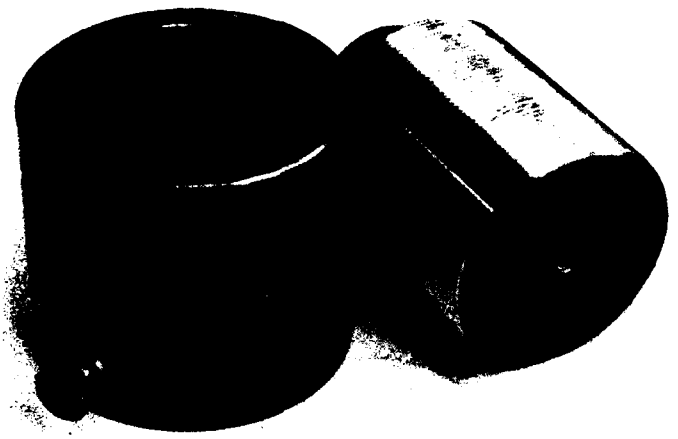

Fig. 13b. Photograph of mounting fixture used to hold specimens during polishing.

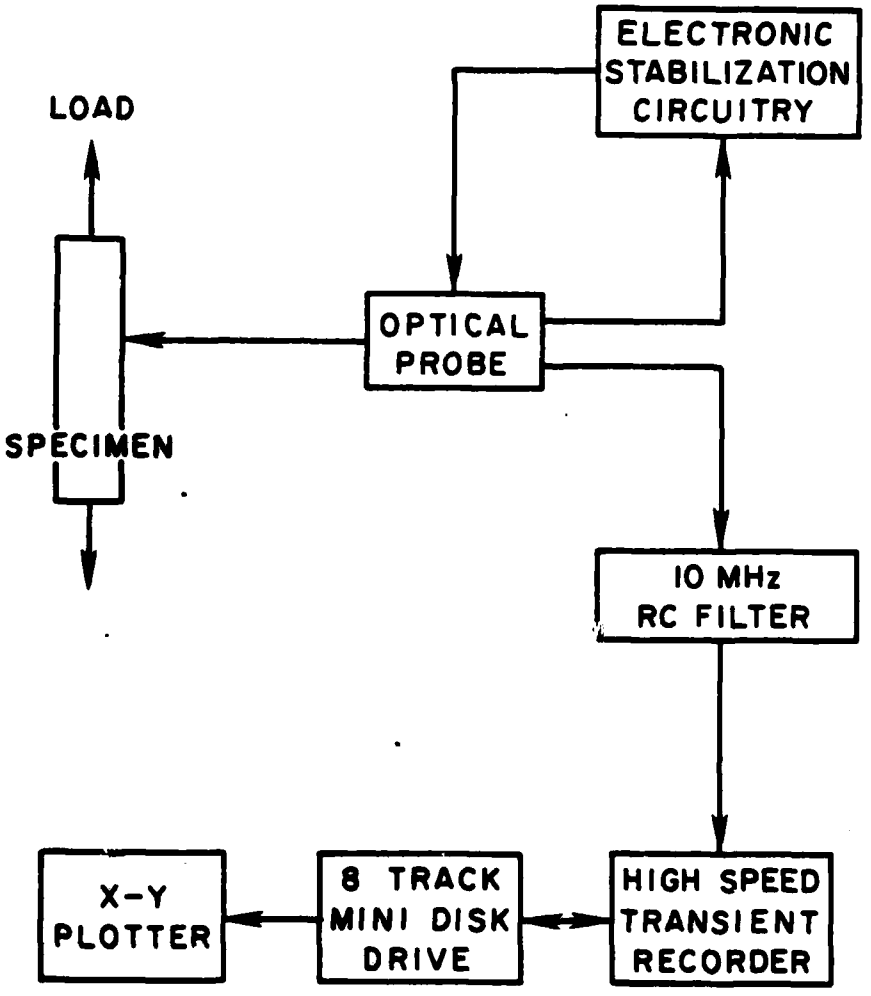

Fig. 14a. Block diagram of experimental system for micro-tensile tests.

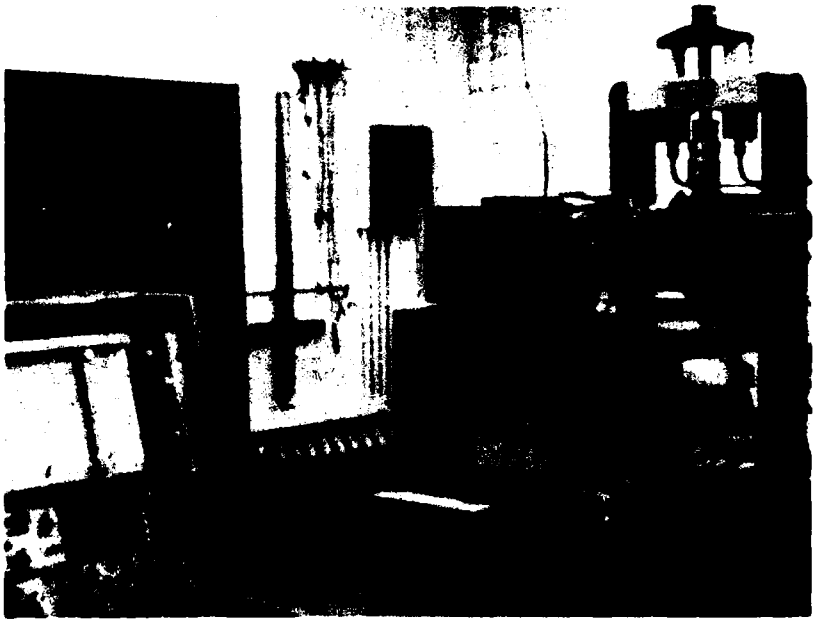

Fig. 14b. Photograph of experimental system for micro-tensile tests.

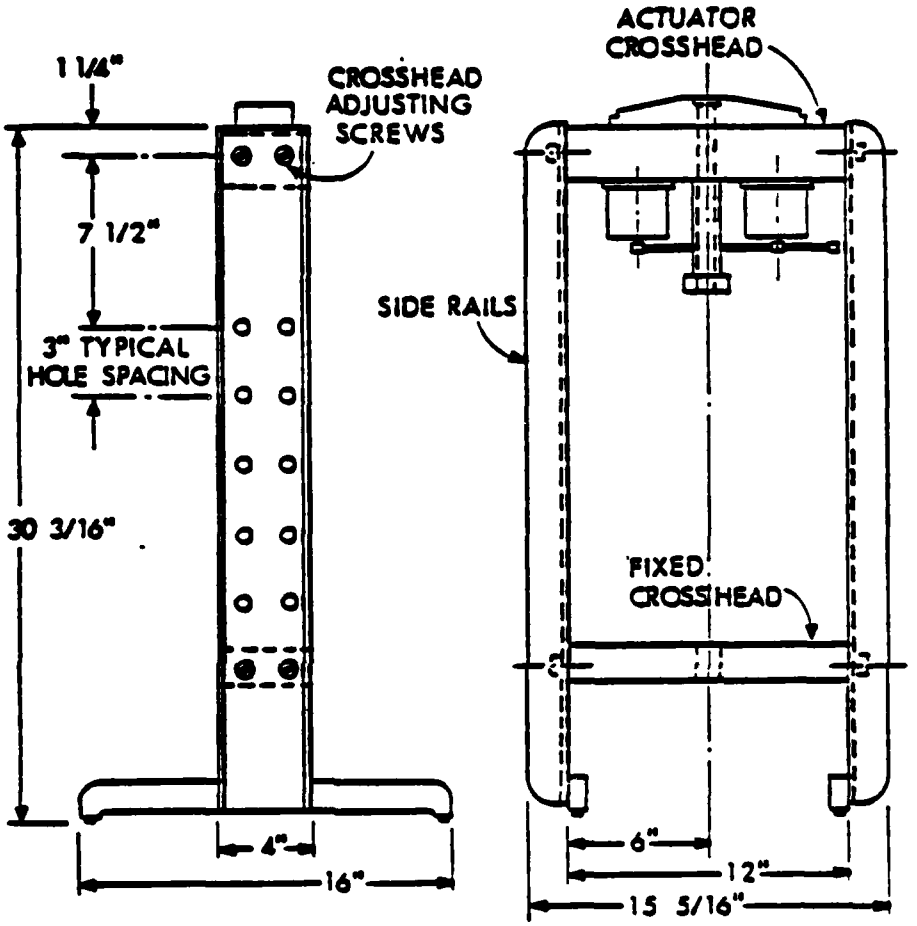

Fig. 15. Schematic of load frame for micro-tensile machine.

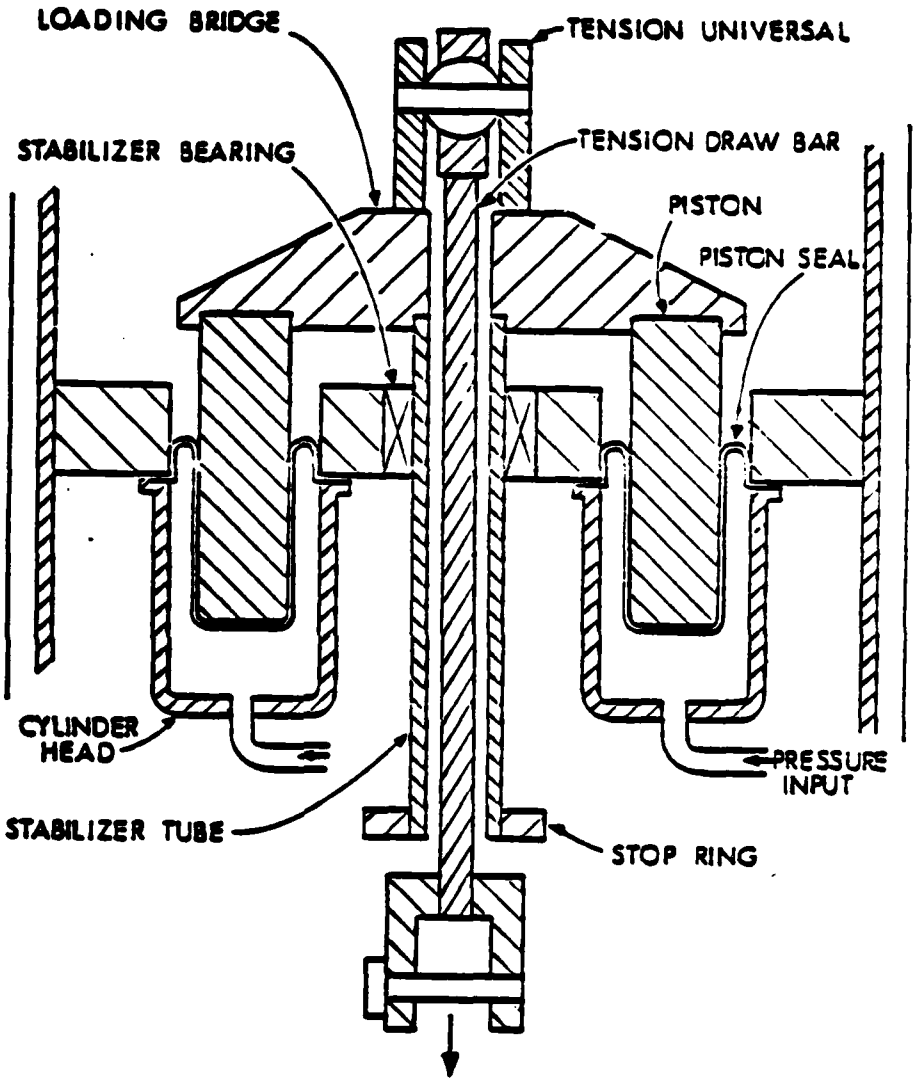

Fig. 16. Cross-sectional schematic of actuator crosshead in pneumatic tensile machine.

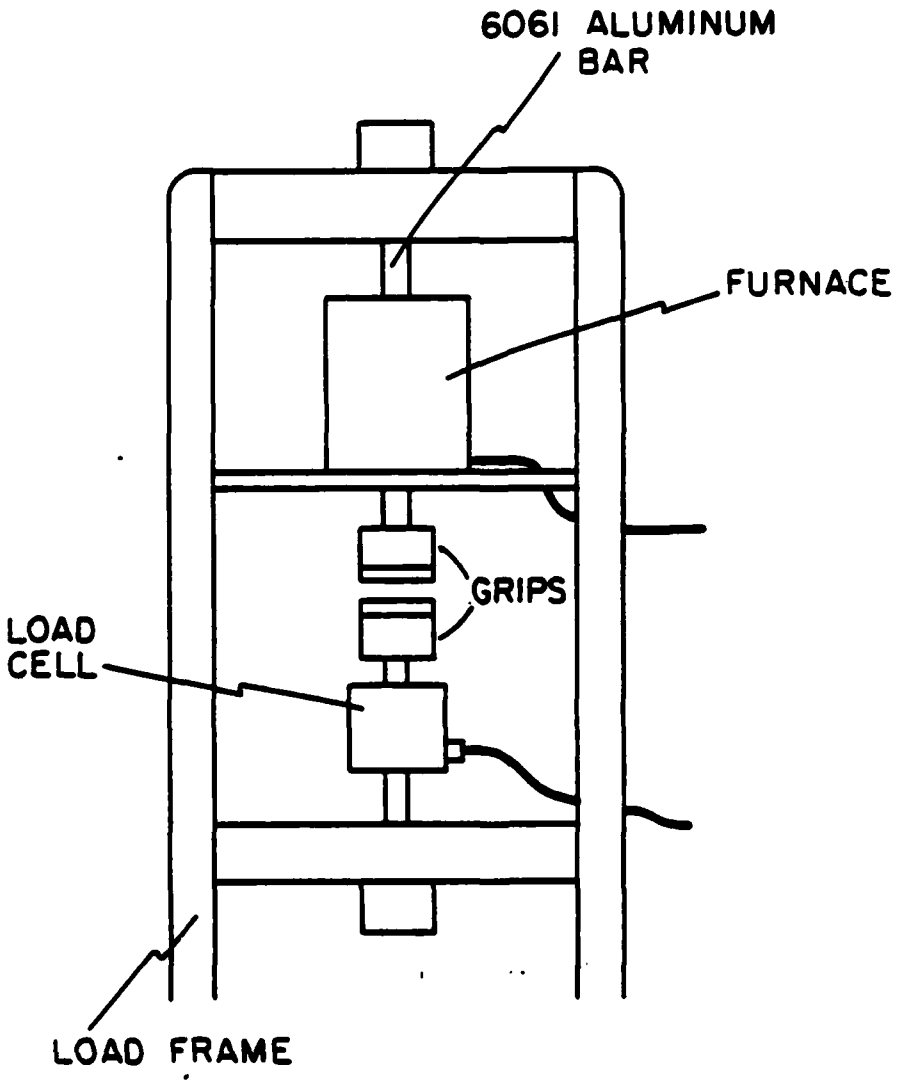

Fig. 17. Schematic of thermal tensile machine.

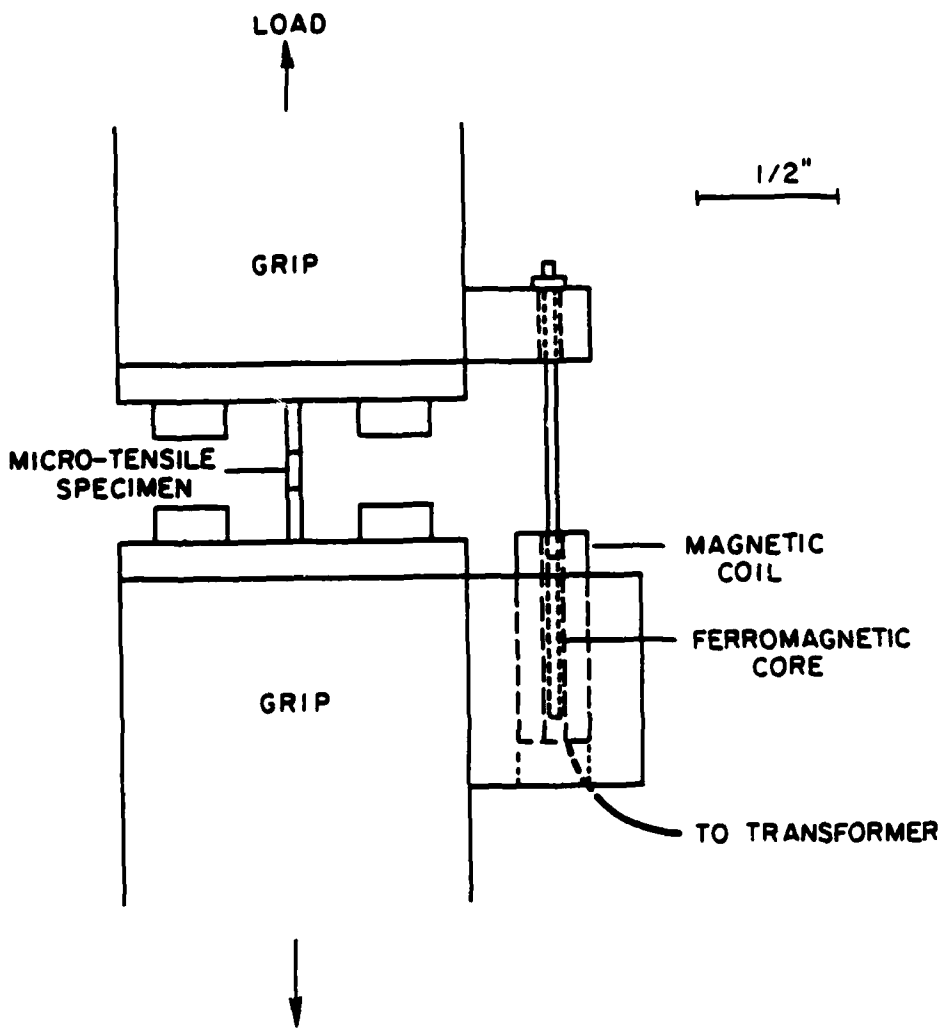

Fig. 18a. Schematic of LVDT used for measuring displacement during micro-tensile tests.

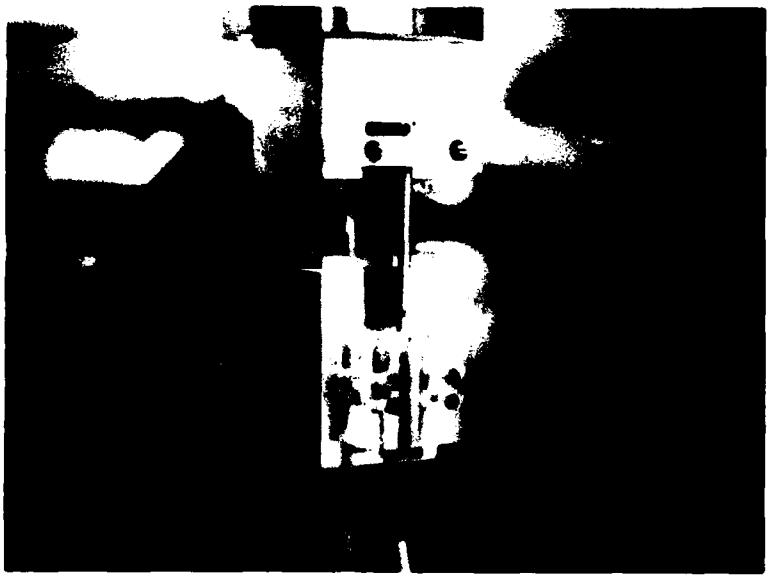

Fig. 18b. Photograph of LVDT used for measuring displacement during micro-tensile tests.

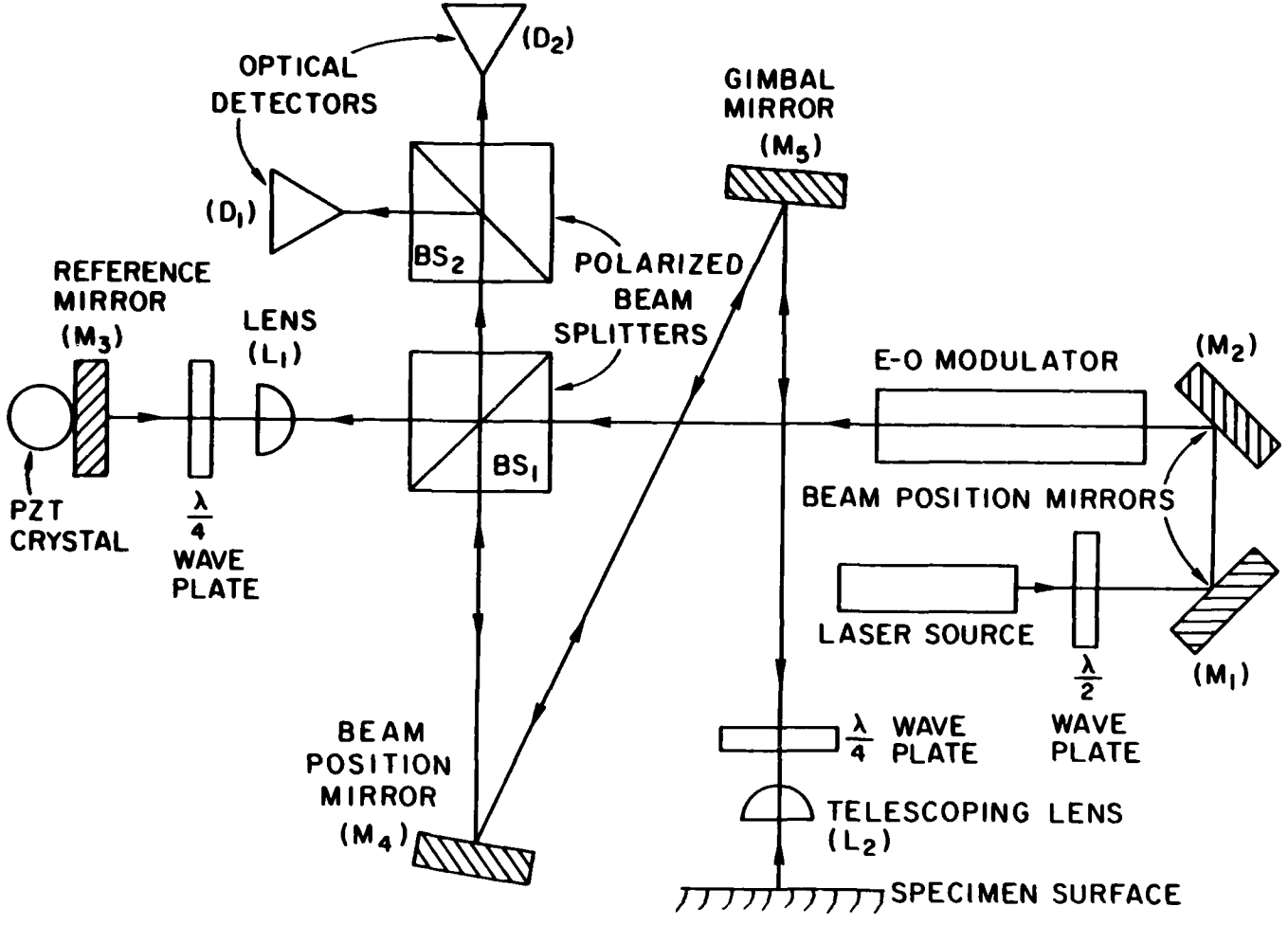

Fig. 19. Block diagram of optical arrangement of interferometer.

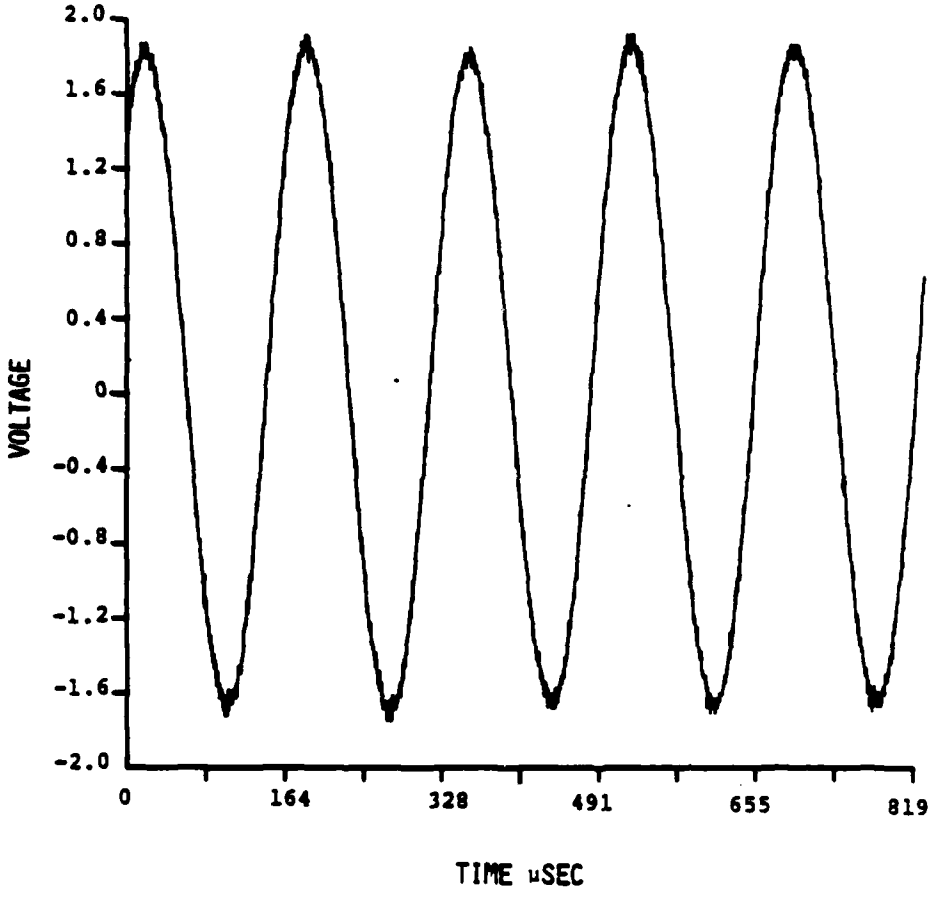

Fig. 20. Calibration waveform utilized in determination of Angstroms displacement per volt output from interferometer. Peak to peak voltage is equivalent to approximately 50 Å displacement.

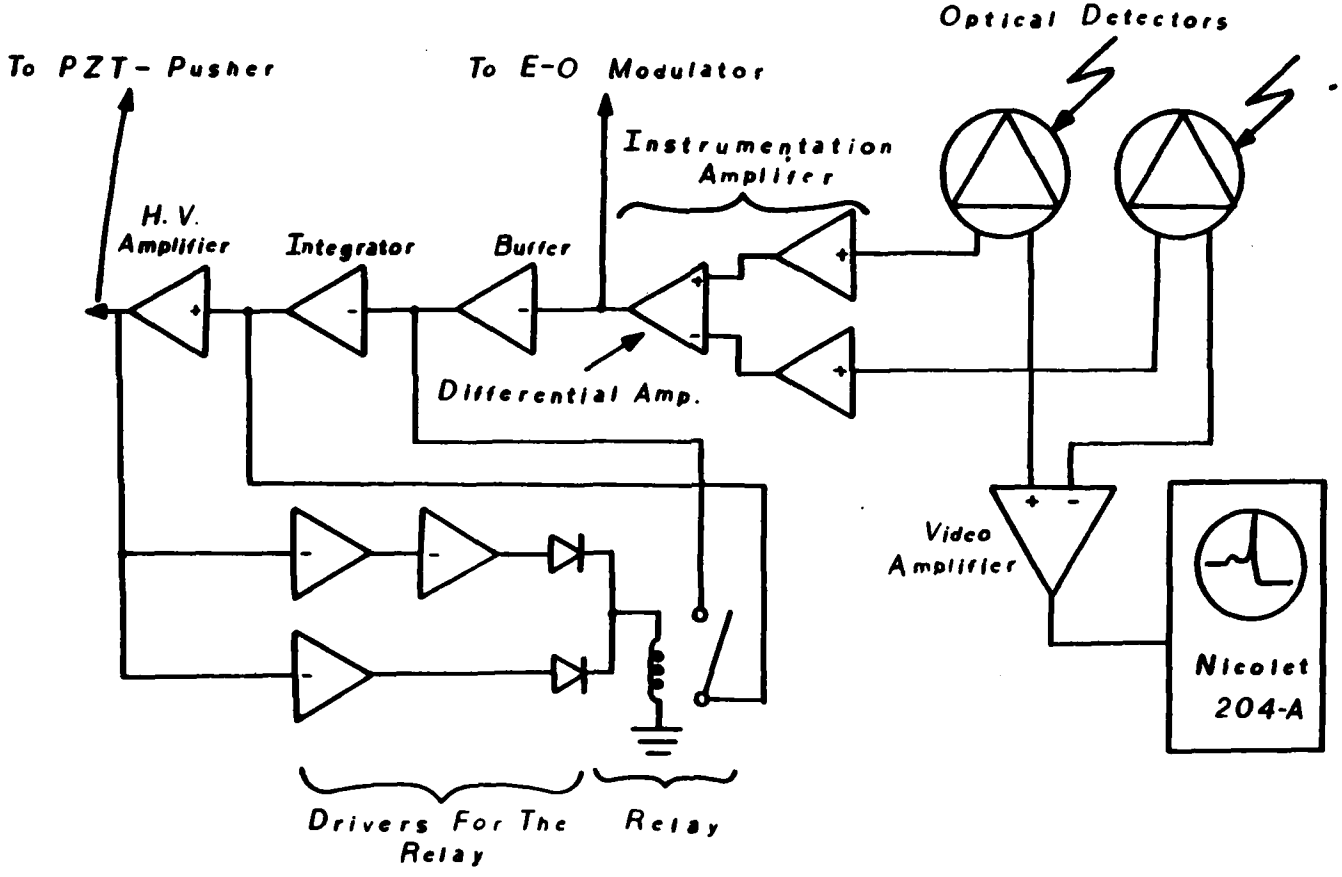

Fig. 21. Support circuitry for interferometer - path stabilization loop and high frequency output.

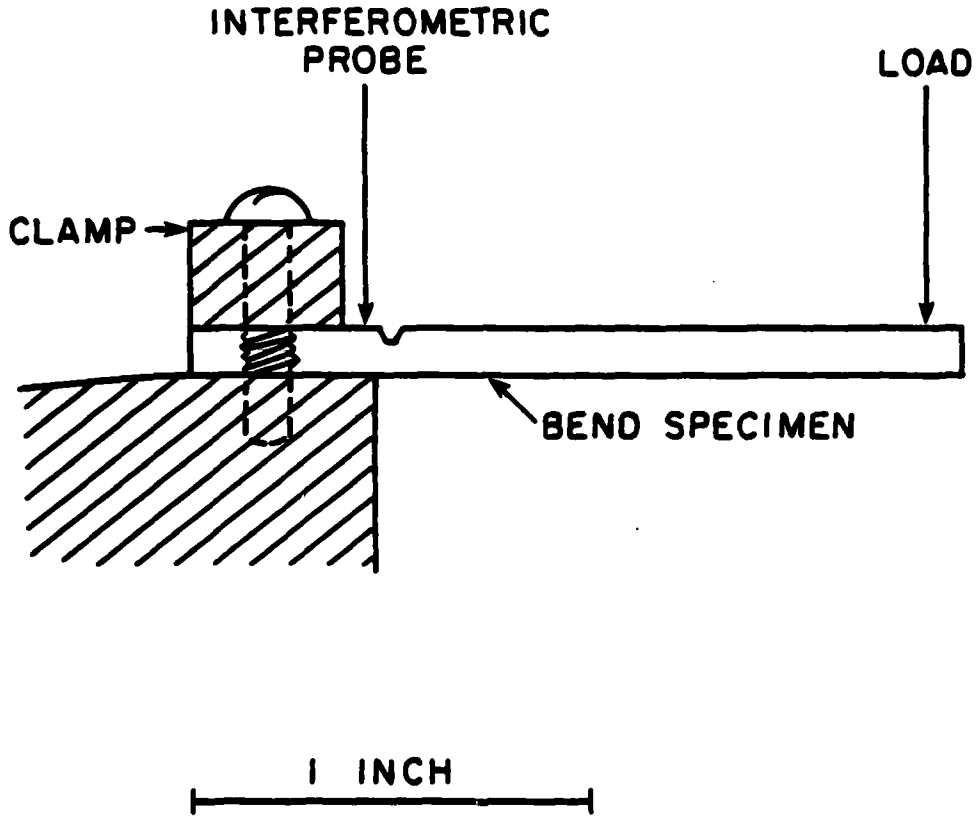

Fig. 22. Schematic of cantilever beam arrangement utilized in bend tests.

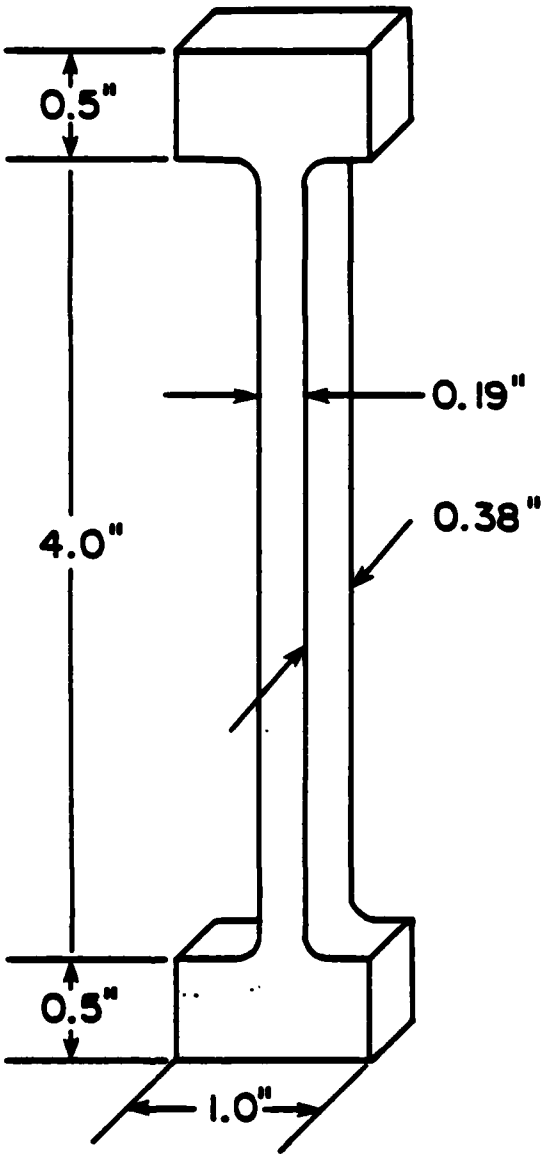

Fig. 23a. Schematic of macro-tensile specimen geometry.

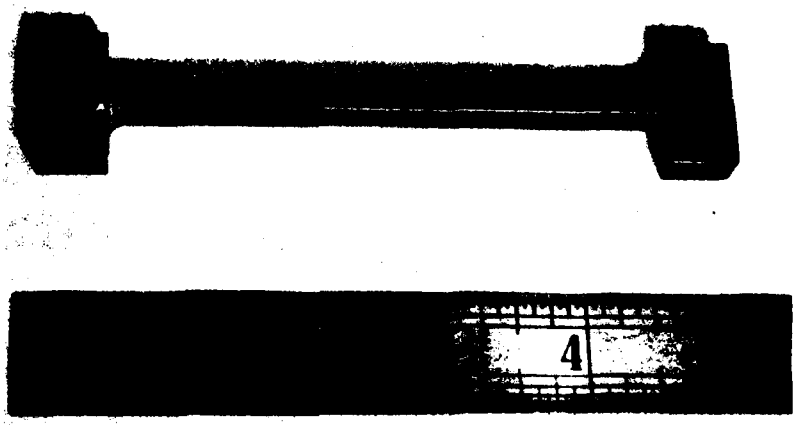

Fig. 23b. Photograph of macro-tensile specimen.

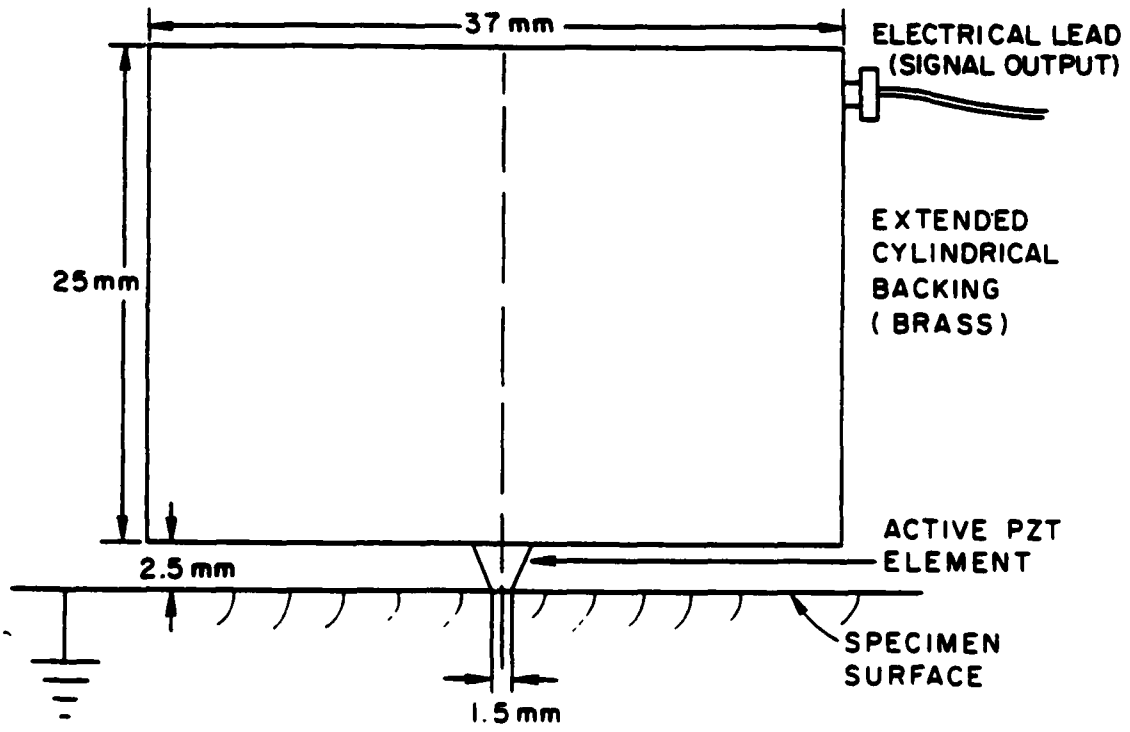

Fig. 24a. Schematic of new transducer designed by Proctor at NBS.

Fig. 24b. Photograph of new transducer designed by Procter at NBS.

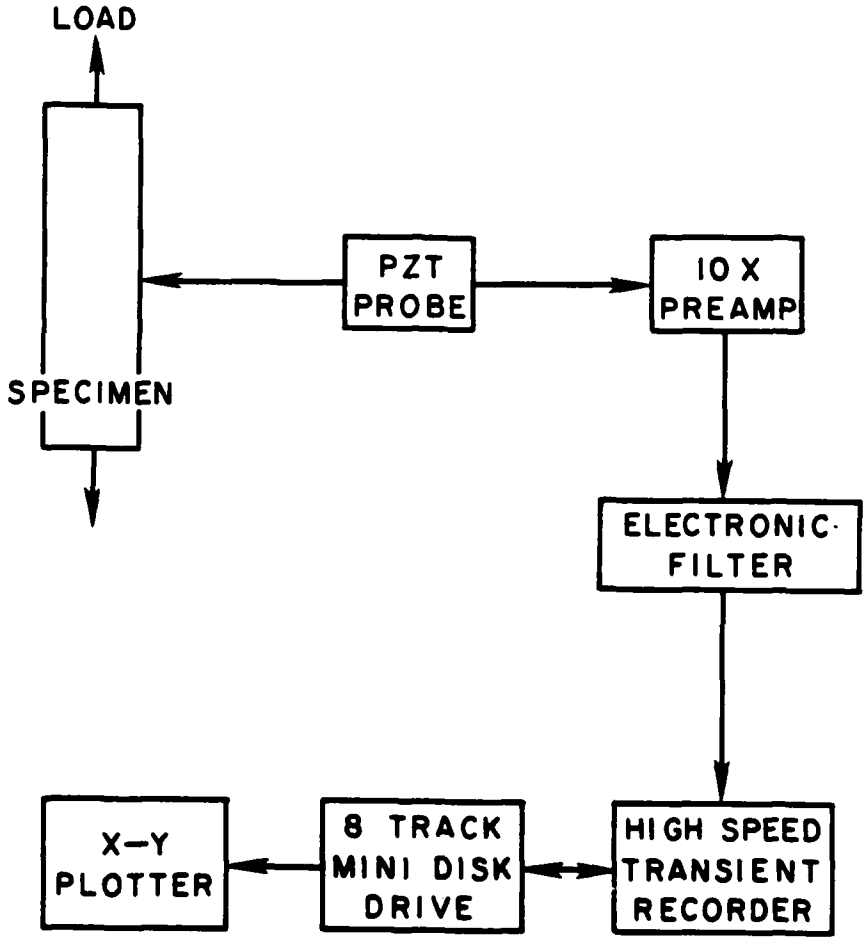

Fig. 25a. Block diagram of experimental system for macro-tensile tests.

Fig. 25b. Photograph of experimental system for macro-tensile tests.

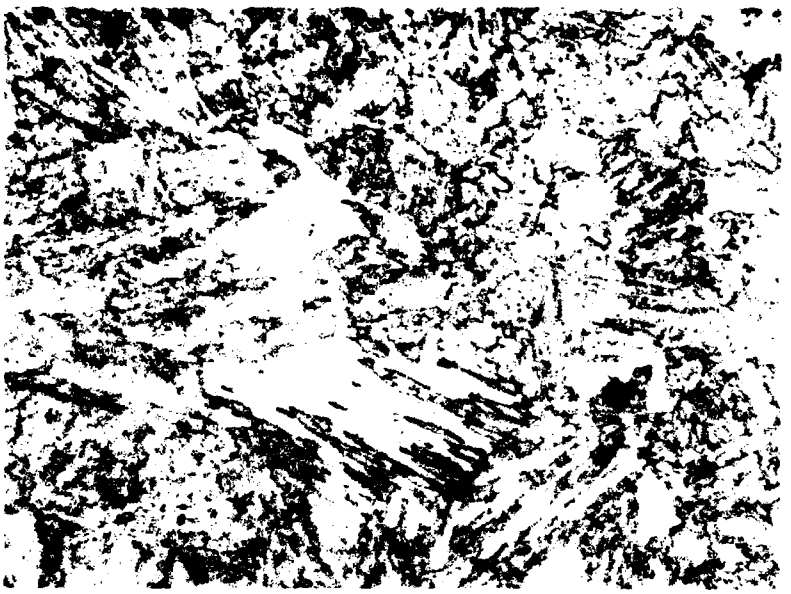

Fig. 26a. Microstructure of HY 80.
Nitol etch, ~650X.

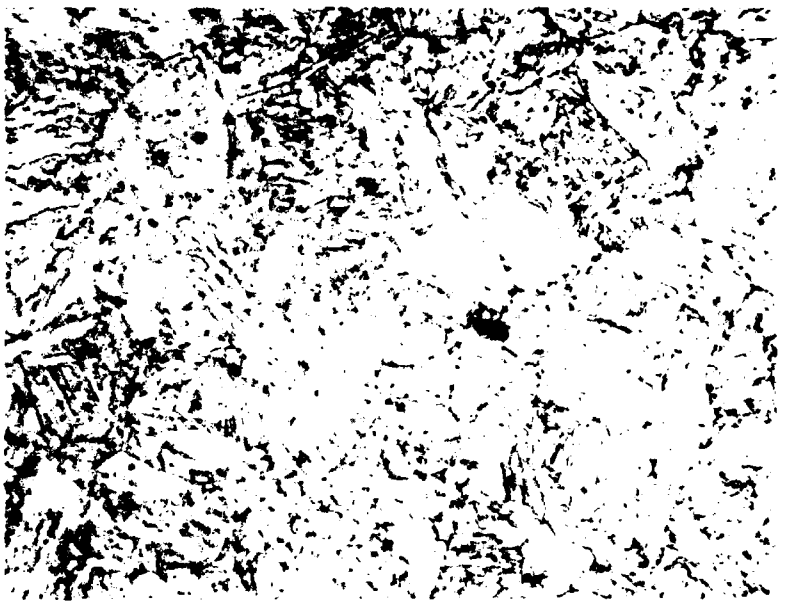

Fig. 26b. Microstructure of HY 100.
Nitol etch, ~650X.

Fig. 26c. Microstructure of HY 130.
Nitol etch, ~650X.

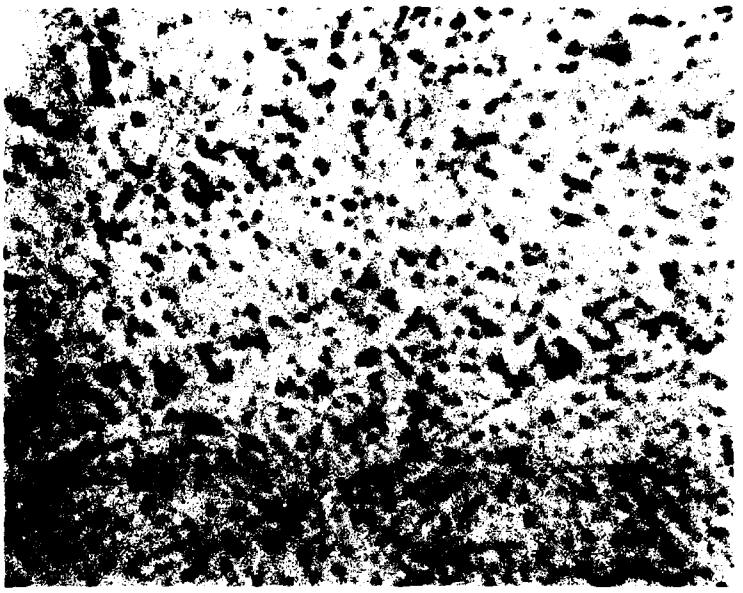

Fig. 27a. Microstructure of HY 80.
Picral etch, ~2640X.

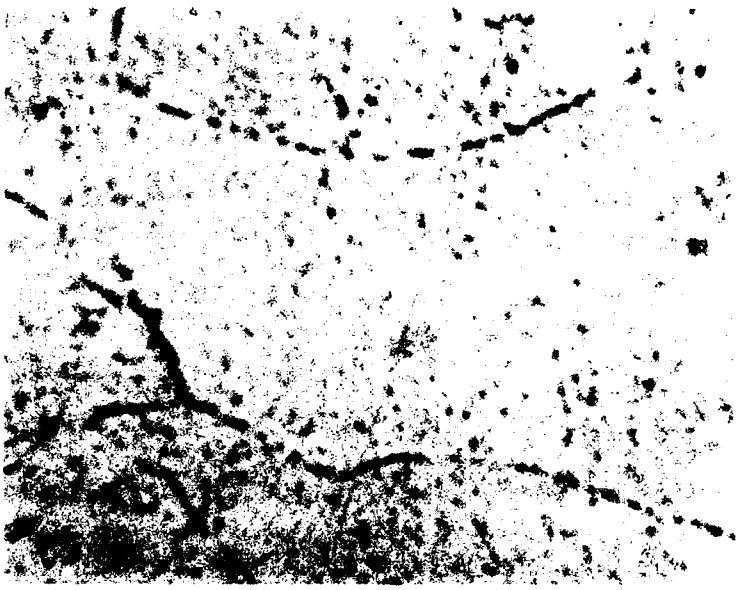

Fig. 27b. Microstructure of HY 100.
Picral etch,~2640X.

Fig. 27c. Microstructure of HY 130.
Picral etch, ~2640X.

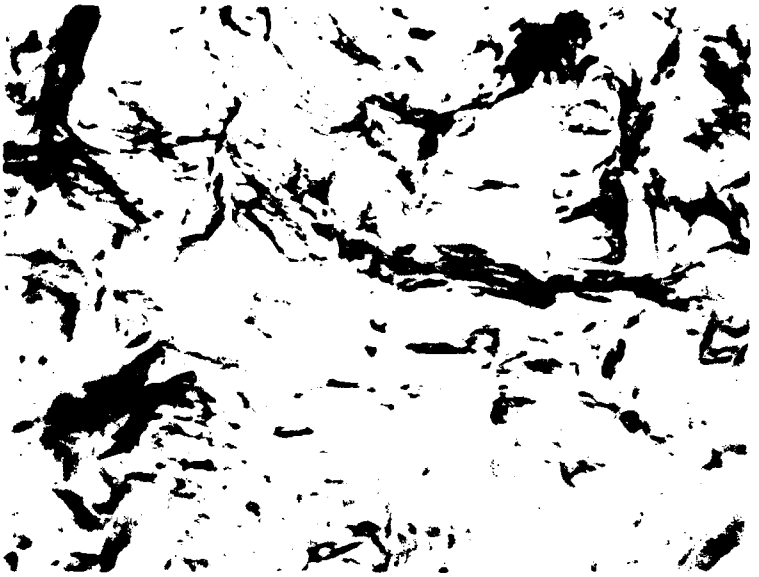

Fig. 28. Slip and phase boundary motion seen on a surface that was polished prior to deformation. Unetched, ~450X.

Fig. 29. Sectioned specimen viewed near fracture surface illustrating void mechanism of fracture. Unetched, ~340X.

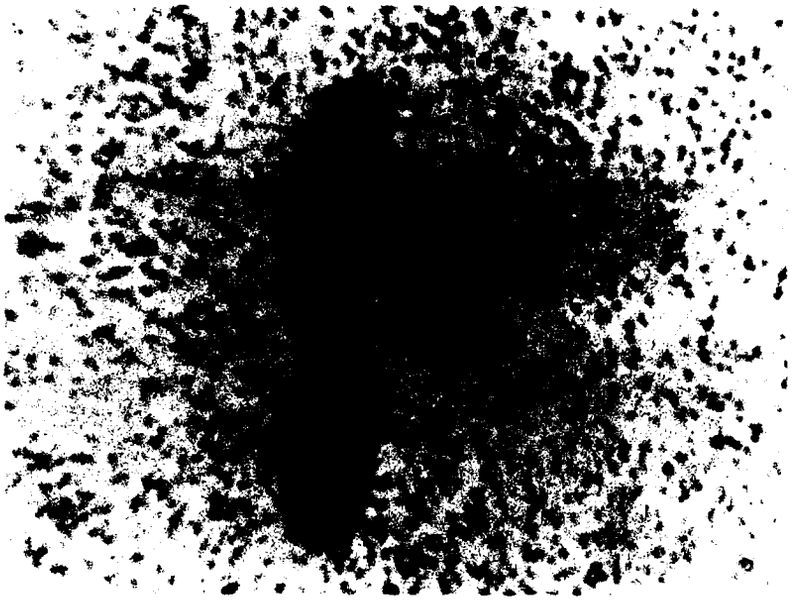

Fig. 30. Void initiation at particle matrix interface. Picral etch, ~2640X.

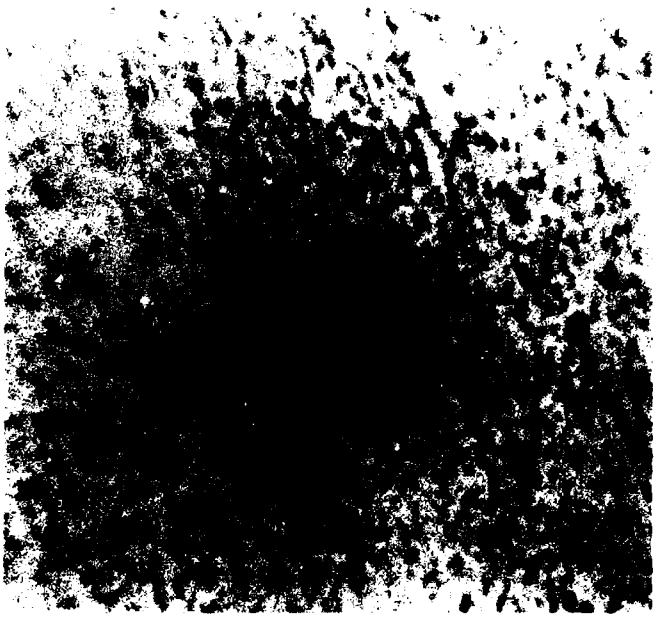

Fig. 31. Void initiation between two sections of fractured particle. Picral etch, ~2460X.

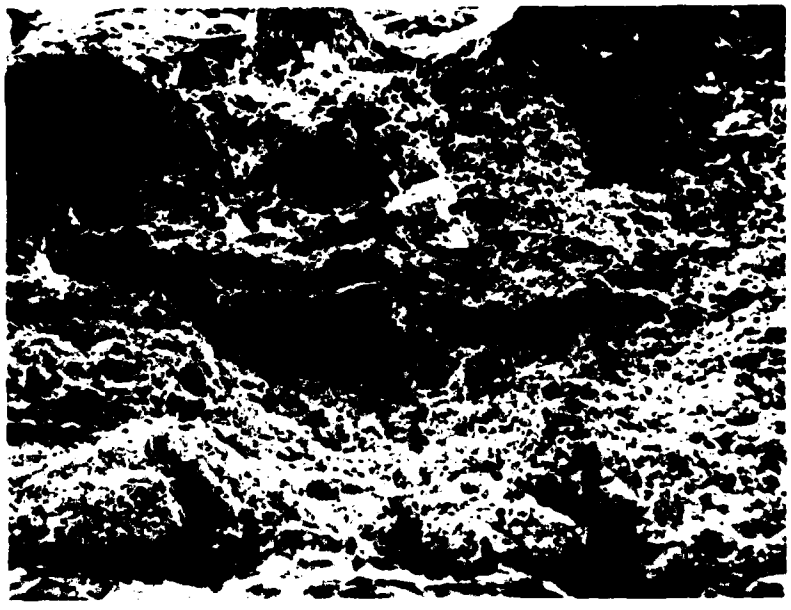

Fig. 32a. Typical fracture surface, ~100X.

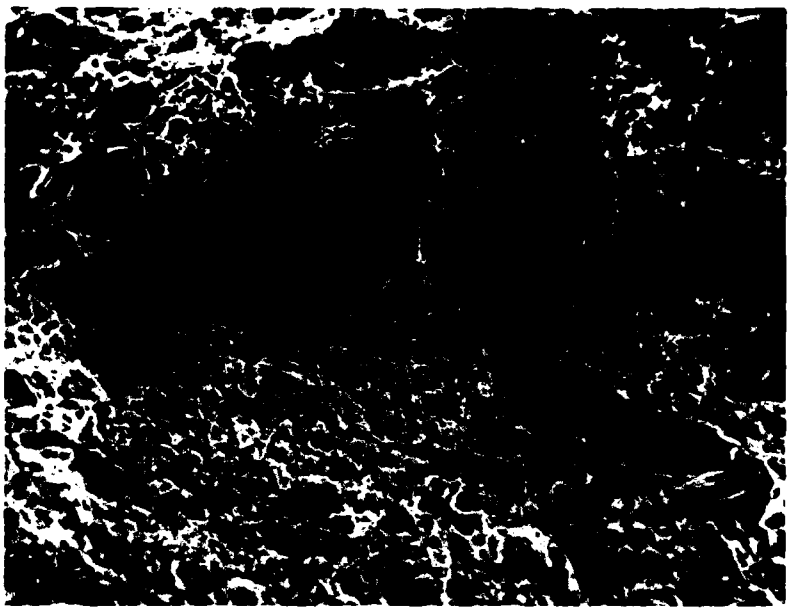

Fig. 32b. Typical fracture surface, ~250X.

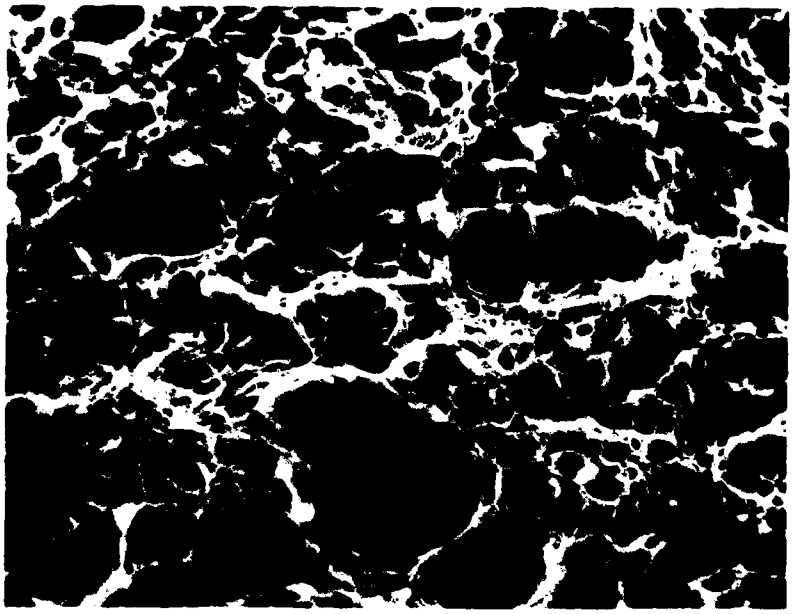

Fig. 32c. Typical fracture surface, ~1500X.

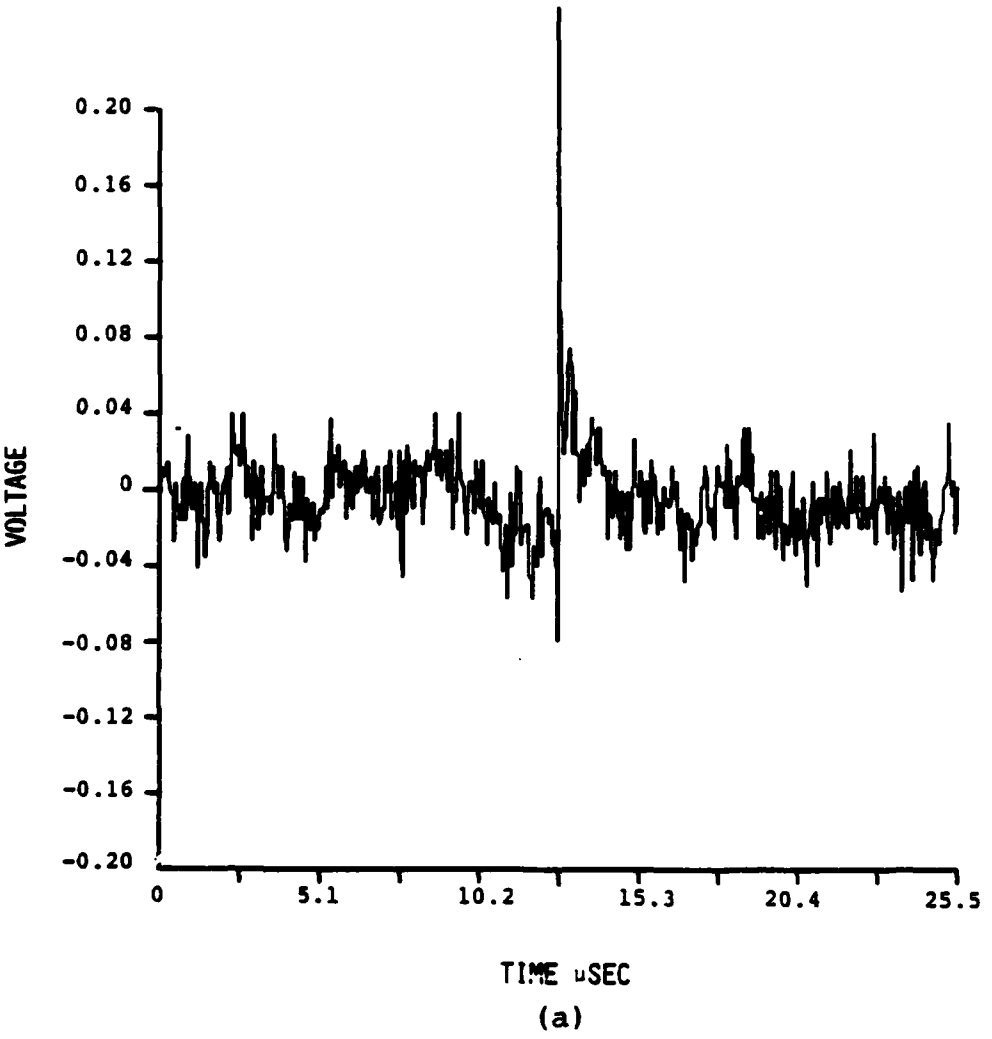

(a)

Fig. 33. Waveforms from micro-tensile tests.

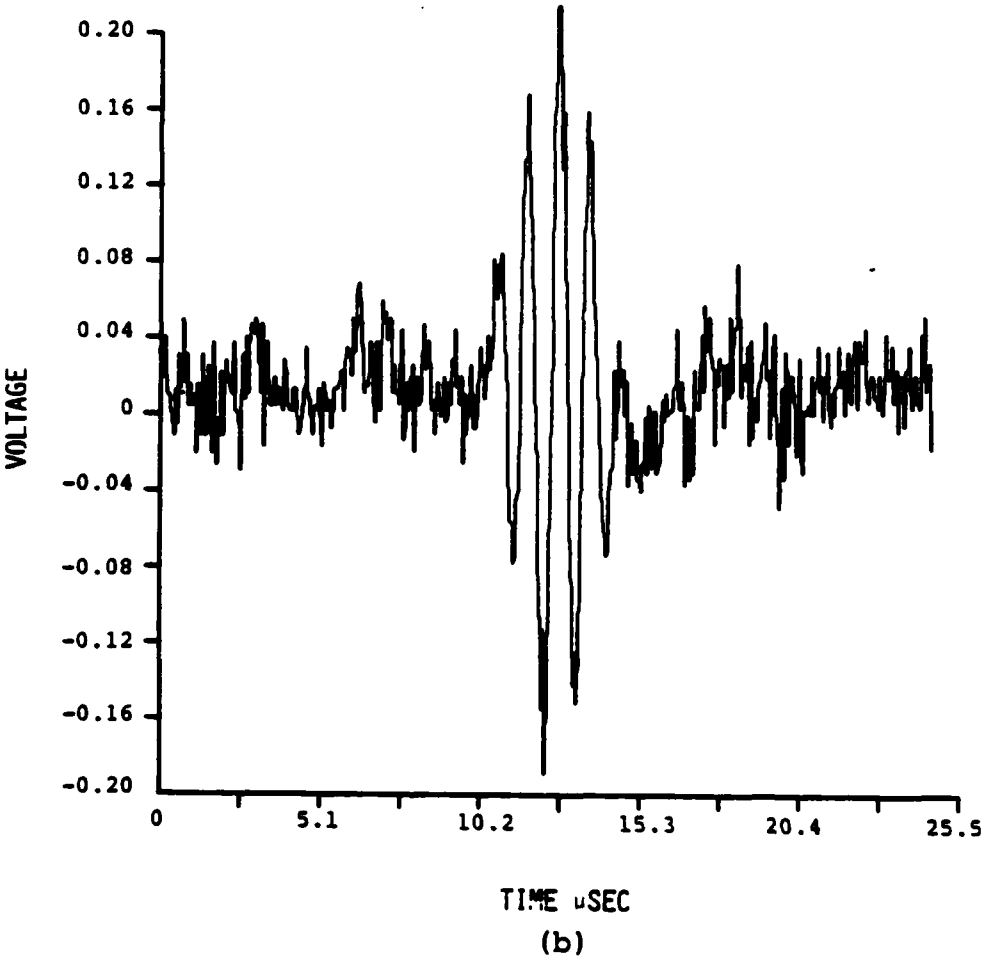
0.20
0.16
0.12
0.08
0.04
0
-0.04
-0.08
-0.12
-0.16
-0.20
VOLTAGE
0
5.1
10.2
15.3
20.4
25.5
TIME uSEC

(b)

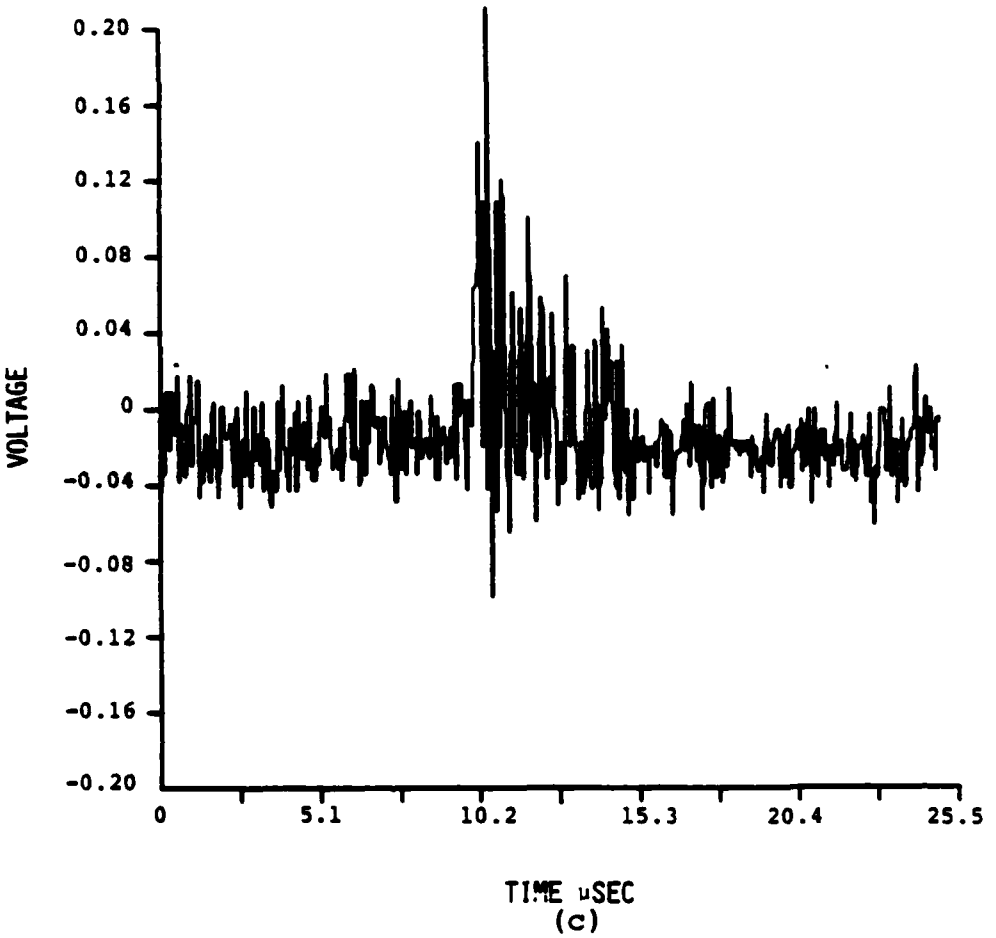
0.20
0.16
0.12
0.08
0.04
0
-0.04
-0.08
-0.12
-0.16
-0.20
VOLTAGE
0
5.1
10.2
15.3
20.4
25.5
TIME μSEC
(c)

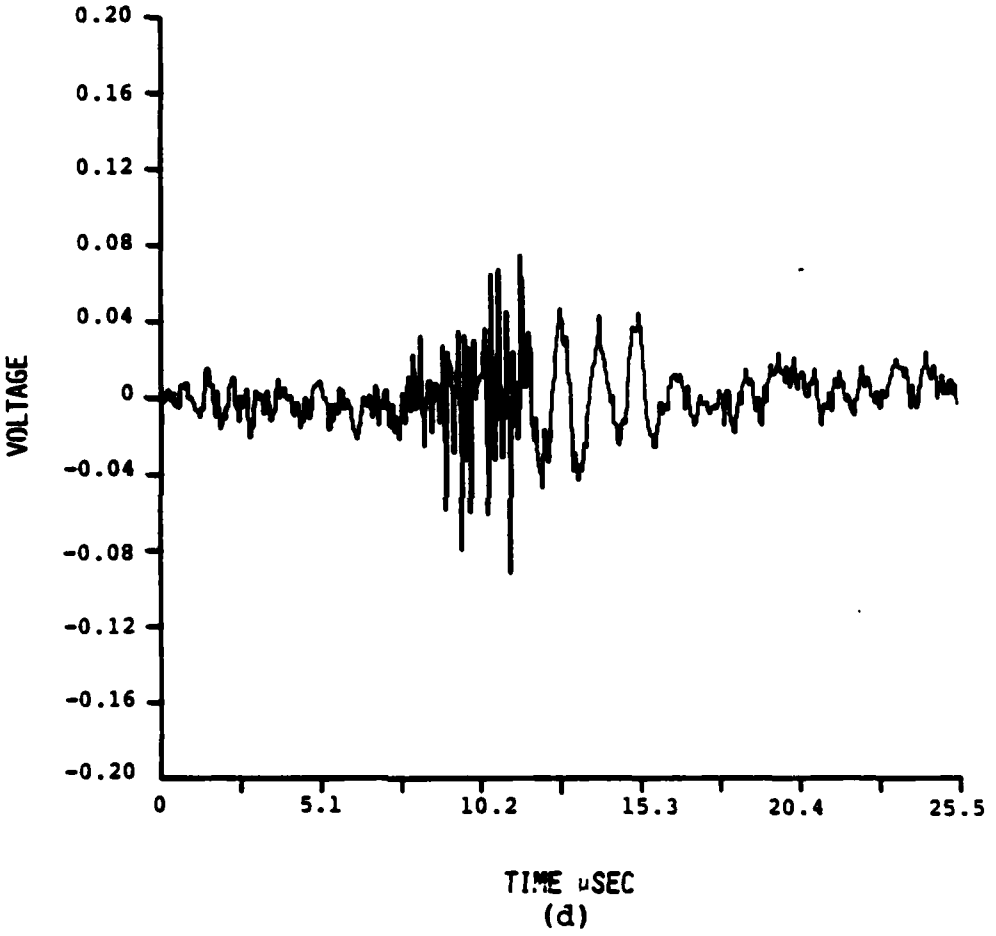
0.20
0.16
0.12
0.08
0.04
0
-0.04
-0.08
-0.12
-0.16
-0.20
VOLTAGE
0
5.1
10.2
15.3
20.4
25.5
TIME uSEC

(d)

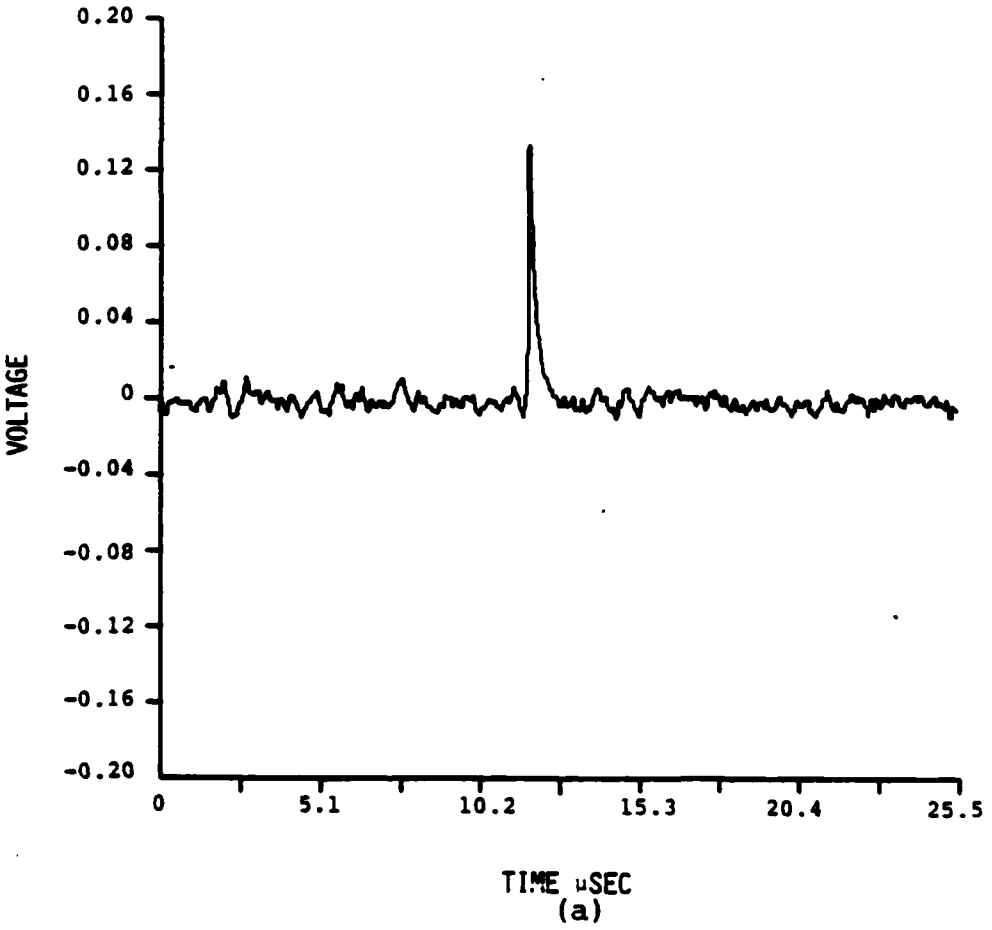

Fig. 34. "Spike" type waveforms from micro-tensile tests.

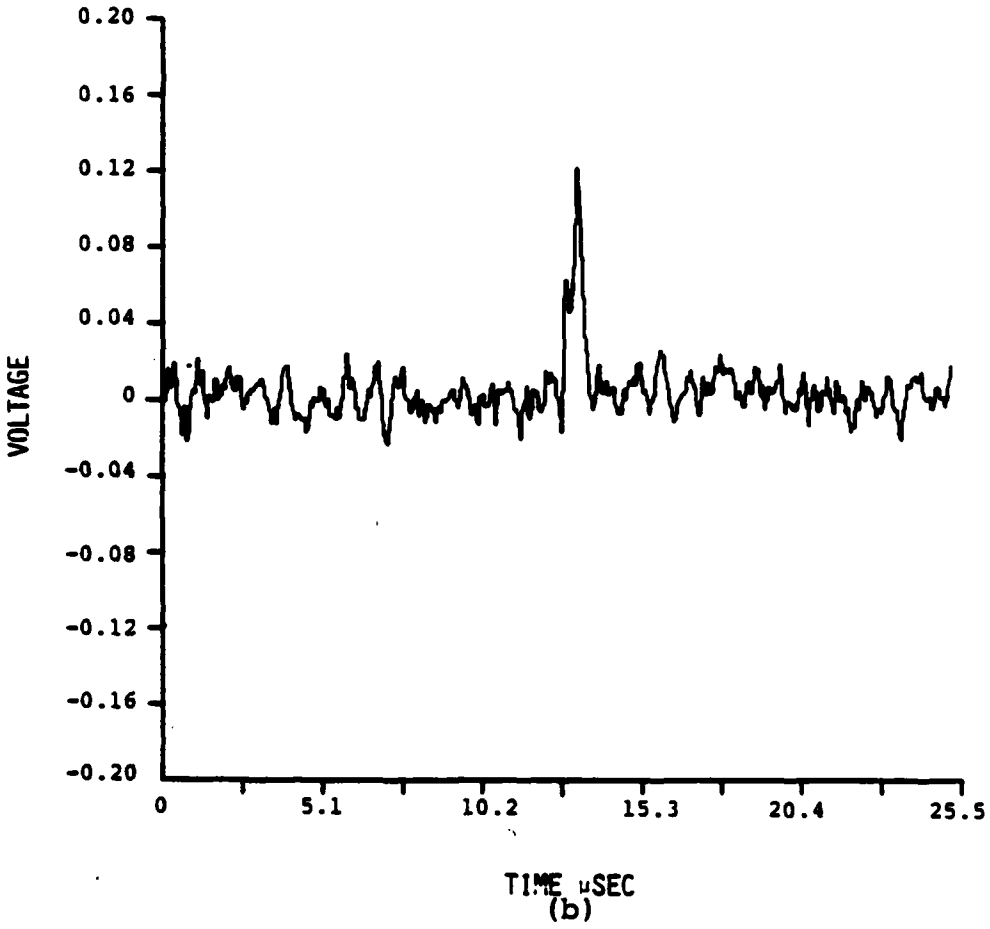
0.20
0.16
0.12
0.08
0.04
0
-0.04
-0.08
-0.12
-0.16
-0.20
VOLTAGE
0
5.1
10.2
15.3
20.4
25.5
TIME μSEC

(b)

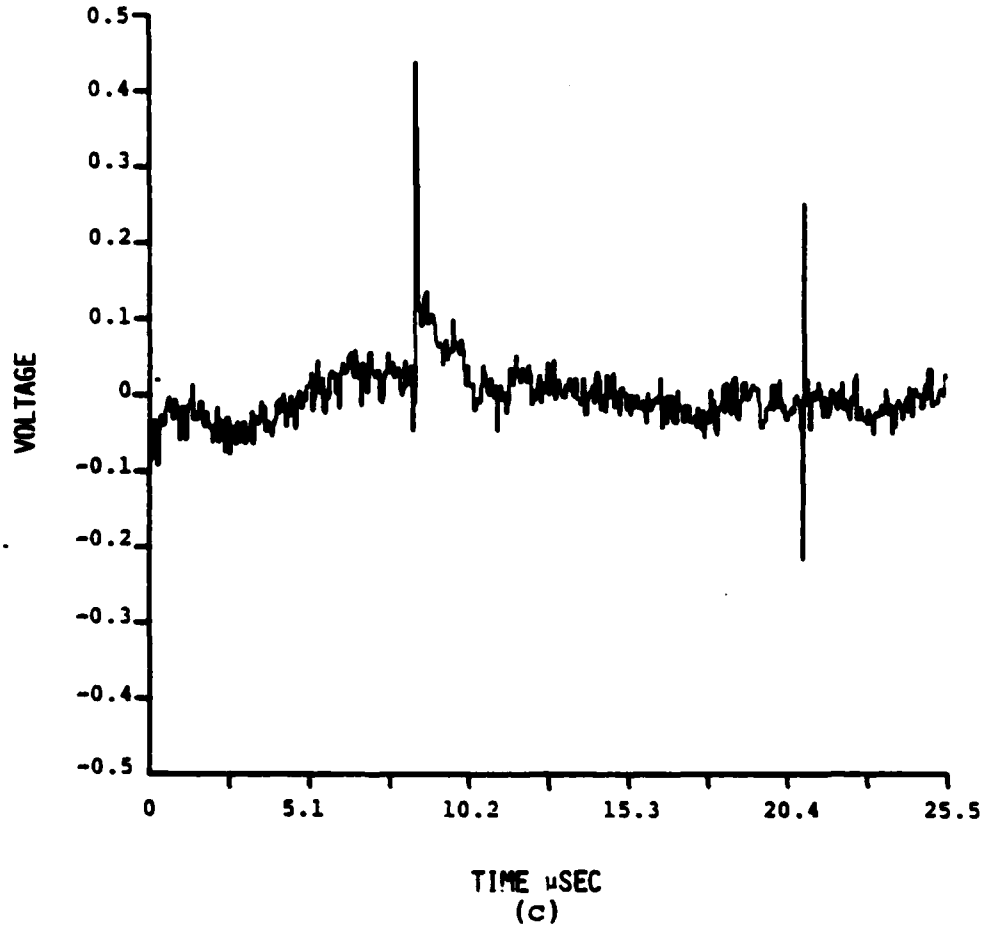
0.5
0.4
0.3
0.2
0.1
0
-0.1
-0.2
-0.3
-0.4
-0.5
VOLTAGE
0
5.1
10.2
15.3
20.4
25.5
TIME µSEC
(c)

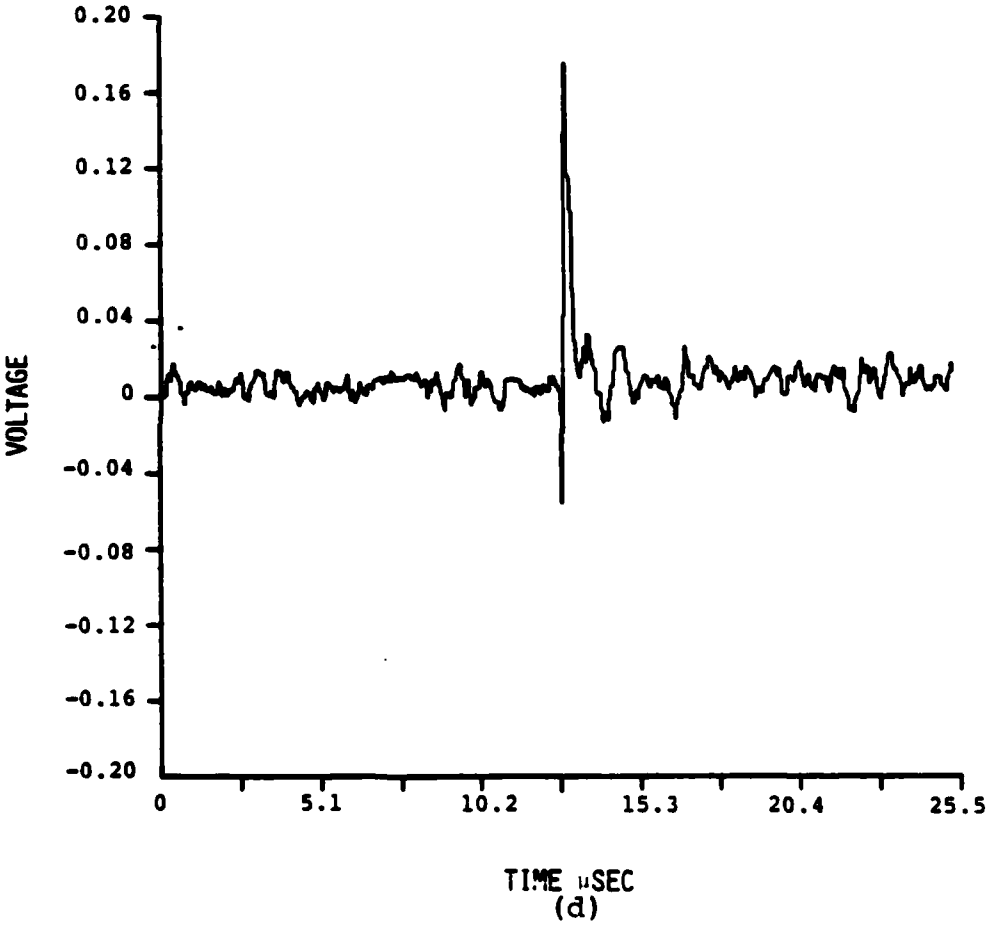
0.20
0.16
0.12
0.08
0.04
0
-0.04
-0.08
-0.12
-0.16
-0.20
VOLTAGE
0
5.1
10.2
15.3
20.4
25.5
TIME µSEC
(d)

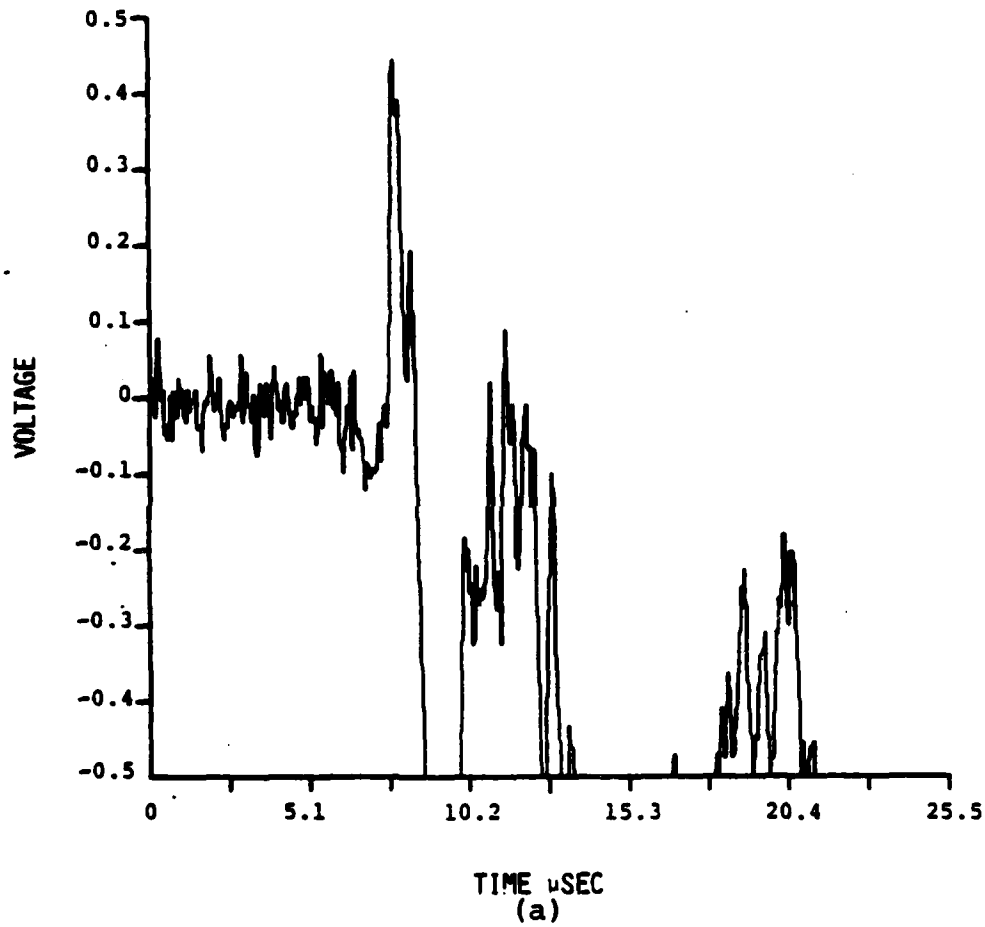

Fig. 35. Emissions detected immediately prior to failure during bend tests.

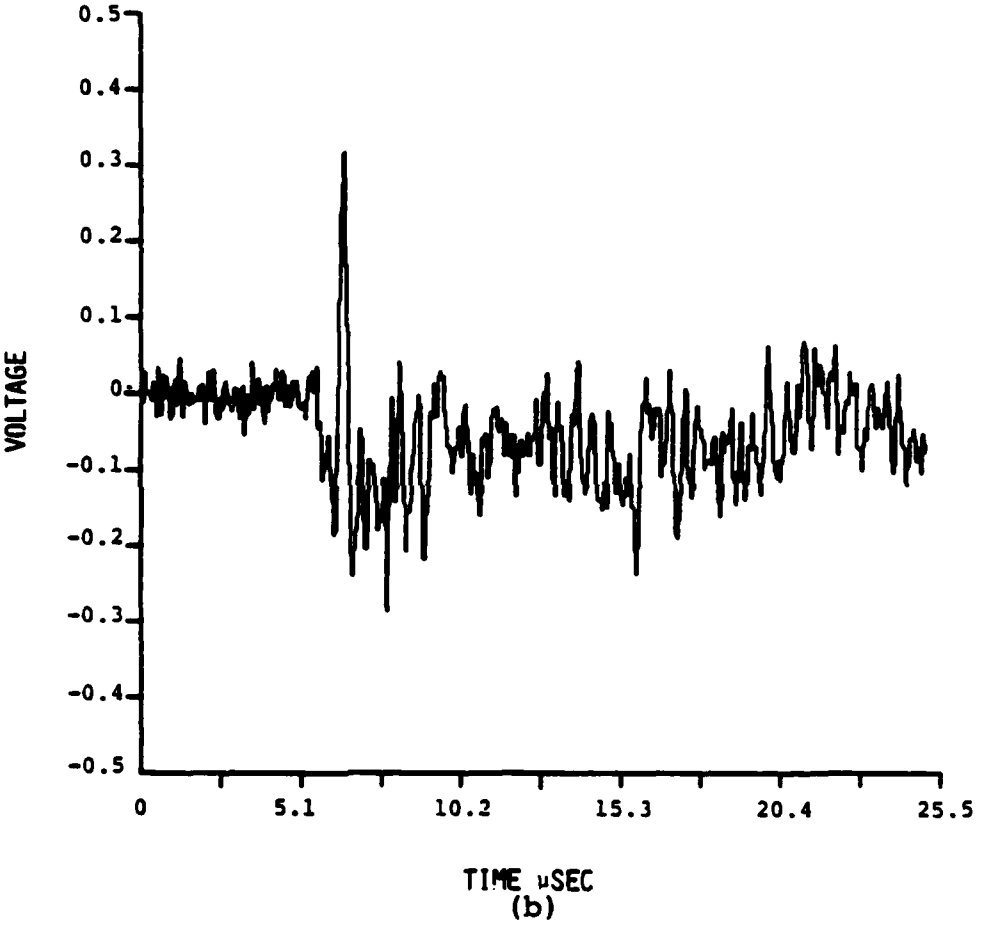
0.5
0.4
0.3
0.2
0.1
0
-0.1
-0.2
-0.3
-0.4
-0.5
VOLTAGE
0
5.1
10.2
15.3
20.4
25.5
TIME μSEC
(b)

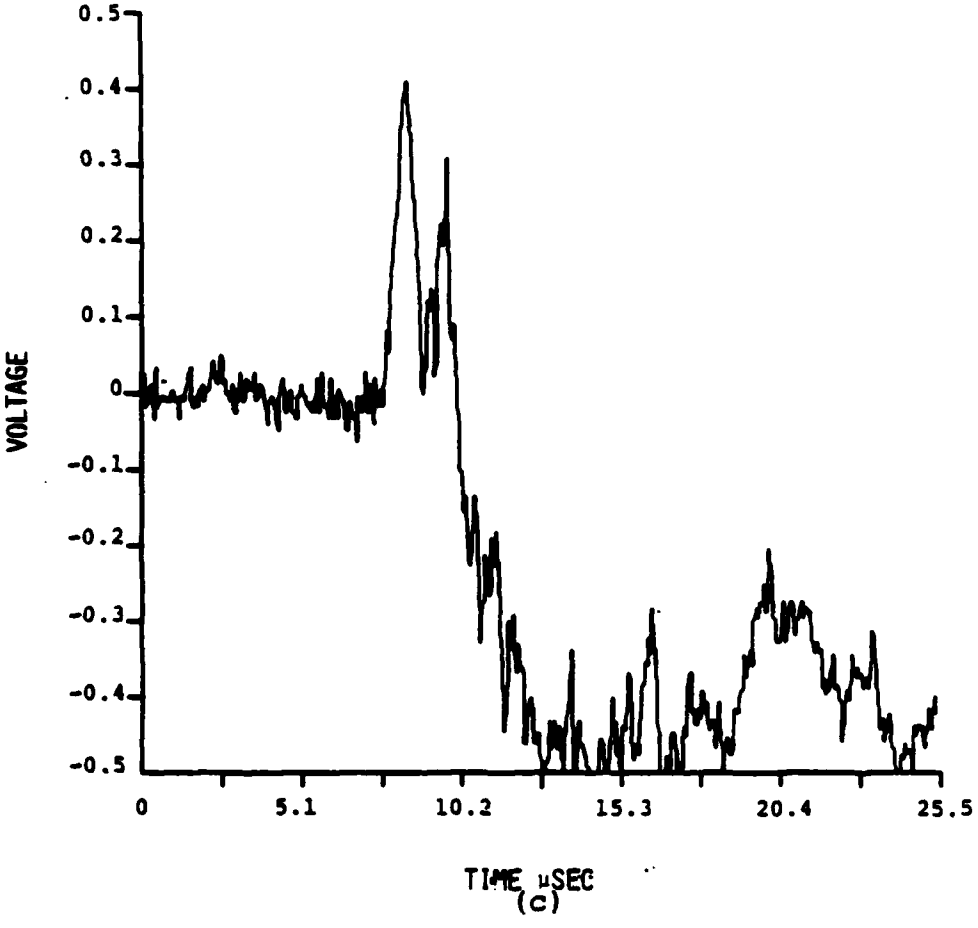
0.5
0.4
0.3
0.2
0.1
0
-0.1
-0.2
-0.3
-0.4
-0.5
VOLTAGE
0
5.1
10.2
15.3
20.4
25.5
TIME μSEC

(c)

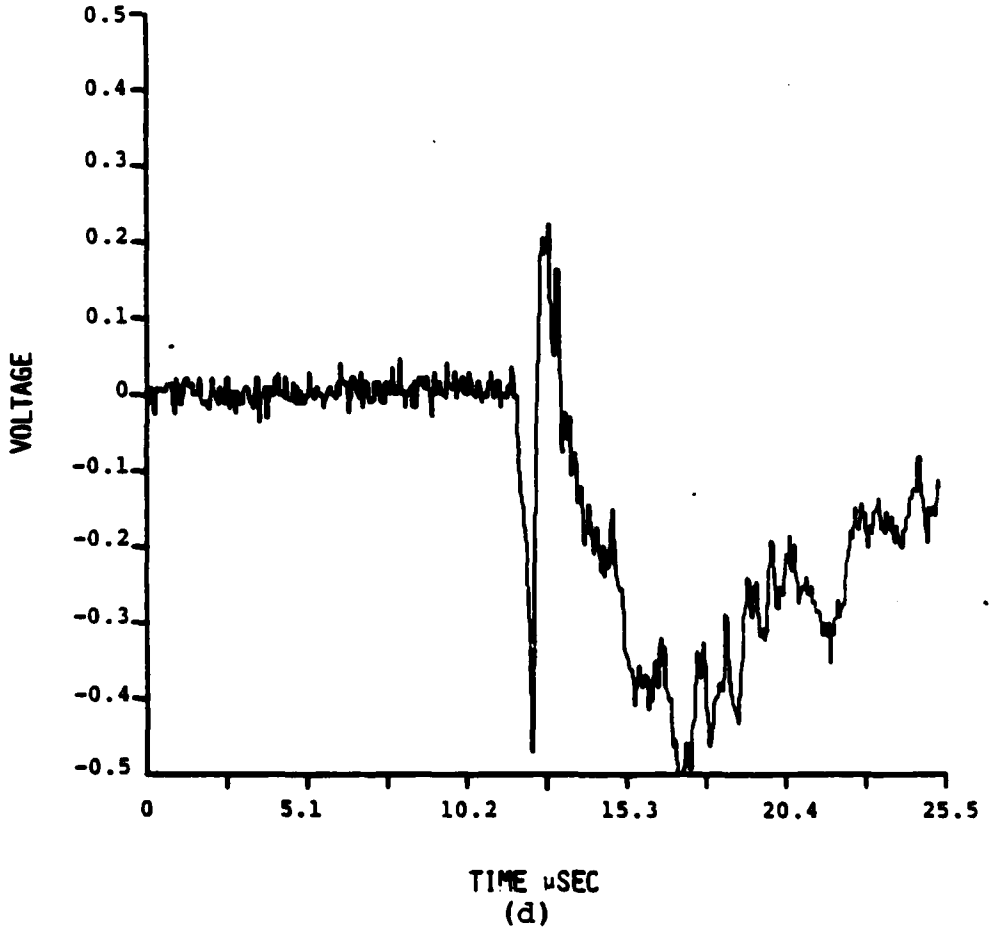
0.5
0.4
0.3
0.2
0.1
0
-0.1
-0.2
-0.3
-0.4
-0.5
VOLTAGE
0
5.1
10.2
15.3
20.4
25.5
TIME μSEC

(d)

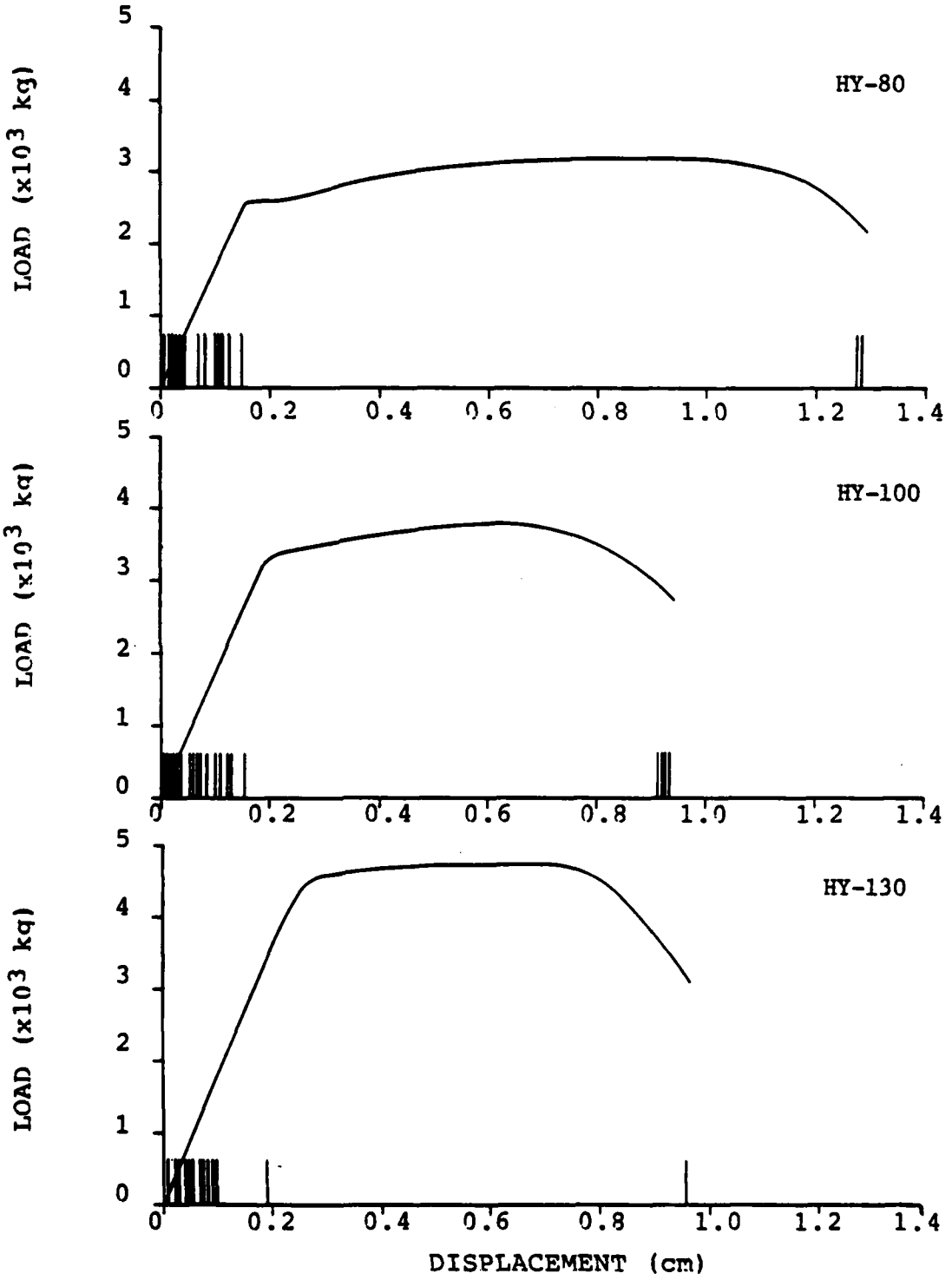

Fig. 36. Load elongation curves with AE superimposed. Each mark along x-axis corresponds to one AE.

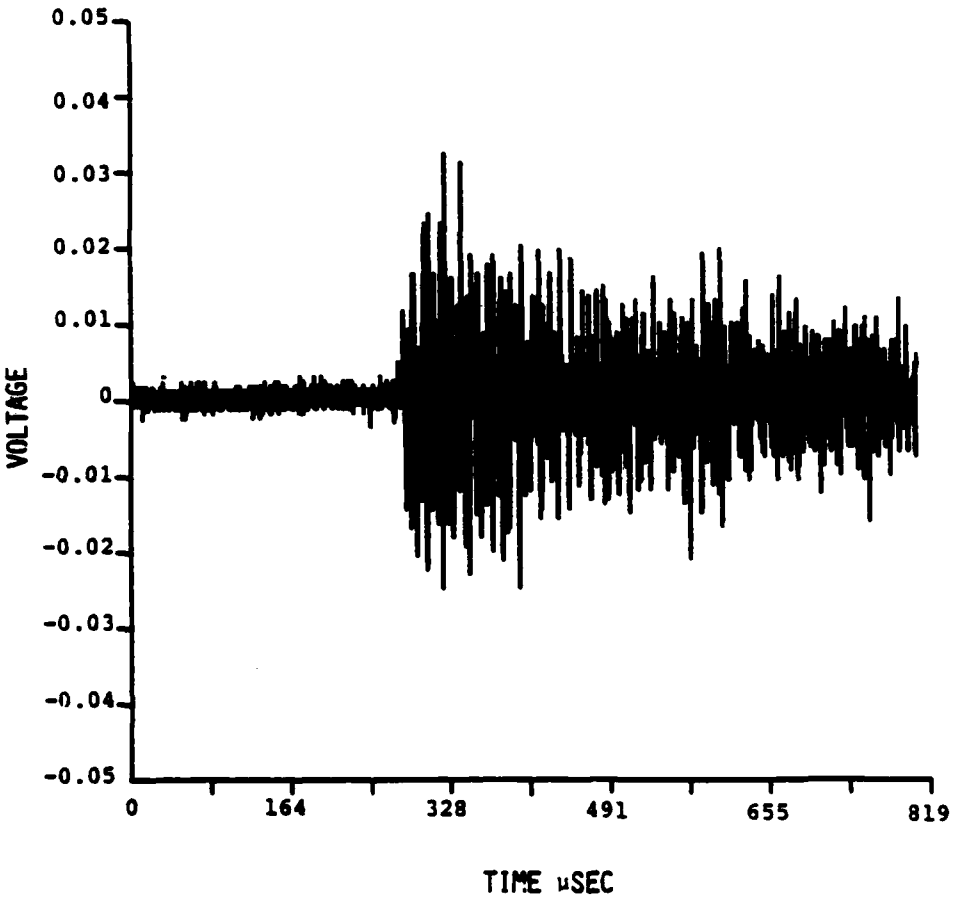

Fig. 37a. Typical waveform detected prior to yield during macro-tensile tests.

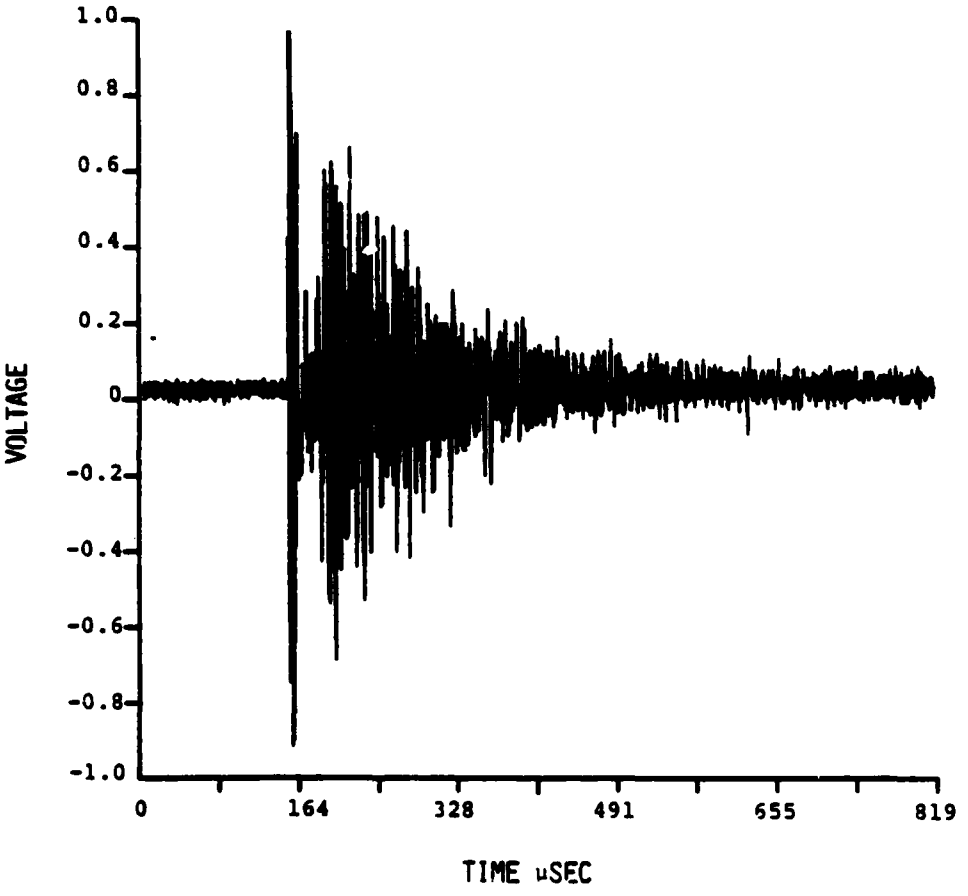

Fig. 37b. Typical waveform detected immediately prior to failure during macro-tensile tests.

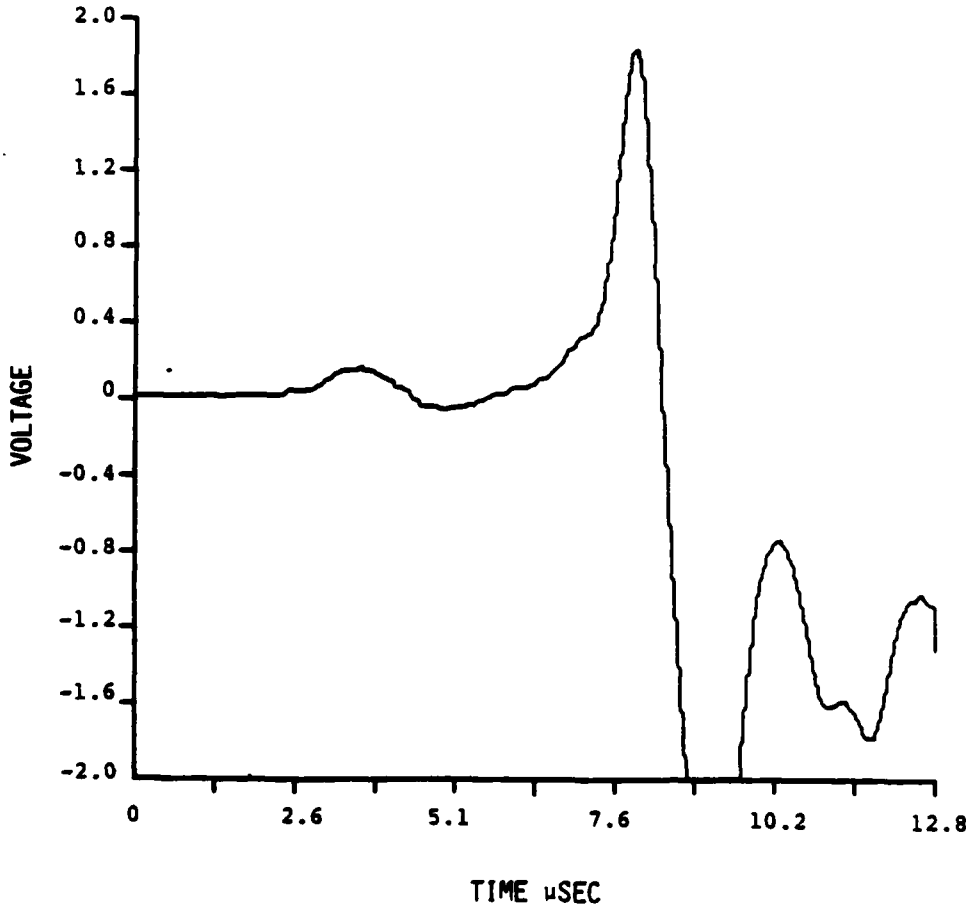

Fig.A 1. Undistorted waveform of glass capillary fracture utilized as standard during specimen geometry investigation.

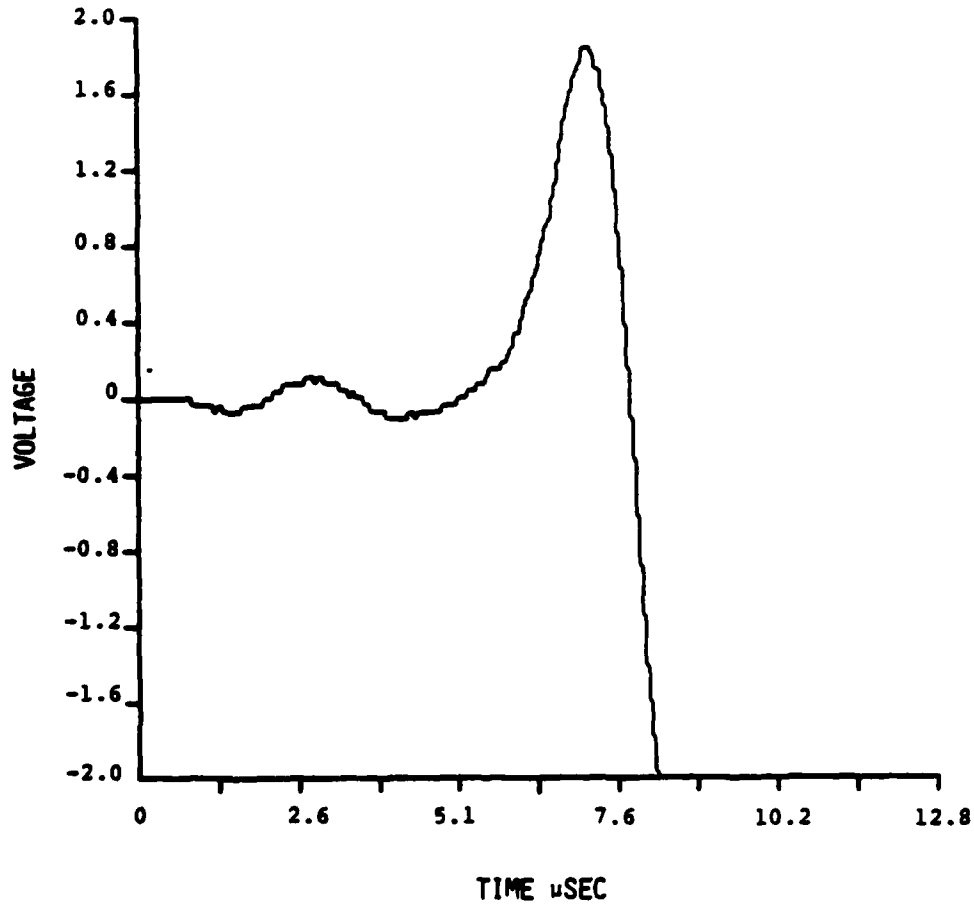

Fig. A2. Waveform of glass capillary fracture after propating through micro-specimen of dimensions width = 0.123 in. and thickness 0.62 in. (see Fig.5).

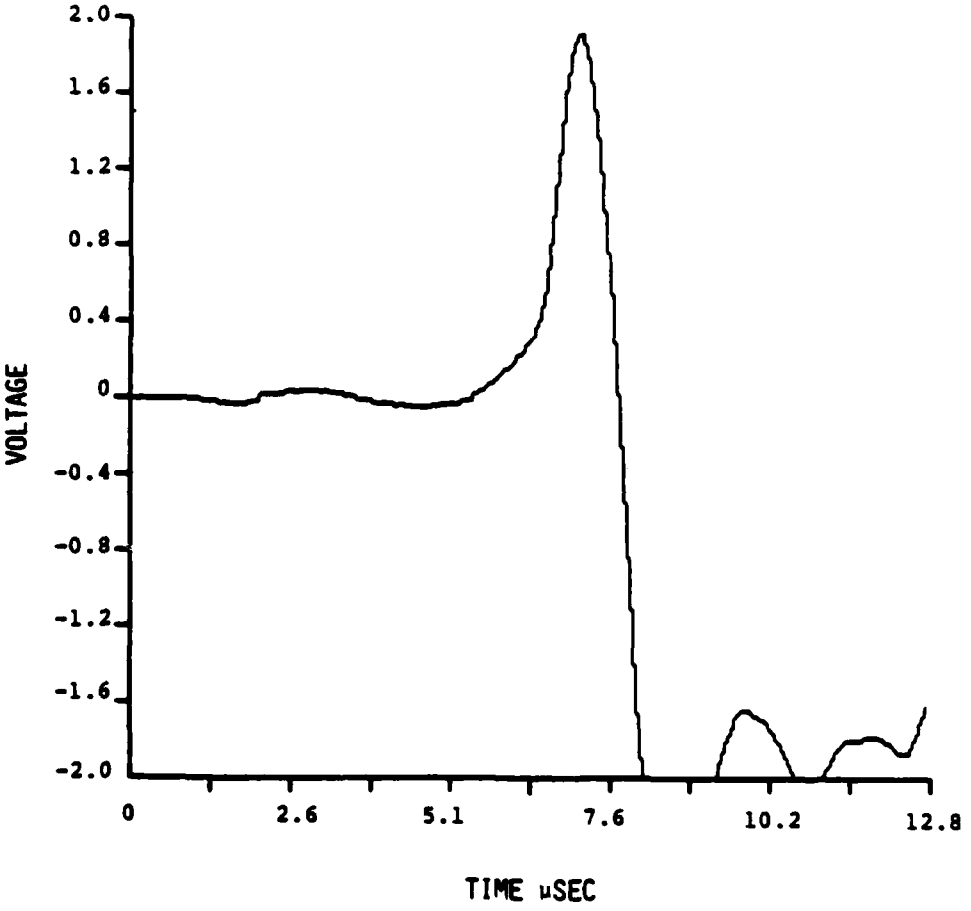

Fig.A3. Waveform of glass capillary fracture after propagating through micro-specimen of dimensions width = 0.35 in. and thickness = 0.03 in.

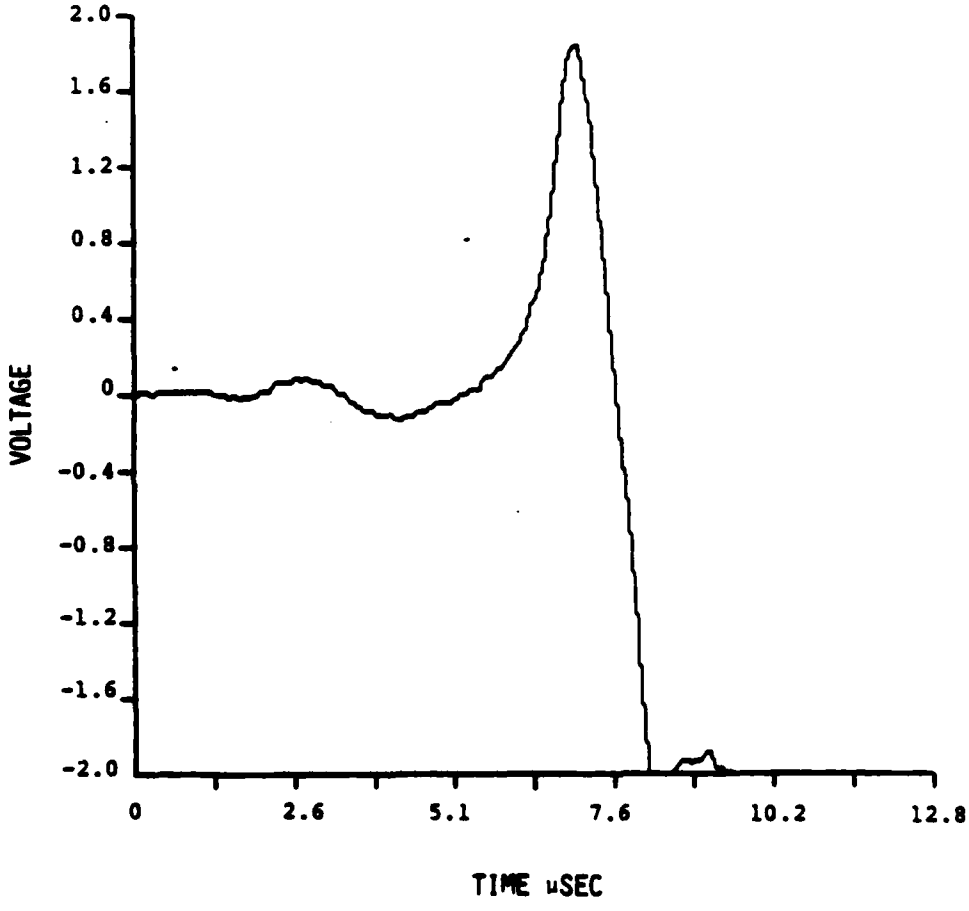

Fig.A4. Waveform of glass capillary fracture after propagating through micro-specimen of dimensions width=0.12 in. and thickness=0.03 in.

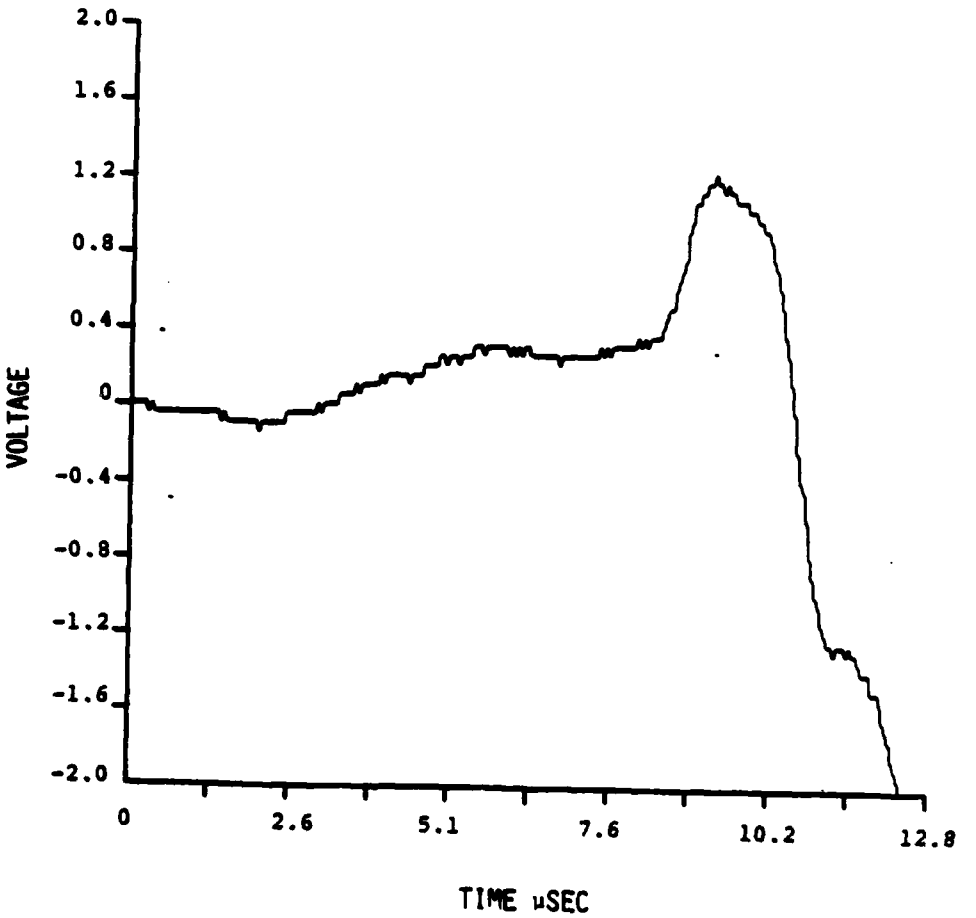

Fig. A 5. Waveform of glass capillary fracture after propagating through micro-specimen of dimensions width = 0.283 in. and thickness = 0.03 in.

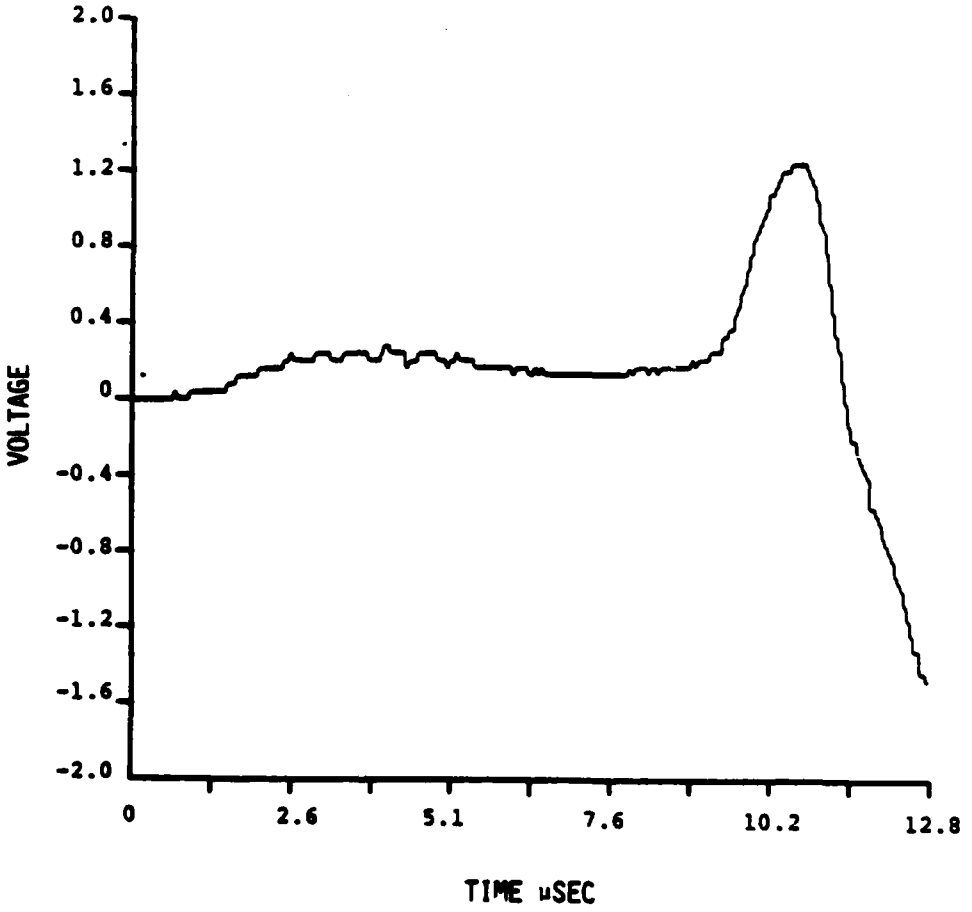

Fig. A 6. Waveform of glass capillary fracture after propagating through micro-specimen of dimensions width = 0.123 in. and thickness = 0.283 in.

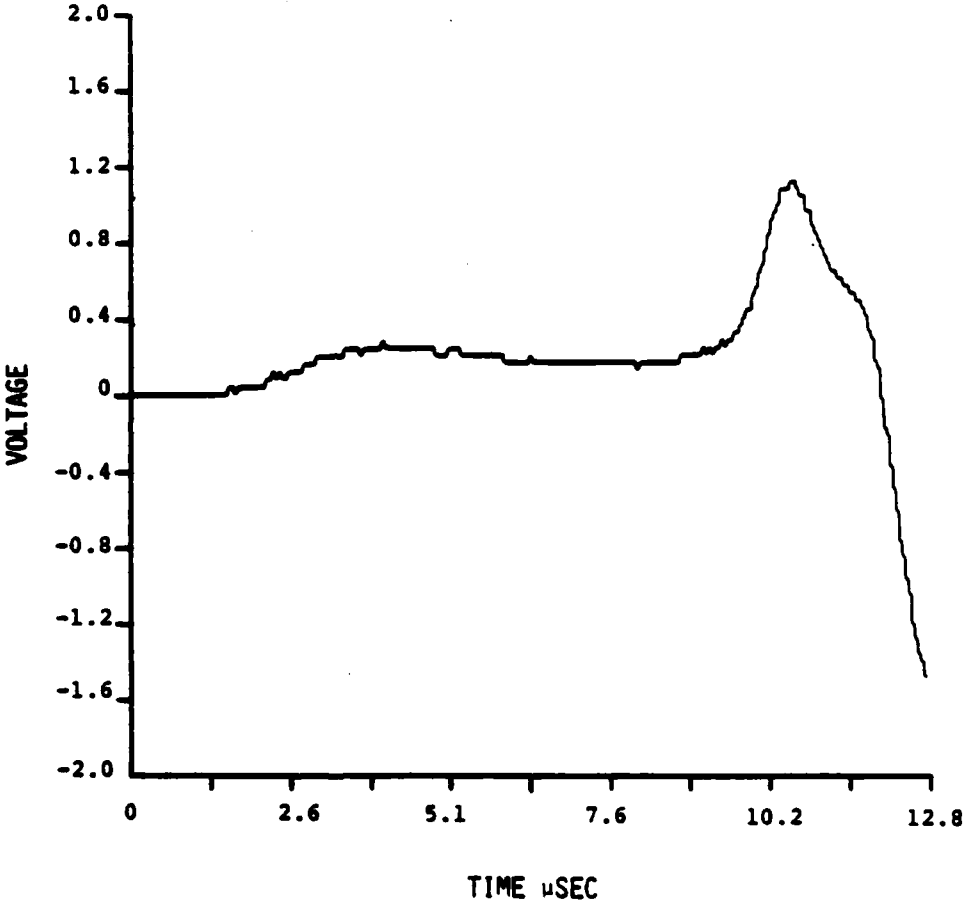

Fig. A 7. Waveform of glass capillary fracture after propagating through micro-specimen of dimensions width = 0.283 in. and thickness = 0.123 in.

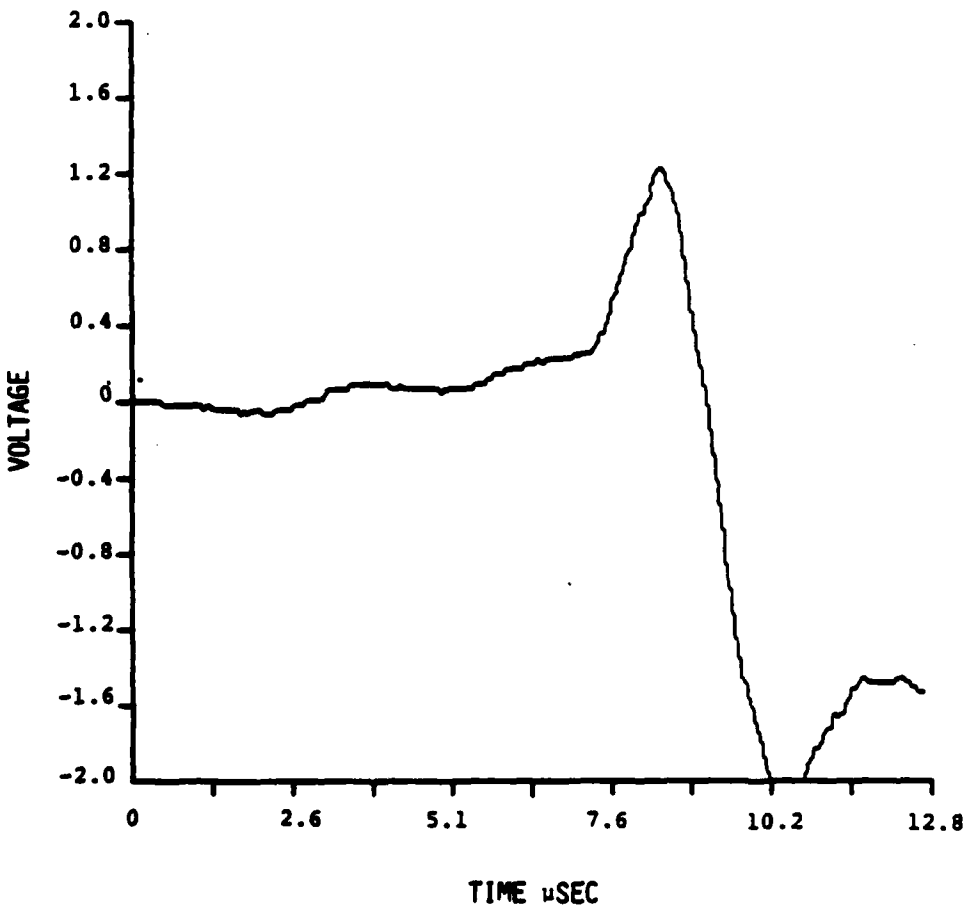

Fig. A 8. Waveform of glass capillary fracture after propagating through micro-specimen of dimensions width = 0.062 in. and thickness = 0.123 in.

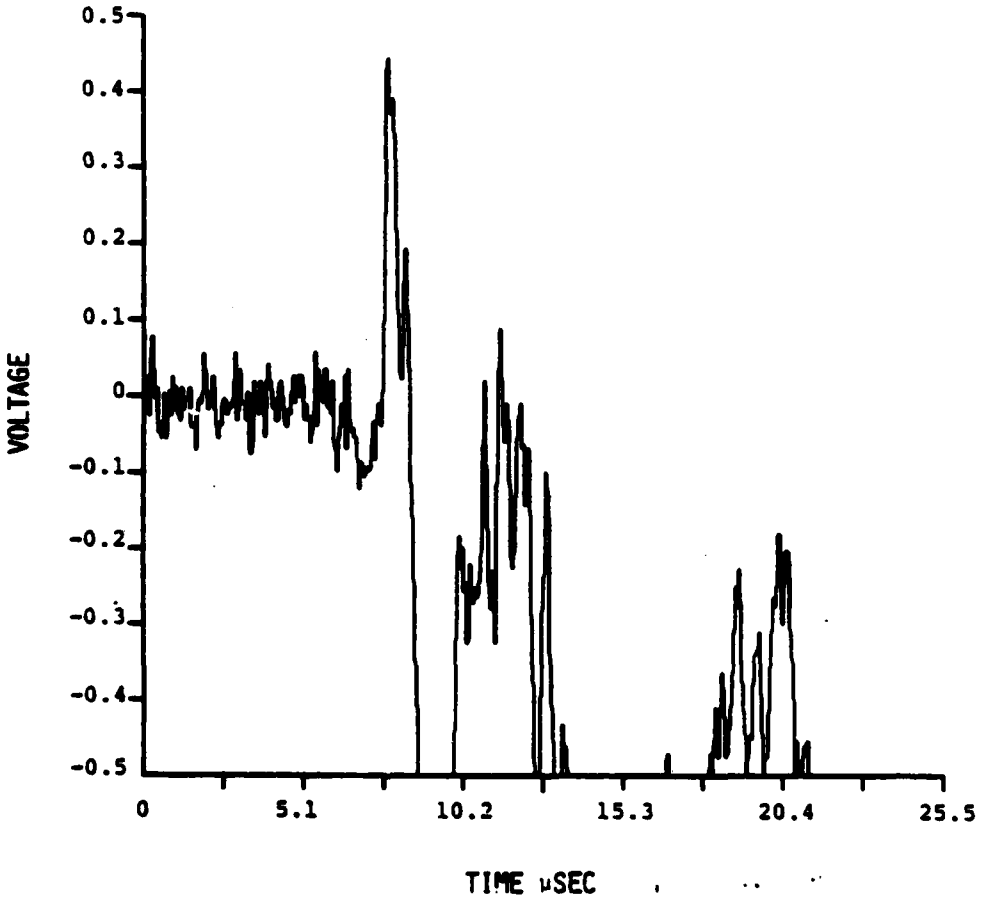

Fig. B 1. Acoustic emission detected immediately prior to failure during a bend test. Note the width (approximately 1 usec.) of the first arriving pulse.

COMPOSITION											
	C	Mn	P	S	Cu	Si	Ni	Cr	Mo	V	Ti
HY80	.16	.34	.01	.015	.15	.23	2.75	1.34	.30	.002	.003
HY100	.15	.33	.007	.017	.17	.26	2.71	1.51	.41	.003	.003
HY130	.09	.77	.007	.007	.20	.32	4.79	.56	.50	.06	.003

PROPERTIES				
	YIELD STRENGTH (ksi)	TENSILE STRENGTH (ksi)	% REDUCTION OF AREA	% ELONG. IN 2"
HY80	85.2	103.5	60	24
HY100	112.2	122.0	54.5	18
HY130	141.1	148.2	65.9	19

TABLE I. Composition and mechanical properties of HY steels.

COMPOSITION									
	C	Mn	Mo	Ni	Si	S	Cu	N	O
A533B STEEL	0.24	1.35	0.5	0.55	0.27	0.0045	0.02	0.001	0.005

Table II. Composition of A533B steel used in Harwell investigations.

INITIAL DISTRIBUTION

Copies

2 ONR
- 1 Code 431
- 1 Code 434

5 NRL
- 1 Code 6307
- 1 Code 6311
- 1 Code 6320
- 1 Code 6380
- 1 Code 6385

2 Naval Air Development Center
Naval Materials Center
Warminster, PA 18974
- 1 Code 6063
- 1 Code 6403

13 NAVSEA
- 1 SEA 05C
- 1 SEA 05M
- 1 SEA 05M/C. Null
- 1 SEA 05R
- 1 SEA 05R24
- 1 SEA 05R25
- 1 SEA 05R26
- 1 SEA 55Y
- 1 SEA 92R
- 2 SEA 996
- 2 SEA 96612

4 Naval Air Systems Command
Washington, DC 20361
- 1 AIR 320B
- 1 AIR 5163
- 1 AIR 5302
- 1 AIR 950D

1 Chief of Naval Material
MAT 0715

1 Naval Surface Weapons
White Oak, MD 20910
Mr. J. Agul

12 DTIC

Copies

1 Naval Ship Systems Engrg. Station
Measurements & Materials Dept.
Philadelphia, PA 19112
T. T. Galie

1 AFWAL
Wright Patterson AFB, OH 45433
Mr. P. A. Parmley

1 Air Force Office of Scientific Research
Bldg 410, Bolling AFB
Washington, DC 20332
Mr. J. Morgan

1 NASA
Langley Research Center
Hampton, VA 23365
Dr. J. Davidson

1 Army Air Mobility R&D Laboratory
Ft. Eustis, VA 23604
SAVDL-EU-SS/Mr. J. Robinson

1 Army Material & Mechanics
Research Center
Watertown, MA 02172
Dr. E. Lenore

1 Army Mobility R&D Laboratory
Ames Research Center
Moffett Field, CA 94035
Dr. Raymond Foye

1 Army Research Office
Research Triangle Park, NC 27709
Dr. F. Schmiedeshoff

50 Johns Hopkins University
Dept. of Civil Eng.
Materials Science & Eng.
Charles & 34th St.
Baltimore, MD 21218
R. E. Green, Jr.

CENTER DISTRIBUTION

Copies	Code	Copies	Code
1	17	1	281
1	172	1	2812
1	1720.1	1	2813
1	173	1	2814
1	2724	1	2815
1	28	1	2816
1	2803	3	522.1
1	2809M	2	5231